Application of magnetic field treatment to enhance the durability of metallic alloys under cyclic loads

A Doctoral Thesis by
Sufyan Akram

Submitted to the University of Hertfordshire in partial fulfilment of the requirement of the degree of

Doctor of Philosophy

School of Physics Engineering and Computer Science
University of Hertfordshire

Supervisor by:

Professor Andreas Chrysanthou
Dr Anatolii Babutskyi
Dr Diogo Montalvão

Date 23 June 2021

Abstract

This research studies the effect of alternating magnetic field treatment on fatigue and wear properties of EN8 steel, 70/30 brass alloy, nickel-aluminium bronze, and aluminium alloy 2014-T6. Cavitation erosion, fatigue and sliding contact wear tests were used as a means to compare the performance of the untreated and treated materials. This thesis describes the effect of the treatment on the following; (i) cantilever rotating fatigue behaviour of EN8 steel and AA2014-T6 aluminium alloy, (ii) friction/wear behaviour of EN8 steel, nickel-aluminium bronze and AA2014-T6 aluminium alloy and (iii) cavitation erosion behaviour of EN8 steel, nickel-aluminium bronze, 70/30 brass and AA2014-T6 aluminium alloy. Within this research, an alternating magnetic field treatment rig was built to treat metallic alloys.

The application of an alternating magnetic field (0.54 T) was observed to lead to an improvement in the cantilever rotating fatigue endurance of both EN8 steel and aluminium AA2014-T6 alloy. An increase in Vickers microhardness and tensile strength of both alloys in the treated condition was also observed. Fractography by using scanning electron microscopy showed evidence of more ductile fracture features after treatment in contrast to the untreated samples. The results of X-ray diffraction indicated the formation of more compressive residual stresses following treatment, while examination by transmission electron microscopy showed evidence of fewer dislocations compared to the untreated state. In the case of the AA2014-T6 alloy, Guinier–Preston (GP) zones and theta prime (Θ') were also generated by the alternating magnetic field. However, the recorded increase in temperature during the treatment range between 12-14 °C and this was not high enough to explain these observations. Therefore, the results were attributed to a non-thermal effect of the treatment, due to the change in the magnetic field direction and the change in polarity leading to depinning and movement of dislocations.

Application of an alternating magnetic field treatment (1.24 T) led to improvement of the wear/friction properties of EN8 steel, nickel-aluminium bronze and aluminium alloy AA2014-T6. To investigate the wear and friction properties, pin-on-disc wear tests were conducted. The pin-on-disc tests were under lubricating conditions using a AISI52100 steel ball bearing as the counterface material and showed a reduction in the width and depth of wear scars as well as lower values of the coefficient of friction following the treatment. In addition, nanoindentation tests, before and after treatment, revealed an increase in the hardness and Elastic Recovery Parameter. Examination by means of transmission electron microscopy attributed these results

to increased dislocation mobility and migration to the surface as a result of alternating magnetic field treatment leading to an increase in the Vickers microhardness and to a change in the residual stress state at the surface. In addition, transmission electron microscopy also revealed increased precipitation of κ_{IV} for nickel-aluminium bronze and increased precipitation of GP zones and Θ'' for Aluminium Alloy 2014-T6 in the treated conditions.

The final part of the thesis investigated the effect of alternating magnetic field treatment (0.76 T) on the cavitation erosion properties of EN8 steel, nickel aluminium bronze, 70/30 brass and aluminium alloy 2014-T6. Cavitation erosion testing (ASTM G32 10) was fulfilled at a frequency of 20 kHz in deionized water. The results showed a significant improvement in the cavitation erosion resistance for all samples treated by alternating magnetic field treatment. In the analysis of the results, the different magnetic nature of the tested alloys was taken into consideration. Scanning electron microscopy of the eroded surfaces were studied. Furthermore, microhardness measurements before and after treatment were also studied. The results of X-ray diffraction indicated the formation of more compressive residual stresses following treatment, while examination by transmission electron microscopy showed evidence of increased dislocation mobility and in some alloys increased precipitation.

From the research work demonstrated in this PhD project, the use of this alternating magnetic field treatment is a promising method for improving the mechanical properties of metallic alloys.

List of Publications and research work presented

The following list below outlines the publications and oral presentations presented during this PhD project:

List of Publications for this PhD:

- **Akram S**, Babutskyi A, Chrysanthou A, Montalvão D, Whiting MJ, Modi OP. Improvement of the wear resistance of EN8 steel by application of alternating magnetic field treatment. **Wear.** 2021:203926.
- **Akram S**, Babutskyi A, Chrysanthou A, Montalvão D, Whiting MJ, Pizurova N. Improvement of the wear resistance of nickel-aluminium bronze and 2014-T6 aluminium alloy by application of alternating magnetic field treatment. **Wear. 2021**;480-481:203940.
- **Akram S**, Babutskyi A, Chrysanthou A, Montalvão D, Pizurova N. Effect of Alternating Magnetic Field on the Fatigue Behaviour of EN8 Steel and 2014-T6 Aluminium Alloy. **Metals. 2019**;9(9):984.

Oral Presentation:

- **"Investigation of the effect of magnetic field treatment on the behaviour of metallic alloys"** Institute of Physics of Materials, Academy of Sciences of the Czech Republic, Brno, Czech Republic, **21 October 2018**

Acknowledgement

I will start by expressing my deepest gratitude to my supervisory team; Professor Andreas Chrysanthou, Dr Anatolii Babutskyi and Dr Diogo Montalvão. I also would like to thank the University of Hertfordshire technical staff, especially Arthur Collyer for his help and guidance with the experimentation and technical input into the PhD project. I would also like to thank the University of Hertfordshire workshop technical team, Giorgos Gkizelis, Dean Fitzgerald, Michael Wilkins, and Andrew Curl for their help with manufacturing parts needed for this project. In addition, I would also like to thank Dr Mark J Whiting (University of Surrey), Dr Nada Pizurova (The Czech Academy of Sciences) and Dr Calum Dickinson (JEOL UK) for teaching me the dark arts of electron microscopy.

Sadly, Dr Anatolii Babutskyi has recently passed away during the final stage of this project and I would dedicate this PhD project to him. Without his input, drive and innovative thinking, we would not have been able to accelerate this research project this far.

I would like to express my immense gratitude to my family for their support. I cannot express in words my gratitude to my parents Mohammad and Djamila Akram for their love, encouragement, and support with this PhD project. Also, I would like to thank my partner Seral Osman for being patient with me, encouraging me to continue and morally supporting me during difficult times.

Lastly, a sincere thanks to my fellow PhD friends, Lyes Azzouz, Aaqib Ayub, Pavel Sevcenko, Nathan Counsell, Yang Jiao, Kristopher Dolton, Philip Nalliah, Eli Nadia, Gongbiao Lin, Ma Mohin, Daerefa-a Mitsheal Amafabia and Mike Ngouani for making me feel welcomed in the PhD office, and being there for me with constant moral support for the times when I needed them the most. Finally, I would like to thank the Almighty Allah for helping me and guiding me through this process.

Table of Contents

List of Figures

List of Tables

Glossary

AFM	Atomic Force Microscopy
AMF	Alternating Magnetic Field
FEA	Finite Element Analysis
NAB	Nickel Aluminium Bronze
PMF	Pulsed Magnetic Field
RS	Residual Stress
SEM	Scanning Electron Microscope
TEM	Transmission Electron Microscopy
XRD	X-Ray Diffraction

1 Introduction

1.1 Background

Fatigue and wear are among some of the main causes of damage to metallic members and structures [1]. If ignored, it can lead to catastrophic failure with financial and economic costs associated with it. About 90% of all metallic failures are estimated to be due to fatigue failure [2]. It is desirable to improve the fatigue life and wear resistance of metallic structures as this will extend their lifetime and reduce repair as well as replacement costs. Metal fatigue and wear is a problem that is constantly affecting many industries including aerospace, biomedical, marine and automotive because it reduces the lifetime of structures. Improving fatigue life can be accomplished by reducing the magnitude of stress the material endures and this increases the number of stress cycles that the material can withstand. Reducing the magnitude of the induced stress can be easily achieved by increasing the size of the structural component. However, this can cause high production and operational costs, as well as a weight penalty. In the case of a vehicle, for example, this can lead to higher fuel consumption and more greenhouse emissions. Therefore, today's challenge is to increase component lifetime while maintaining an optimised structural design and keeping costs to a minimum. Aeroplanes, high-pressure vessels, steel bridges, engineering machinery and nuclear power plants are some of the many structures which need to cope with high fluctuating stresses and are highly prone to fatigue failure.

There is currently a growing interest in researching new methods for improving the mechanical properties of alloys by altering material properties to prevent fatigue and wear failure. Such methods include nitriding, carburising, high-frequency quenching and shot-peening which are widely used by industry. These techniques increase the fatigue life by increasing surface hardness and by producing compressive residual stresses at the material surface without a substantial weight penalty [3, 4]. However, some of these methods can be expensive and time-consuming and may involve heat treatment [5].

One of the new potential developments that are under investigation for improvement in fatigue resistance is the use of electromagnetic treatment (ET) [3, 6-8] which has attracted

recent research interest. The interaction between electricity and magnetism is known as electromagnetism, while the interaction of a magnetic field with electrons (or vice-versa) is known as the electromagnetic effect [9, 10]. Winterton [8] is considered to be the first researcher who investigated the effect of a saturated magnetic field on the fatigue behaviour of materials (plain carbon steel) in 1959. Since then, there have been intensive investigations using ET in the form of static magnetic fields in metallic materials [11]. The technique has been shown to be successful in relaxing stresses [12], improving fatigue resistance [13] and changing other mechanical properties [14]. ET has also been applied in the form of direct electric current pulsing [15] and pulsed magnetic field treatment [16]. Pulsed magnetic field treatment is considered to be more economical in generating a high energy magnetic field than static magnetic field treatment [11, 17]. High current density can be achieved through the application of electropulsing in the material. This high current density has been shown to input transient energy from an external environment to reorganise and even repair fatigue damage within the microstructure [18]. Troitskii pioneered the use of electropulsing for metallic alloys and subsequent studies have shown that the techniques could enhance the fatigue life of steel [4, 13, 15, 19-21], copper [6], titanium [22, 23] and aluminium alloys [24, 25]. The use of ET can be promising for extending the fatigue life of these structures [11, 26, 27]. In comparison to conventional treatments like heat treatment, magnetic field treatment is easy to perform [28] and the treatment time is significantly less [29].

The improvement of fatigue life by the application of ET has been attributed to various mechanisms including dislocation movement , microstructural changes by temperature increase due to Joule heating [4, 18, 22], stress relaxation [20, 22, 30] and crack healing [15, 21, 31]. However, there are also several studies that have shown that fatigue life can be reduced by the use of ET [21, 32, 33]. To explain this contradiction, it has been suggested that excessive treatment can cause damage due to melting and/or oxidation. Hence, to develop the application of ET, a better understanding of its effects is needed including knowledge of the optimum treatment parameters.

Through the investigation of magnetic field treatment, the research conducted by this project aims to develop a new material processing technique using magnetic fields to enhance the mechanical properties of alloys. In order to test the mechanical properties, several cyclic load

tests were conducted. This includes fatigue testing, cavitation erosion testing and sliding contact wear testing. A wide range of alloys including EN8 steel, aluminium alloy 2014-T6, nickel aluminium bronze and brass alloy were involved in this study. The technique that is investigated in this research is alternating magnetic field treatment. The work which is reported in this research differs from earlier work in that it applies an alternating magnetic field treatment that uses simpler equipment and is more cost-effective in comparison with pulsed magnetic treatment and electropulsing.

1.2 Research Question

This research will aim to answer the following question:

"How does alternating magnetic field treatment affect the fatigue and wear properties of metallic alloys?"

This research will investigate the effects of the treatment on metallic alloy and what causes the change in the mechanical properties. There have been several studies that have investigated the effects of pulsed magnetic field treatment and electropulsing, however, not much work has been done using alternating magnetic field treatment. Furthermore, there has not been a large level of properties studied using this technique and with a variety of different alloys. Hence, in this investigation, EN8 steel, nickel aluminium bronze, 70/30 brass alloy and aluminium alloy 2014-T6 are investigated. To test the cyclic mechanical properties, cavitation erosion, fatigue and sliding contact wear tests were used as a means to compare the mechanical performance of the untreated and treated materials.

1.3 Outline of the thesis

The thesis is outlined as follows:

- Chapter 1 outlines the background and the need for magnetic field treatment to improve the fatigue and wear properties of materials.

- Chapter 2 gives a detailed literature review on the effects of electromagnetic treatment on fatigue, wear and mechanical properties. It also presents a fundamental theory of magnetism and a literature review on electromagnetic field treatment. Furthermore, the aim and objectives of the research project are found here.

- Chapter 3 elucidates the type of electromagnetic processes involved in this project and gives reasons for the chosen processing parameters used in this project.

- Chapter 4 presents the methodology used in the project and describes the experimental setup for the mechanical testing, fatigue testing, pin-on-disc testing and cavitation erosion testing. The characterization techniques used are described; these include X-ray diffraction (XRD), Vickers microhardness and electrical conductivity measurements as well as scanning and transmission electron microscopy. In addition, details on sample preparation are presented.

- Chapter 5 presents and discusses the effects of alternating magnetic field treatment on the fatigue behaviour of EN8 steel and aluminium alloy 2014-T6. In this chapter, fatigue testing along with XRD residual stress, hardness and tensile tests were conducted. Scanning electron microscopy (SEM) was carried out to analyse the fracture surface and transmission electron microscopy (TEM) was employed to elucidate the mechanisms that led to improvement in fatigue resistance.

- Chapter 6 presents an investigation of the effects of alternating magnetic field treatment on the wear properties of EN8 steel, nickel aluminium bronze and aluminium alloy 2014-T6. Further characterisation including XRD, microhardness and electrical conductivity measurements were also conducted. Analysis of wear scar tracks for treated and untreated EN8 steel, nickel aluminium bronze and aluminium alloy 2014-T6 was conducted by SEM. Finally, TEM was employed to understand the mechanism behind the improvement in the wear resistance.

- In Chapter 7 the effects of the alternating magnetic field treatment on cavitation erosion are presented. Alternating magnetic field treatment was conducted on four

alloys (EN8 steel, nickel aluminium bronze, 70/30 brass and aluminium alloy 2014-T6). The erosion rate, topographical and microstructural analyses for the cavitation erosion-corrosion experiments are presented along with further analysis involving residual stress measurements by XRD, microhardness and electrical conductivity measurements.

- Chapter 8 presents the conclusions of the research and proposes future research in the area of electromagnetic processing.

2 Literature Review

2.1 Fatigue

Fatigue is defined as the gradual degradation and eventual fracture of a material due to progressive cracking under repeated alternating or cyclical stress [1, 34-37]. These repeated stresses are lower than the yield strength of the metallic component concerned [35]. Fatigue loads are usually cyclic by nature, however, they are not necessarily of constant size or amplitude [35, 37]. The process of fatigue failure can be characterized into three distinct steps: (1) Crack initiation where a small crack is formed at a point of high-stress concentration; (2) Crack propagation during which stage cracks advance incrementally with each stress cycle; (3) Final fracture which takes place quite rapidly once the advancing crack has reached a critical size. Cracks that are associated with fatigue failure are often initiated on the surface of a component at some point of stress concentration. Crack nucleation sites are usually caused by surface scratches, sharp fillets, keyways, threads, dents, etc [38]. Furthermore, cyclic loading can produce microscopic surface discontinuities resulting in dislocation slip steps that may also act as stress raisers. Dislocations are crystallographic defects or irregularities within a crystal structure and result in an abrupt change in the arrangement of the atoms.

Microscopic investigations have shown that during fatigue, the gradual accumulation of micro-failures further leads to the growth of fatigue cracks which are points of high-stress concentration within the material. Dislocation pile-up occurs and it is created by the fluctuating loading produced during fatigue. This is what is known as persistence slip bands (PSB). Furthermore, this can lead to the microstructure of the alloy becoming unstable due to the formation of PSB and grain interferences [39]. Due to the presence of PSB, tiny steps are formed at the surface; these steps can serve as areas of high-stress concentration causing fatigue crack initiation. If the fatigue cracks are left untreated, they will propagate and the material will fracture [40]. Fatigue can be classified into two different categories, low-cycle fatigue and high-cycle fatigue. Low-cycle fatigue occurs when materials experience high loads that produce not only elastic strain but also some plastic strain during each cycle. Consequently, fatigue failure for Low-cycle fatigue occurs at less than 10^4 to 10^5 cycles. Fatigue that occurs at lower stress levels wherein deformation is completely elastic and hence the fatigue life is longer, is known as high-cycle fatigue. High-cycle fatigue is associated with

fatigue life greater than 10^5 cycles. Under these circumstances, the stress levels are considerably lower than the tensile or yield strength acting on the material. This is due to low stresses causing the material to experience elastic deformation [41].

It is desirable to increase the fatigue life of materials by reducing the effect of fatigue. This can be accomplished in several ways including reducing the magnitude of the applied stress that the material experiences. The reduction of the magnitude of the induced stress can be easily achieved by an increase in the size of the structural component. However, this also leads to an increase in weight and production and operational costs. In the case of a vehicle, this may lead to an increase in mass, fuel consumption and more greenhouse emissions. Therefore, the challenge is how to increase fatigue life while maintaining an optimised structural design.

During fatigue loading, the surface of the component/part starts to become rough. As a result, PSBs are created that include intrusions and extrusion profiles [42] which are points where fatigue cracks start to initiate. Furthermore, the radius of curvature of the crack tip can also influence crack growth. During cyclic loading, there is high plastic deformation near the crack tip due to the presence of a high level of stress concentration. Plastic deformation caused by fatigue loading can make the crack tip blunt. However, during unloading, the crack tip is sharpened. This repetitive process of blunting and re-sharpening continues while the crack advances. Based on fractographic observations, striations or closely spaced ridges are usually evident on the fractured surface. When the fatigue load is interrupted, the formation of benchmarks occurs; these can be observed microscopically as shown Figure 2.1.

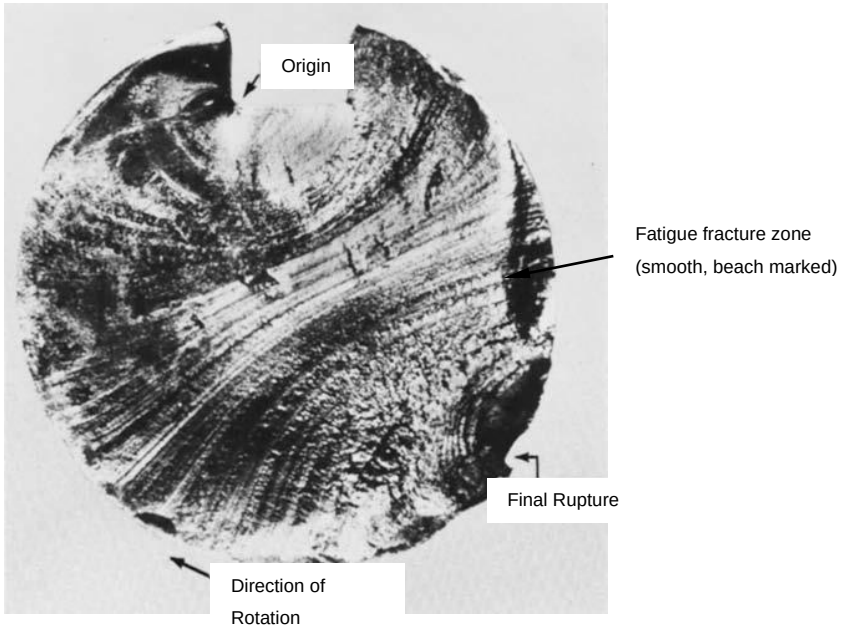

Figure 2.1. Fracture surface of a rotating steel shaft that experienced fatigue failure [43].

For many common loading situations, the maximum stress acting on a component is at the surface. Subsequently, this can lead to crack formation and crack propagation on the surface. Consequently, most cracks that lead to fatigue failure start at the surface and specifically at stress amplification sites. Therefore, it has been observed that fatigue life is indicative of the condition and configuration of the component surface. There are numerous factors influencing fatigue resistance; these include various types of surface treatment involving carburizing, nitriding or shot peening. These techniques have shown to increase the fatigue life of metallic alloys, however, the cost and time required to apply these techniques are often high.

Fatigue failure is the most frequent cause of metal failure and has a substantial impact on most structural failures [36]. Hence it is important that careful consideration must be taken during product design and manufacture especially if the product is intended for use involving highly demanding applications. Hence, developing new and cost-effective methods for increasing fatigue resistance is important in today's society. Later in the chapter, methods for improving fatigue resistance using electromagnetic processing will be explored.

2.2 Friction and Wear

Wear is a phenomenon that normally occurs in a sliding, rolling or impact motion when two surfaces rub against each other. This leads to deformation or material loss from one or both surfaces [44]. In many cases, wear can lead to damage to the working components and can even lead to mechanical failure [45]. The field of Tribology was established in 1967 to study the wear phenomenon. Tribological research is an important contribution to the improvement of the performance of rotary and reciprocating motion machinery and therefore it is important for the reduction of natural resources and energy saving. Wear is a response of a system that is affected by many factors, for example, the working conditions and material properties. Having low wear is not always associated with the material having a low coefficient of friction.

There are four principal types of wear mechanisms; these are adhesive wear, abrasive wear, fatigue wear and tribo-chemical wear [46]. These four types of wear mechanisms are named based on their removal mechanisms. These mechanisms can appear either alone or in combination causing aggressive material loss on the mating surfaces.

2.2.1 Adhesive Wear

Adhesive wear occurs as a result of adhesive bonding between asperities of two flat rubbing surfaces under sliding contact. There is a high possibility of adhering wear occurring if the two rubbing surfaces are made of identical material. This is due to adhesion and bonding being strong in such situations due to asperity contact which does not produce wear debris instantaneously. During sliding contact, asperities are sheared and compressed unceasingly and cracks, plastic deformation and fragment transfer occur on the two rubbing surfaces. Accumulation of fragments then takes place; some of the accumulated fragments fall off due to surface rubbing and become wear particles [47, 48]. This process can be aggravated under high loading and high sliding speed conditions. Adhesive wear can occur under both lubricated and non-lubricated conditions and therefore, it is difficult to eliminate adhesive wear [49, 50]. Severe adhesive wear can, however, be significantly reduced by applying lubrication which can form a protective tribo-film.

2.2.2 Abrasive Wear

Abrasive wear is caused when asperities of a rough, hard surface or hard particles slide on a softer surface causing damage to the interface by plastic deformation or fracture [51, 52]. Abrasive wear can be categorised into two types, second body abrasive wear and third body abrasive wear [51]. Second body abrasive wear occurs when relatively harder surfaces slide on a softer surface. Grinding, cutting and machining are typical examples of second-body abrasive wear [51]. Third body abrasive wear occurs when one or both of the surfaces are abraded by grit or particles that are trapped in between two surfaces or embedded on a softer surface [51, 53]. The abrasive grit must have a higher hardness than at least one of the surfaces in contact. In this scenario, the relatively harder surface of the two surfaces plays the role of the third body. For example, third body abrasive wear can be found in mechanical operation systems such as free-abrasive lapping and polishing [51]. Abrasive grooves caused by abrasive wear of particles or asperities from the harder surfaces can be observed on the worn scar tracks. The main mechanism for generating wear debris is micro-cutting. The hardness and size of the particles can potentially exert a strong influential force on the degree of abrasive wear [54]. During the sliding process, third body abrasive wear is generally the consequence of adhesive wear as the debris generated can be trapped between surfaces and become abrasive grit [51].

2.2.3 Fatigue Wear

Fatigue wear is caused by very high loads that are repeated a large number of times during a sliding and rolling process. When the applied load exceeds the fatigue limit of the material then fatigue occurs [55]. Fatigue wear starts with crack initiation beneath the contact surface and then spreads as the load cycles continue. In addition, the primary cracks start to propagate along a slip plane or dislocation cell boundaries. As a result, primary cracks develop and connect with a subsurface crack leading to secondary cracks. Subsequently, when several cracks start to develop to a critical level, the material above the cracks will be removed and then fatigue wear occurs. This can be observed due to crack formation and flaking of surface material due to the characterisation of fatigue wear [56]. Fatigue wear can happen with or without lubrication and has been reported in some cases to accelerate with improper lubrication [57]. An illustration of crack initiation and propagation is shown in Figure 2.2 [58].

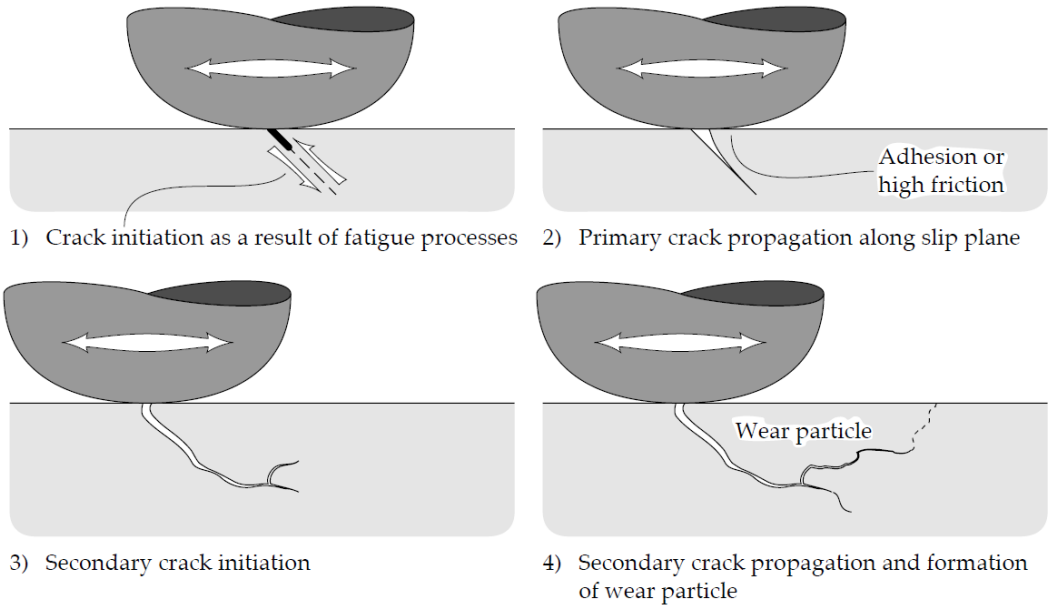

Figure 2.2. Schematic illustration of the process of surface crack initiation and crack propagation [58].

2.2.4 Chemical (corrosive) Wear

Chemical wear is caused by friction in a corrosive environment. Generally, surfaces are covered by a layer formed by a chemical product of corrosion. This layer acts as a protective layer on the surface to protect against further corrosion. However, once the slide action takes place on the surface, the protective layer can be damaged and leads to exposure of bare material beneath the layer. Hence, the corrosive elements in the environment can react with the exposed surface continuously [51]. The degree of chemical wear is dependent on the rate of the chemical reactions [59]. Chemical wear requires both the chemical reaction and the rubbing; in order to reduce the effect of chemical wear, it is advisable to avoid (where possible) operation in a corrosive environment such as high temperature and high humidity.

There are two general approaches to improve the wear/friction resistance of a mechanical system; either by separation of attrition faces of parts by use of a liquid or solid lubricant and modification of the material and its properties; the application of a coating is one possible measure that can be taken up. Alternatively, traditional processing techniques such as

temperature, pressure and time may be used to alter the properties of the material. These techniques are used to increase the material hardness which thus increases the wear resistance of a mechanical system. Later in the chapter, alternative methods for improving the wear resistance using electromagnetic processing will be addressed.

2.3 Cavitation Erosion

Cavitation was first reported in 1754 by the famous Swiss mathematician Euler , while working on the design of a water wheel and the influence it might have had on the wheel's performance. Cavitation is destructive in nature and can cause severe damage or material loss, especially during the operation of ships. Cavitation can cause erosion of components such as ship propellers and rudders. This resultant destruction can lead to expensive maintenance in the form of frequent docking, inspection and prevention or replacement of damaged parts [60]. Cavitation is a fluid mechanics phenomenon, that occurs whenever there is a change in the velocity of a fluid and/or in a pressure field. It takes place in regions where the flow conditions cause absolute pressure. This leads to boiling of the fluid even at ambient temperature. Small vapour bubbles or "cavities" then form within the fluid and they implode when the surrounding pressure rises again. The collapse of the cavities creates a highly localized and instantaneous pressure resulting in high-intensity shock waves and jet impact, leading to significant erosion on any material surface they come into contact [60]. Hence the phenomenon of bubbles collapsing on the material surface, causing erosion, is called cavitation [61].

Cavitation is often deemed detrimental to anything it comes into contact with, leading to erosion of the material. Cavitation damage can lead to serious issues, especially in restricted waterways with high flow rates, impellers, pumps, turbines and boat and marine propellers. Figure 2.3 shows the severe cavitation damage that has been incurred on the blades of a Francis turbine [62].

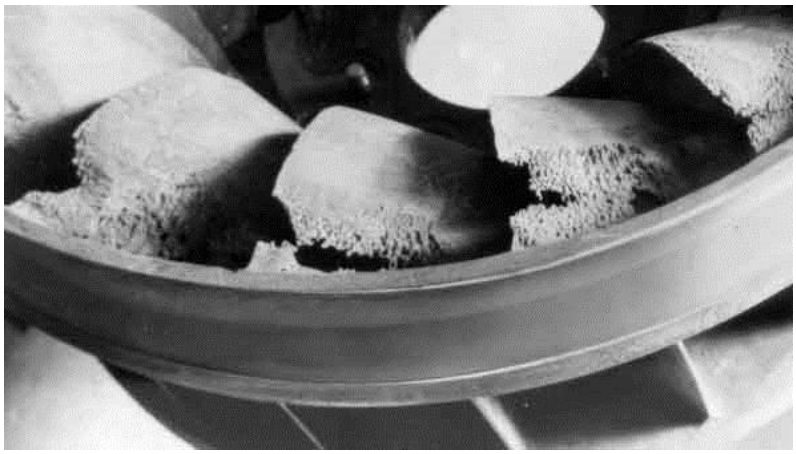

Figure 2.3. Cavitation damage on the blade at the discharge from a Francis turbine [62].

Cavitation erosion can be tested by various cavitating flow methods including Venturi apparatus, single hydrofoils radial-pump, vibratory apparatus, etc. Among these various laboratory techniques, the most common methods reported in the literature to study cavitation are the rotating disk method, the hydrodynamic tunnel method and the vibratory devices. Table 2.1 shows a list of the various types of cavitation test methods [63-67]. In comparison to the other methods mentioned in the table, the cavitation test using the ultrasonic vibratory test rig has been known to give the most reproducible cavitation results within a controlled laboratory environment. This, however, does not represent real-life conditions such as those encountered by a propeller or a rudder. The cavitation bubbles in an ultrasonic vibratory test produce nearly uniform-sized cavitation bubbles forming at the same location and excited at a fixed frequency. However, in reality, during actual the cavitation erosion process, the cavitation field may vary depending on the bubble nucleus size and exciting frequencies. Therefore, cavitation erosion can occur at different locations of the propeller [68].

Table 2.1. List of different methods for cavitation testing [63-67].

Test Techniques	Principle	Test Duration
Cavitating Jets	High Pressure and speed jets are discharged causing cavitation damage	A couple of days
Circular Leading Edge (CLE) Single hydrofoil	This is achieved using a closed loop with an air dome and a vacuum pump to enable variation of the static pressure.	A couple of days
Emersion Cavitation Tunnel	This is caused by radial divergent that is introduced in the flow to create unsteady cavitation	Minimum of 10 hours
Radial Pump	Specimens are secured on an impeller blade rotating in a closed loop of cavitation flow	A couple of days
Rotating Disk	A disk with the cavitation inducers and specimens fixed together as it rotates in the water to provide a cavitation flow	24 hours
Vibratory Cavitation	This is produced by an ultrasonic vibratory horn that is used to create cavitations on the sample	30 minutes
Venturi Flow Test	Cavitation is introduced by using a Venturi throat	16 hours

2.3.1 Cavitation Wear

Cavitation wear is mechanical in nature and can not occur without tensile and compressive stresses. Cavitation wear damage is subjected to several periods of activity. Depending on the surface structure, the material surface is deformed, loosened and eventually eroded in various ways. This is due to the frequent strain from the shock waves [69, 70].

The rate of erosion is dependent on the exposure period and it increases from negligible values, reaching a maximum before decreasing again and finally levelling off to a steady value. Figure 2.4 shows the rate of cavitation erosion with time for a typical cavitation erosion process. The behaviour is characterized by four stages; firstly the incubation period, then maximum rate, deceleration period and the steady-state period [70].

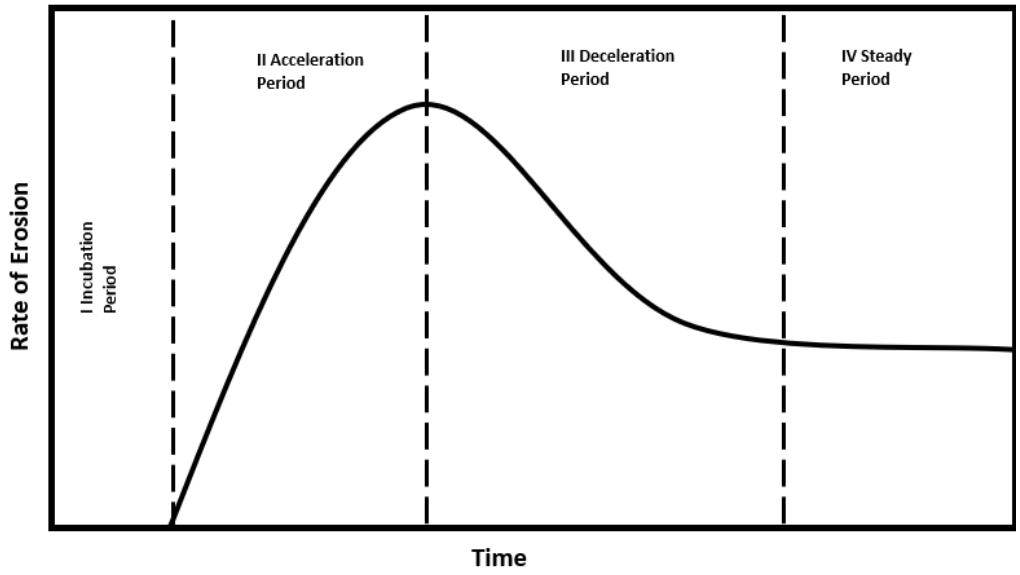

Figure 2.4. Classification of the erosion periods [71].

Incubation period – This is known as the zero loss period depicted by zone I in Figure 2.4. In this zone, the mass loss is almost zero or negligible [70]. During this stage, micro-cracks nucleate around the grain boundaries and inclusions form due to both elastic and plastic deformation at the surface [70]. As a result, the surface of a ductile metal would first undergo elastic deformation and then plastic deformation causing dents to form with time. After this, the strength of the material is exceeded and surface fracture occurs leading to loss of material.

Acceleration period – During period II, there is a steep linear rise which corresponds to the period where the rate of erosion is at its maximum as crack growth proceeds. This is due to the degree of splitting, shearing and tearing action on the material caused by the formation of internal tension at the end of the incubation phase exceeding the strength of the material [72].

Deceleration Period – In zone III, the mass-loss rate decreases and then after a certain amount of time it reaches a steady period. In some materials, this period can consist of oscillating rate periods [70-72].

Steady-State Period – For zone IV, the material erosion rate reaches a steady period, where the rate of crack nucleation and propagation becomes constant for the remainder of the

exposure time [70]. Furthermore, this is because the surface, that has already strongly fractured, reduces the probability of an implosion close to the surface. The fractured surface acts as a protective cushion. As a result, this leads to erosion at a lower steady rate [70-72].

The cavitation erosion process is the result of both mechanical and electrochemical action. It is a very complex phenomenon that depends not only on the type and unsteadiness of the cavitation but also on the response of the material to the cavitation energy [70]. The shock waves generated due to the cavitation erosion process impinge on the adjacent metal surface and lead to the breaking of the material bonds. It firstly produces compressive stresses on the surface of the material, and then when it is reflected, it produces tensile stresses that are normal to the surface. Any system that repeats this tensile and compressive stress pattern is subjected to cavitation wear. Cavitation wear is similar to surface fatigue wear, therefore, hard ductile materials that can resist surface fatigue also resist cavitation damage [70, 72].

In cavitation wear, the micro-cracks formed propagate to the point where the material can no longer withstand the impulsed load due to the imploding vapour bubbles imposed. This causes the particles to finally break off. As with fatigue failure, the micro-cracks first form at the stress risers, (notches, undercuts, weld defects etc.) or heterogeneous areas of the material such as at inclusions etc. Hence, if the surface is rough, it is prone to suffer more cavitation wear [72].

2.4 Introduction to electromagnetic treatment

Fatigue is thought of as an inevitable and irreversible process that metallic components undergo and as such metallic materials may be difficult or impossible to remanufacture. Repetitive stresses create micro-flaws leading to fatigue damage and failure. Extending the fatigue life can be accomplished by reducing the magnitude of the stress the material is exposed to or by improving the material properties. Reducing the magnitude of the induced stress can be easily achieved by increasing the size of a component or structure. However, this will introduce a weight penalty and as a result higher fuel consumption and an increase in greenhouse gas emissions. In addition, the structure or component will operate at a higher operational cost. Therefore, today's challenge is to increase resistance against fatigue while sticking to existing optimised structural designs and keeping costs to a minimum.

A number of methods are used by industry to increase the fatigue life; these methods include nitriding, carburising, high-frequency quenching and shot-peening. These techniques increase the fatigue life by increasing surface hardness and by producing compressive residual stresses at the surface of the material without added weight penalty [3, 4]. However, some of these methods can be expensive, time-consuming and may require high levels of energy [5].

Recent research has shown that improvement in fatigue resistance can be achieved by application of various processes that are collectively referred to as electromagnetic treatments (ET) [3, 6-8] and are based on the application of either a high magnetic field or a high current density. Winterton is considered to be the first person to investigate the effect of a saturated magnetic field on the fatigue behaviour of carbon steel in 1959. Since then, there has been an intensive amount of investigations applying ET in the form of a static magnetic field [11]. These techniques have been shown to be successful in relaxing stresses, improving fatigue resistance and improving various mechanical properties. ET can be applied in the form of electropulsing and pulsed magnetic field treatment [16]. The latter process is considered to be more economical in generating a pulse or pulses of a high energy magnetic field than static magnetic field treatment [11, 17]. Pulses of high current density can be achieved through the application of electropulsing to materials and has been shown to transfer input energy from the external environment to reorganise or repair microstructural fatigue damage [18]. Troitskii pioneered in the use of electropulsing for metallic alloys and subsequent studies have shown that the process can extend the fatigue life of steel [4, 13, 15, 19-21], copper [6], titanium [22, 23], aluminium alloys [24] and various other types of structures [11, 26, 27]. In comparison to conventional processes like heat-treatment, magnetic field and electropulsing are easy to apply and control [28] and the treatment time is of significantly lower duration [29].

The improvement of fatigue life by electromagnetic field treatment can be attributed to various mechanisms including dislocation movement [3], Joule heating [4, 18, 22], stress relaxation [20, 22, 30] and crack-healing [15, 21, 31]. However, there are also several studies that have shown that ET can reduce the fatigue life of metallic alloys [21, 32, 33]. Such detrimental effects have been suggested to occur due to overheating that can cause damage

due to melting. Hence, to maximise the effect of ET on fatigue properties, optimum parameters need to be identified and implemented.

Much of the early research work on the use of magnetic field treatment and electropulsing took place in the former Soviet Union. Owing to their potential, both types of techniques are currently under investigation in the United States of America (USA), China and Europe. This literature review outlines the benefits of the two techniques as reported in the literature and discusses the proposed mechanisms that have led to improved fatigue resistance of metallic alloys. The chapter analyses mechanisms based on fatigue crack healing as well as changes to residual stress and microstructure. In the final section, the challenges and problems that remain before this type of technology is commercialised are discussed.

2.4.1 Effect of electromagnetic treatment on fatigue resistance

An inspection of the literature has revealed that there are two main types of electromagnetic treatment that have been used for improvements in fatigue resistance. These are:

1. Magnetic field treatment, in the form of static [3, 73] and alternating magnetic field treatment [3] also referred as eddy current field treatment [31].
2. Electropulsing treatment or direct electric current treatment [4, 13, 15, 18, 20-23, 30, 74-76] involving the application of a pulse of a high-density current through a material.

In some studies of fatigue investigations, electropulsing or magnetic field treatment have been applied at different stages of fatigue life. These studies can be further categorised into four types depending on the stage at which the treatment was applied. These stages include the following:

1. Treatment applied prior to fatigue testing [22].
2. Treatment at specific fatigue (pre-fatigue) levels [3, 4, 13, 15, 16, 18, 20-23, 30, 74-76].
3. Treatment applied at specific continuous periods of the fatigue test [73].

A summary of the findings of key investigations showing improvement in fatigue life due to ET is given in Table 2.2.

Table 2.2. Summary of the beneficial effect of electromagnetic treatment on fatigue life enhancement.

Alloy	Treatment type and parameter	Application period	Improvement in fatigue life
Low carbon steel [16]	Alternating magnetic field 36 mT for 210 s	At 50 % pre-fatigued and after every 100,000 cycles	Over 2 times at 360 MPa and 420 MPa
Medium carbon steel [3]	Alternating magnetic field and static magnetic field 90 ~ 365 mT for20 ~ 240 min	After fatigue tests to 1.2 x 10^5 cycles (roughly equivalent to pre-fatigue of 55)	34 % at 549 MPa under static magnetic field at 365 mT for 60 min 27% at 549 MPa under alternating magnetic field at 90 mT for 60 min
Steel, AISI 4140 [73]	Static magnetic field 80 mT, 130 mT	Continuous treatment from 30% fatigue life to failure and between 30-60 % of average fatigue life of untreated samples	20 % at 630 MPa
Cast hot work die (CHWD) steel [13]	Electropulsing 54 $\frac{MA}{m^2}$, 120 μs	80 % pre-fatigued	140 %
Austenitic stainless steel (SUS31) [4]	Electropulsing 82.76 $\frac{MA}{m^2}$, 0.5 ms	After 2 x 10^5 tensile fatigue cycles (equivalent to pre-fatigue of about 87%)	Extended crack initiation lifetime by 26% at 115 MPa
Austenitic stainless steel (SUS31) [74]	Electropulsing 92.31 $\frac{MA}{m^2}$, 0.5 ms	At 85 % and 43 % pre-fatigued	21 % and 6 % At 115 MPa
Titanium alloy (Ti-6.1 % Al, 2.2 % Cr, 2.7 % Mo) [22]	Electropulsing 150 $\frac{MA}{m^2}$, 50 μs	Before fatigue test	25-50 % at 300-600 MPa
Austenitic stainless steel, 08H18N10T [20]	Electropulsing 8 kA, 20 s	At 62 % pre-fatigued	54 % at 80 MPa
Steel, Fe-0.6C-1Mn-2Si [75]	Electropulsing 290 $\frac{MA}{m^2}$, 15 s	At 70 % pre-fatigued	54 % at 115 MPa
Stainless steel, 0.45C17Mn3Al [30]	Electropulsing 232.5 $\frac{MA}{m^2}$, 25 μs	At 49 % pre-fatigued	72 % at 20 MPa
Steel 40 & Steel 45 and Titanium alloy, VT1-0 [23]	Electropulsing 280 $\frac{MA}{m^2}$, 0 ~ 135 s	Pre-fatigued samples	28 % at 20 MPa

2.4.2 Magnetic field treatment

Fahmy et al. [16] treated low-carbon steel using an alternating magnetic field strength of 36 mT for a total of 210 s and subsequently conducted fatigue tests using a rotating-bending fatigue machine at 360 MPa and 422 MPa stress amplitude. At the lower stress amplitude, an alternating magnetic field treatment was applied at half the estimated fatigue life. For the higher stress amplitude, the treatment was applied at 100,000 cycle intervals. The fatigue life of low-carbon steel was reported to increase by more than two times in comparison to the untreated samples. The authors speculated that the reasons for the extended fatigue life were due to the effect of the magnetic field inducing strain (magnetostriction). This in turn caused dislocation motion and/or changes in the dislocation density of the steel alloy, however, no microscopic evidence or dislocation density calculations were provided. The observed delay in fatigue crack initiation was attributed to the rearrangement of the magnetic domains which promoted dislocation mobility.

A comparatively higher magnetic field intensity was used by Bao-Tong et al. to treat medium-carbon steel after a pre-fatigue level of 55 %. The application of an alternating magnetic field was shown to be effective for improving the fatigue life. For example, when the authors applied an alternating magnetic field of 90 mT, the fatigue life improved by 28%. When the author's increased the intensity of the alternating magnetic field the to 180 mT and 320 mT, the fatigue life decreased lower than the untreated condition by 3% and 10%. To explain the decrease in the fatigue life, Bao-Tong et al. suggested that it is due to the higher level of alternating magnetic field treatment, causing a higher amount of eddy current produced in the sample. As a result of the higher eddy currents, this has caused excessive heat to be generated, leading to a heavy oxidation effect. Hence causing a decrease in the fatigue life. Furthermore, Bao-Tong et al. investigation, studied the combination of treatment intensity and time are critical parameters for achieving optimal fatigue life enhancement as well as investigating the difference between alternating magnetic field and static magnetic field. For example, when a static magnetic field was used for 60 $mins$, a magnetic field intensity of 90 mT had no effect at all, while at 135 mT an increase in the fatigue life by 34 % was reported. However, application of 365 mT increased the fatigue life by only 14 %. It is not clear why there was no effect at the lower intensity, but this observation suggested that there may be a threshold value which needs to be exceeded in order to activate the influential mechanisms

that lead to improvement in the fatigue life. Like in the earlier study by Fahmy et al. , it was suggested that magnetostriction may have been active, but Bao-Tong et al. also proposed another possible mechanism based on the electroplasticity effect due to eddy currents from the application of an alternating magnetic field. However, Bao-Tong et al. only offered an explanation in the cause of the alternating magnetic field. No explanation for the improvement using static magnetic fields were given. A possible reason for the improvement caused by the static magnetic field may be due to alignment in the magnetic domain causing unpinning of dislocations.

A slightly different approach in comparison to the work of these authors [3, 16] was used by Celik et al. who treated AISI 4140 steel with a continuous static magnetic field while running a fatigue test. The intensity of the field was higher than that used by Fahmy et al. [16]. It was observed that the static magnetic field treatment was more effective during the initial stages, particularly when applied before the number of cycles had exceeded 30% of the fatigue life. However, the results suggested that the treatment was not very effective during the latter stages of fatigue life. It was also apparent the fatigue life was further extended when the magnetic field intensity increased to 130 mT from 80 mT. Using atomic force microscopy (AFM), alignment of the magnetic domains was observed in a treated alloy that had been exposed to a static magnetic field treatment of 80 mT, thus confirming the speculative proposed mechanism of Fahmy et al. and Boa-Tong et al. [3]. It was further proposed that the alignment of the domain walls reduced the number of obstacles opposing dislocation movement and thus made dislocation movement easier. As a result, the time required for the formation of slip bands was prolonged and this consequently delayed fatigue crack initiation. In more recent work, Zhao-Long et al. proposed an analytical model to correlate the effect of the magnetic field intensity with fatigue life. This model was developed by using the non-equilibrium statistical theory of fatigue fracture and the results were consistent with the experimental data of both Fahmy et al. and Celik et al. [73]. The model also suggested that fatigue life increased with increase in magnetic field intensity. However, the model was limited to the use of a static magnetic field treatment only and did not address the possibility of any adverse effects due to the application of excessive treatment intensity.

2.4.3 Electropulsing treatment

Electropulsing was used by Zhao et al. as a means to enhance the thermal fatigue life of a hot-work tool steel. Surprisingly, the authors did not state the temperature at which the thermal fatigue tests were carried out, but they refer to earlier work of theirs in which temperatures up to 580ºC were employed. By applying a relatively low current density of 54 $\frac{MA}{m^2}$ at a pulse time of 120 μs and treating notched samples after a number of cycles equivalent to 80% of fatigue crack initiation life, there was an increase in the time taken for crack initiation. In addition, there was a significant decrease (of about 50%) in the crack propagation velocity following electropulsing. The authors [13] showed that electropulsing had induced a circular heat-affected zone (HAZ) (Figure 2.5) at the notch root of the sample due to high-speed heating and cooling; in other words, fast quenching had taken place. The resulting microstructure of the HAZ was composed of superfine martensite and of an fine-grained carbon compound. Though not reported by the authors , judging from the composition of the hot-work tool steel, this fine-grained carbon-containing phase must be composed of chromium carbide and/or molybdenum carbide. It was proposed that this microstructural change was advantageous in enhancing the durability of the material as the presence of fine-grained martensite (and the carbides) suppressed crack initiation and crack growth. Crack growth retardation and crack healing due to grain refinement of a similar hot-work tool steel was also reported in later work to emerge from the same lab by Lin et al. who postulated that these observations were accompanied by an increase in dislocation density in the area close to the notch/crack. In both studies, the benefit was achieved by formation of a HAZ that contained refined martensite and carbides; electropulsing had led to heating at the notch/crack to a sufficiently high temperature to form austenite which then transformed to fine martensite and carbides as a result of fast cooling. These are solid-state transformations and did not involve melting of the alloy. This observation was in agreement with earlier work by Zhou et al who reported crack healing of 45 steel (AISI 1045) under electropulsing. However, Lin et al. did observe evidence of melting but only when they increased the discharging duration from 120 μs to 140 μs; undesirable damage was reported as a result of melting. In contrast to these studies, an investigation by Jing et al. showed that a healing effect could be achieved by formation of a HAZ through fusion under electropulsing of a precipitation hardened martensitic stainless steel. Therefore, the presence of melting can sometimes lead to positive effects and at other times to negative effects. It is clear that more

research is warranted to fully understand and to control the effects of melting due to electropulsing. As the level of heating during the treatment is likely to differ depending not only on the material/microstructure but also on the size and shape of a crack, this is going to be a very difficult task. The authors of these investigations did not measure the temperature rise during electropulsing and no details of the rate of cooling/quenching have been provided; understandably, this is not easy, but it may provide useful information that may enable prediction of the conditions required to induce the HAZ and to optimise the effect of this treatment. The link between all these studies [13, 18] is that improvement in fatigue resistance was achieved via the precipitation of fine martensite with, in some cases, carbides; their precipitation was reported to be the result of slow defussion as a result of electropulsing.

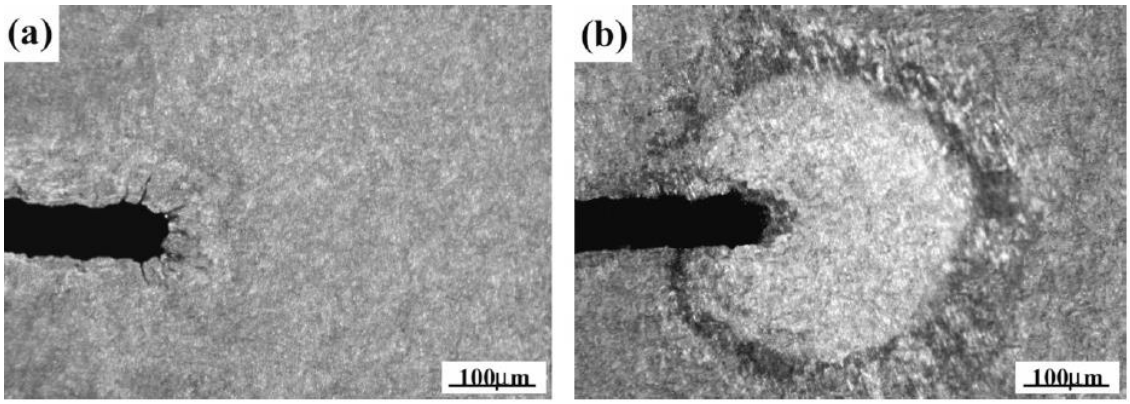

(a) (b)

Figure 2.5. The thermal fatigue (TF) crack morphologies of the samples treated without and with current pulse after 600 cycles. (a) the untreated sample and (b) the sample treated with a current pulse [13].

The other major effect attributed to electropulsing and leading to improvement in the fatigue resistance of metals is based on recovery and relaxation that was accompanied by changes to the defect structure (principally dislocations). In a recent study, Tang et al. investigated the effect of electropulsing on the fatigue behaviour of a notched stainless steel (SUS31) plate. The study focused on the time taken for crack initiation (i.e. the number of cycles required for the crack to initiate) to take place at the notched area under tensile-tensile fatigue test conditions. It was shown that at a stress level of 115 MPa, the crack initiation period was delayed by 26 % when electropulsing at 3 kA for 0.5 ms had been applied to samples after 2

x 10^5 cycles of pre-fatigue (equivalent to about 87 % of the crack initiation period of the untreated samples). From the digital image correlation results shown in Figure 2.6, relaxation of the residual plastic strain (ε_{yy}) parallel to the loading direction was observed in the electropulsed sample. Based on their findings, the authors [4] suggested that the electropulsing treatment had led to the recovery of residual plastic strain around the crack notch. This was confirmed by observation of a reduction in the dislocation density around the notch (Figure 2.7) of a treated specimen. The change in dislocation density as shown by the use of TEM, revealed the origin of the healing effect around the notch. These authors used a higher current density and a lower pulse time in comparison to the parameters used by Zhao et al. and did not report any formation of a HAZ in the region around the healed crack.

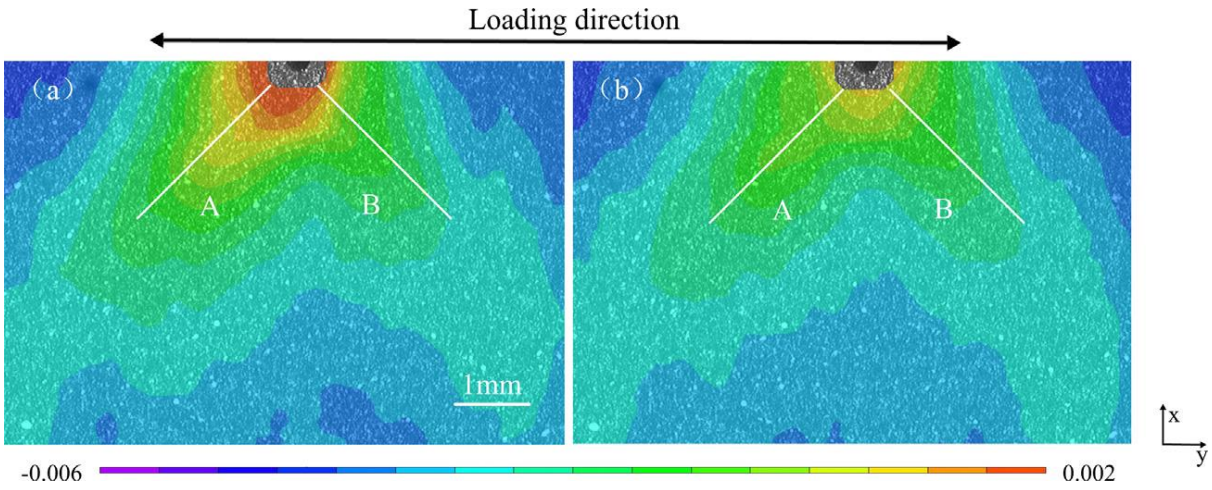

(a) (b)

Figure 2.6. Distribution of plastic strain around a notch tip: (a) strain ($\boldsymbol{\varepsilon_{yy}}$) before the application of electric current; and (b) strain ($\boldsymbol{\varepsilon_{yy}}$) after the application of electric current. [4].

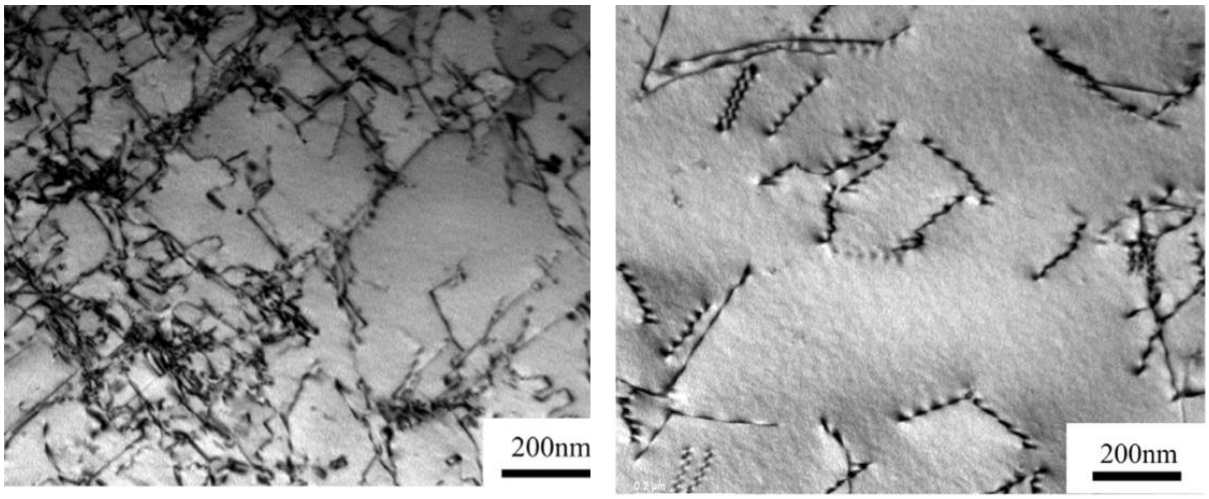

(a) (b)

Figure 2.7. Typical TEM image of the dislocation structure observed after the fatigue test (a) Untreated and (b) after electropulsing [4].

In another study also conducted by the same group on SUS316 stainless steel under the same electropulsing conditions (3kA for 0.5 $\boldsymbol{ms}$), it was observed that electropulsing could delay the time for fatigue crack initiation. Atomic force microscopy (AFM) was em**ployed to analyse slip bands in a pre-fatigued sample before and after electropulsing (**Figure 2.8). The results taken from exactly the same area indicated that the step height of the slip bands that were formed during the cyclic loading had decreased following electropulsing; in addition, some slip bands seemed to have disappeared. It was proposed that the effect of the treatment had been achieved by dislocation motion due to electron wind drag and by thermal stress from high-speed heating. TEM observations also concluded that the delaying effect induced by the electric current on the fatigue crack initiation period was also related to a decrease in the dislocation density. This observation was in good agreement with the fatigue crack initiation model of Tanaka and Mura who attributed the delay of fatigue damage to a reduction in the dislocation density. Further evidence of the beneficial effect of persistent slip band spacing was provided by Conrad and co-workers [77, 78] who applied 2 electropulses per second at a duration of 100 μs and a current density of 10 $\frac{\boldsymbol{MA}}{\boldsymbol{m^2}}$ during rotation bending fatigue of pure copper. A delay in crack initiation was reported leading to an increase in fatigue life due to electropulsing during the fatigue test. While the volume fraction of the persistent slip bands remained the same as that for the untreated sample, the slip band spacing and width

decreased by about 30% as a result of the electropulses. This decrease occurred just after the start of the electropulsing treatment. These authors [77, 78] made a very interesting observation in that there was significant reduction in intergranular cracking relative to transgranular cracking. The improved fatigue resistance and the decrease in the intergranular cracking were attributed to an increased homogenisation of slip (due to the reduction in the slip band spacing and width). Slip homogenisation was proposed to be the result of increased dislocation mobility caused by interaction between drift electrons (from the applied current) and the active dislocations.

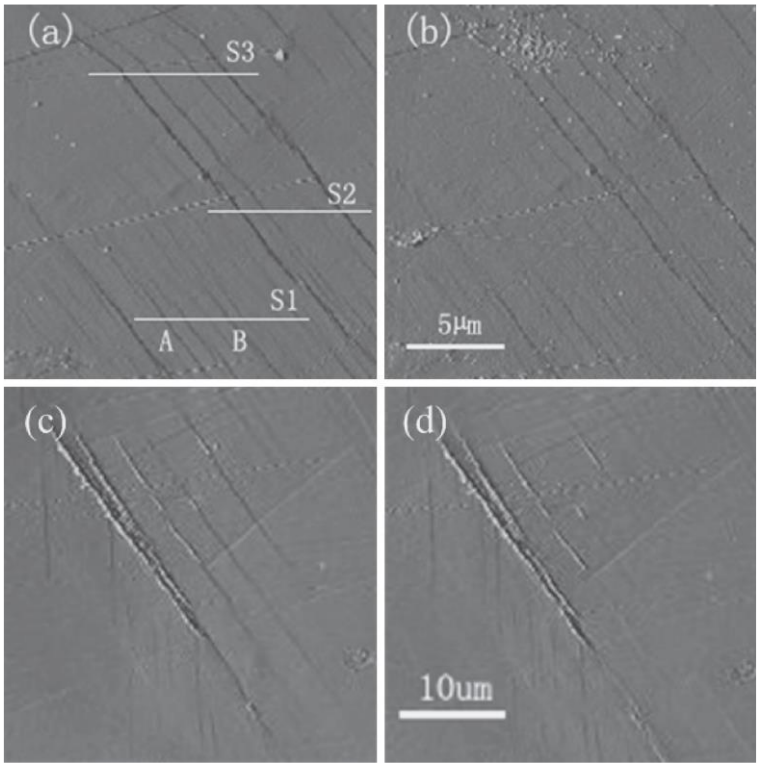

Figure 2.8. AFM micrographs of the surface relief areas: (a) before and (b) after the application of electropulsing (higher magnification; (c) before and (d) after the application of electropulsing (higher magnification) [74].

The idea of homogenisation playing a part in improving the fatigue life of titanium alloy Ti-6.1%Al-2.2%Cr-2.7%Mo was also put forward by Levitin et al. [22]. The specimens had been grit-blasted using steel balls that were vibrated ultrasonically to produce compressive residual

stresses on the surface. They were subsequently electropulsed at a current density of 150 $\frac{MA}{m^2}$ for a pulse time of 50 μs before fatigue testing. By using this approach, the fatigue life was reported to increase by 25-50%, though the electropulsing treatment had led to a reduction in the compressive residual stress (as determined by X-ray diffraction). However, they also reported an increase in microstresses within crystallites. It was further suggested that the residual stresses had become more uniform throughout the volume of the electropulsed samples making them microstructurally more homogeneous. The recorded temperature during electropulsing was between 77 $°C$ between 247 $°C$, but such temperatures are too low for stress relaxation for this alloy. It was argued that heating had occurred at areas of high electrical resistance like defects. In a recent investigation, Xu et al. supported the idea of local temperature increases due to Joule heating around micro-defects. Observations of local melting appeared at the vicinity of the microcracks, indicating local heating to occur due to the treatment.

Sosnin et al. applied electropulsing treatment to 08H18N10T austenitic stainless steel and to 45G17Yu3 precipitation-hardened steel at pre-fatigue levels of 62% and 69%, respectively. It was shown that the application of a treatment of 8 kA for 20 s to 08H18N10T austenitic stainless steel led to an improvement in the fatigue life of 54 % at a stress amplitude of 80 MPa. An even higher improvement was achieved for 45G17Yu3 steel at a stress amplitude of 20 MPa when using an electropulse of 9.3 kA for 70 s. Unfortunately these researchers [20] provided no details of the current density and the geometry of the samples. Transmission electron microscopy for 08H18N10T austenitic stainless steel showed that electropulsing improved the fatigue resistance by factors involving (i) retardation of the dislocation substructure growth, (ii) reducing the development of martensitic transformation of austenite, (iii) inducing disintegration of the solid solution by precipitation of TiC particles and (iv) reducing the internal field stress amplitude. In the case of 45G17Yu3 austenitic steel, electropulsing was reported to enhance the fatigue life by (i) stress relaxation due to the combined effect of reconstruction of grain structure; (ii) annihilation of dislocations and reconstruction of dislocation substructures; (iii) formation of micro-twins (probably as a result of thermal-stress); (iv) healing of stress concentrators; and (v) suppressing the martensitic transformation. The annihilation of dislocations due to electropulsing has also been observed in another study by the same authors involving the use of electropulsing at 70 % pre-fatigued

notched steel (Fe-0.6C-1Mn-2Si) by applying a current density of 290 $\frac{MA}{m^2}$ for 15 s which is a higher intensity than that used by Levitin et al. [22]. The recorded improvement in the fatigue life was 54 %. Microstructural analysis showed that the electropulsing treatment promoted the relaxation of stress concentration through the dissolution of particles localised at the grain boundaries. This treatment also strengthened the steel by formation of globular pearlite and by increasing the scalar dislocation density. These effects eventually caused the mean and maximum subcritical crack length for fatigue to increase. Both these studies by Sosnin et al. support previous observations by Levitin et al. who suggested that electropulsing repairs the fatigue damage by causing a reduction of the residual stress.

Improvement in the fatigue life of stainless steel (0.45C17Mn3Al) following electropulsing has also been shown to take place by Konovalov et al. [30]. A treatment of 232.5 $\frac{MA}{m^2}$ for 25 μs, at a pre-fatigue level of 49 % produced an increase in fatigue life of 72 %. The use of TEM revealed that the electropulsing treatment had led to one of the most powerful stress concentrators in the crystal lattice structure to relax and this was thought to delay fatigue crack initiation. In another study, the same researchers varied the pulse time of the treatment from 0-135 s to examine the effect of the duration of the treatment of the fatigue resistance. A current density of 280 $\frac{MA}{m^2}$ was applied to pre-fatigued samples of medium carbon steel (steel 40, steel 45) and titanium alloy (VT1-0). The maximum increase in the fatigue life of steel 45 was recorded to be 28 %, when the pulsing time was set to between 45-70 s. The authors suggested that the electro-plastic effect was most prominent when the treatment duration reached 70 s. However, when increasing the treatment time to 135 s, the fatigue life decreased by 10 %. It was speculated that the decrease in fatigue life was attributed to the increase in the temperature. The authors, however, did not show any evidence of there being any thermal effect.

2.5 Effects of electromagnetic processing on the tribology of the material

There have been several research investigations on the effects of magnetic field treatment on the mechanical and tribological properties of materials. Tests conducted by Snegovskij et al.

showed that after magnetically treating propellers, the wear resistance capability increased by 1.5-2 times compared to untreated samples. More recent work by Babutskyi et al. reported that the coefficient of friction of magnetically treated AISI 52100 steel was reduced on average by 13% compared to untreated specimens. It was shown that the width of the wear tracks from pin-on-disc tests was greater for the untreated disc specimens in comparison to the treated ones as shown in Figure 2.9. The average wear track width for the untreated samples was 137 μm, while a value of 80 μm (24% reduction) was recorded for the treated ones.

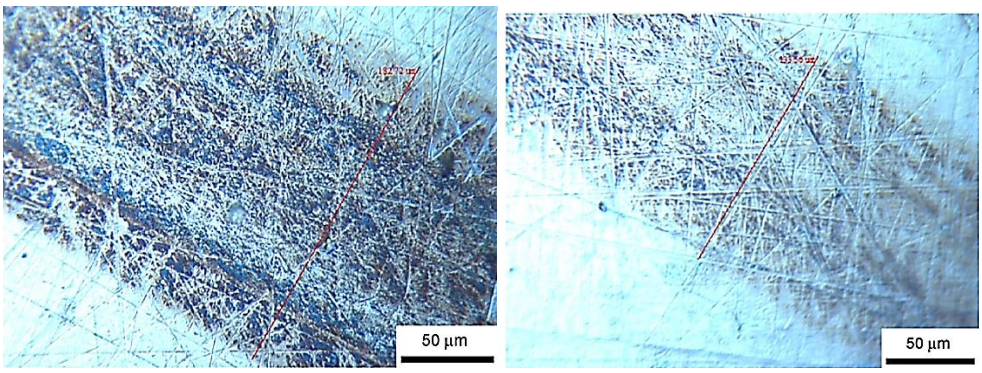

(a) (b)

Figure 2.9. Wear tracks on the surface of the untreated (a) and treated (b) disc specimens.

Babutskyi et al. suggested that the improvement in the coefficient of friction was attributed to reduction in residual stress and destabilization of the retained austenite in steel. However, no residual stress measurements or microscopic evidence was provided. In a study by Xi et al. , the effect of magnetic field treatment on the tribological behaviour of AISI 1045 steel was investigated. In the study, a pulsed magnetic field of 32 mT was applied for 30 s prior to friction testing. The authors observed that the coefficient of friction had dropped by 16.4% in the treated samples. Furthermore, microhardness tests were performed before and after treatment and an increase of 8% in the Vickers microhardness was measured. The decrease in the coefficient of friction was attributed to an increase in dislocation density by 16.5% which was calculated using the Williamson -Hall method. In addition, X-ray diffraction and microstructural evidence showed that the average crystallite size of ferrite in the treated samples was lower. These results can further contribute to the improved abrasion-resistant mechanism exhibited after treatment. While their investigation [79], showed very promising results, no theory was presented to explain the observed improvements.

2.6 Effect of electromagnetic processing on residual stress

It has been well-documented that electromagnetic treatment causes relaxation of residual stress. Tang et al. [12, 80, 81] conducted systematic research which showed that residual stress was reduced by nearly 40% following the application of strong pulsed magnetic treatment in HT70 steel. Tang et al. [12, 81] argued that stress relaxation was due to dynamic magnetostriction which provided the energy for inelastic strain movement via magnetoelastic coupling. Klamecki, [82] also observed reduction in residual stress by using pulsed magnetic field treatment for both low-stressed and high-stressed 1070 steel specimens. For specimens with lower initial stress levels, a 4-7% reduction in residual stresses was reported while for samples with higher initial stress levels, a decrease of 8-13% was observed. It was also stated that cyclic magnetostriction caused dislocation movement and changes in microstructure due to application of the magnetic field. In recent studies conducted by Cai et al. [29, 83], the use of a combination of both pulsed electric current and pulsed magnetic fields has led to significant residual stress reduction. It was proposed that this result was due to dislocations moving faster and more efficiently. These results that are summarised in Figure 2.10 showed that by carrying out pulsed magnetic field treatment there was only 10% residual stress reduction, however, there was a 20% increase in residual stress by pulse electric current treatment. The combination of both treatments increased residual stress release by up to 60%.

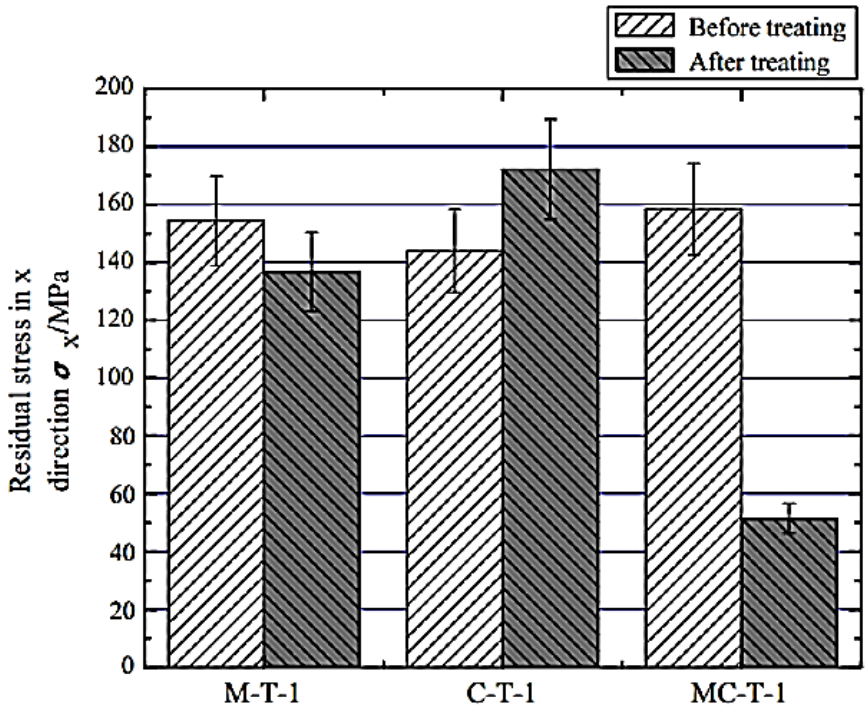

Figure 2.10. Average residual stress changes caused by Magnetic Field Treatment (M-T), Pulsed Electric Current Treatment (C-T) and Magnetic Field and Pulsed Electric Current Treatment (MC-T) [83].

It was proposed that there was an electro-magneto-plasticity influencing the dislocation movement; the proposed mechanism was based on the magneto-plastic theory and electro-plastic theory. This theory suggests that the treatment may provide a condition for dislocation depinning to occur. As for pulsed electric current treatment, this may provide conduction for electrons to drive the movement of dislocations, leading to a reduction of residual stresses [29, 83].

2.7 Effect of electromagnetic processing on micro plastic deformation

Electropulsing has been reported by Hosoi et al. to lead to fatigue crack healing of austenite stainless steel SUS316NG. Figure 2.11 shows the effect of the treatment at the crack tip before and after high density electric current treatment. The crack closure phenomenon that was observed was reported to be due to Joule heating that was generated by the high-density

electric field. When an electric current pass through a crack, the current flows along the crack due to the presence of electrical resistance at the crack surface. Hence, a high density electric current field is generated at the crack tip. This leads to the area at the tip and the vicinity of the crack to be heated rapidly and to expand due to Joule heating. This thermal expansion has been reported to cause compressive stresses to exceed the yield point and hence cause crack closure [15, 84].

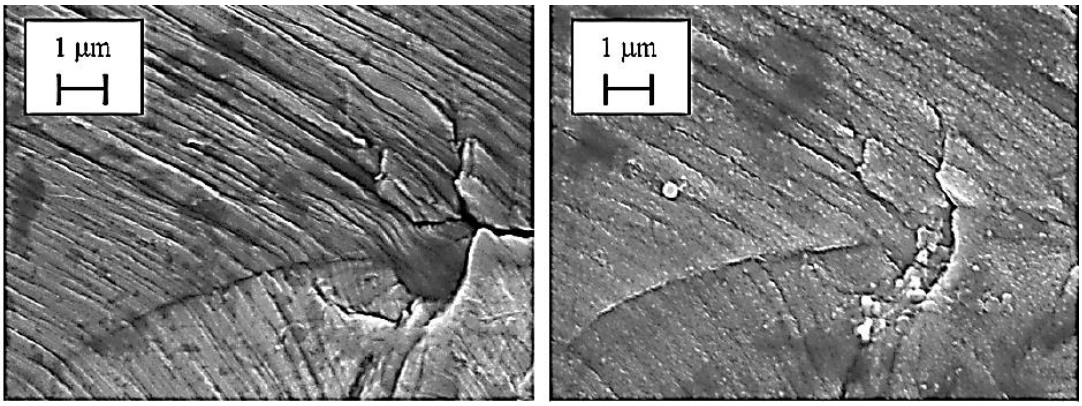

(a) (b)

Figure 2.11. SEM magnified images of the crack tips (a) before and (b) after the application of the electric current [18].

In work conducted by Cai et al. , the effects of plastic deformation caused by pulsed magnetic treatment on medium carbon steel were investigated. Using scanning electron microscopy (SEM) it was observed that the magnetic field caused plastic deformation within the grains as shown in Figure 2.12. The average plastic deformation within a length of 4 mm was reported to be not more than 0.1 μm.

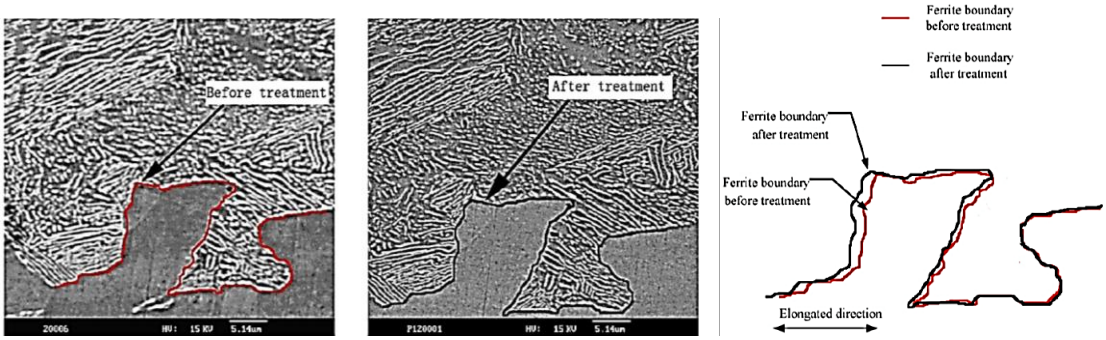

(a) (b) (c)

Figure 2.12. SEM images contrasting micro-deformation (a) Micro-structures before magnetic field treatment (b) Micro-structures after magnetic field treatment (c) Overlapped reference curves [85].

By using X-ray diffraction (XRD) Cai et al. also calculated the residual stress before and after treatment. A 12-24% decrease in residual stress was reported as a result of the PMF treatment. It was also observed that the magnetic field treatment caused plastic deformation within the grains. When comparing heat treatment to PMF treatment, the behaviour of plastic deformation and residual stress relaxation were different. With heat treatment, stress was released through the material continually and plastic deformation in the adjacent area was nearly uniform. However, when PMF treatment was used it was suggested that stress relief took place within some selected grains instead of the entire sample. The effect of magnetic field treatment was explained by consideration of the magneto-plastic effect which is due to the motion of dislocations in crystals when exposed to magnetic fields [86]. The magneto-plastic effect is determined by certain conditions, including the magnetic field flux density, the mean free path of dislocations, the magnetic field treatment time, the induced direction of the magnetic field and the temperature [29, 85, 86].

2.8 Threats and challenges to electromagnetic treatment

Despite the positive impact of electromagnetic treatment (ET) as outlined in this literature review, there are still concerns with regard to the correct treatment parameters that need to be applied. Furthermore, the main question concerning many researchers in this field is whether:

- the application of an external magnetic or electric energy improves the fatigue resistance of metals and alloys [73, 87, 88]?

While several investigations have indicated that ET can extend fatigue resistance, there is also evidence in the literature that detrimental effects are possible due to ET [16, 20, 24, 31, 32, 89]. The observation of adverse effects has been attributed by some researchers to the excessive levels of intensity, while others have argued that exceeding a critical point during treatment can lead to microstructural damage and reduced fatigue life. Some studies have also shown that ET can only repair fatigue damage if the initial damage prior to the treatment does not exceed some critical level or the intensity of the treatment does not approach a certain "saturation limit" [3, 32, 73, 90]. There is also evidence that the treatment needs to reach a minimum level or threshold point before it starts to extend fatigue life. It is also important to know about the optimum level of treatment in order to maximise fatigue life. Therefore, the real issue faced is to identify the ideal parameters of treatment regarding the type, intensity, time, number of applications and frequency, etc. for the optimisation of fatigue resistance of a given alloy.

The observed detrimental effects have been attributed to a variety of reasons; for example, Bao-Tong et al. observed a reduction of 10 % in the fatigue life of low carbon steel specimens following a exposure to a high alternating magnetic field of 3200 Gs for 20 $mins$. It was suggested that excessive overheating took place as a result of eddy currents which caused heavy oxidation leading to deterioration of the fatigue properties of the material. In a study conducted by Fahmy et al. , there was also decrease in fatigue life of mild steel as the magnetic field increased. In another study, electropulsing was applied to aluminium alloy 6061-T6 using a current density of 150 $\frac{MA}{m^2}$ and this led to the decline of fatigue life by 10%. It was observed that this was the result of damage from melting due to an excessive current density. This study also found that at a higher maximum stress intensity factor, K_{max} of 0.91 $MPa.mm^{1/2}$, a current density of 90 $\frac{MA}{m^2}$ did not have any effect on fatigue life. The reason that was given was that the current density was not sufficiently high enough to achieve crack healing.

Cai et al. have reported that the application of a magnetic field perpendicular to the direction of maximum stress has the potential to release more residual stresses and therefore the field orientation may be an influential parameter in the application of magnetic field treatment.

Celik et al. reported that the pre-fatigue level has a substantial influence effect on the effectiveness of magnetic field treatment and showed that the fatigue life of AISI 4041 steel decreased when the an static magnetic field was applied at a pre-fatigue level above 60 %. Application of the magnetic field after a certain point in the fatigue life led to overheating which was detrimental to the fatigue life. Tang et al. observed that by electropulsing at 43 % of fatigue crack initiation with 3 kA for 5 μs, there was only 6 % improvement in fatigue crack initial life. However, when the treatment was applied at 85 % of the fatigue crack initiation life, there was 21 % improvement in the fatigue crack initiation life showing that the pre-fatigue point at which the treatment was applied was important. The duration of the treatment has also been shown to play a significant role in the effectiveness of electromagnetic treatment. For example, by applying electropulsing treatment to titanium alloy VT1-0 at a current density of 280 $\frac{MA}{m^2}$ for a duration of 135 s led to negative effects in contrast to a treatment of 70 s [23]. According the authors the fatigue life of the alloy was reduced by 10 % due to the excessive time of treatment. In another study, Hosoi et al. showed that for a high number of electropulses, crack acceleration took place because electropulsing led to crack growth acceleration by inducing tensile residual stress around the crack tip [21]. An investigation by Yang et al. demonstrated the importance of the direction of the treatment in relation to the direction of the crack growth. Their work showed that the application of eddy currents to repair fatigue cracks worked best when applied perpendicular to the crack. In addition, no crack healing observed on fatigue crack repairing when the eddy currents were applied in the radial direction of the fatigue crack as there was no eddy current detouring effect [31]. All these results suggest that there is a need for controlling the ET parameters to achieve fatigue life enhancement.

Previous research studies have demonstrated that the increase in the magnitude of ET can introduce a desirable fatigue resistance in metals. However, very little research has been done which isolates variable parameters, such as the intensity of treatment, the number of treatment applications and the pre-treated conditions of the alloy. Isolating the variable

parameters can establish how the ET parameters affect the properties of the metal derive a relationship between the variables and fatigue resistance to identify the optimal treatment parameters. Another factor not mentioned in the literature that also needs to be considered is the alloy initial condition. Understanding if the treatment works best for alloys that are annealed, cold-worked or pre-stressed are key points that must be considered when trying to determine the optimal treatment parameters.

2.9 Conclusions

In light of the findings mentioned in this review, it seems that there are several types of electromagnetic treatments with varying parameters. The results have mainly shown a beneficial effect of electromagnetic field treatment on fatigue properties, wear and residual stresses of the metallic alloys. However, the problems now faced with electromagnetic field treatment are the understanding of the underlying mechanisms and the establishment of treatment parameters, e.g., current density, pulse time and the number of pulses, which will produce the maximum improvement of a given alloy. Furthermore, one thing that is common in all studies in the literature review is the use of highly sophisticated and specialized equipment to treat the alloys. In addition, the use of a high-density electric current can be dangerous to the operator and would require additional health and safety measures to keep the operator safe. Therefore, this research will investigate the effects of alternating magnetic field treatment on metallic alloys and what causes the change in the mechanical properties. As mentioned in this review, there have been several studies that have investigated the effects of pulsed magnetic field treatment and electropulsing, however, not much work has been done using alternating magnetic field treatment. Subsequently, the technique that is investigated in this research varies from previous research as it uses an alternating magnetic field to treat the alloys. Alternating magnetic field treatment differs from earlier work as it uses simpler equipment and is more cost-effective in comparison with pulsed magnetic treatment and electropulsing. Furthermore, alternating magnetic field treatment is a lot safer to use and requires fewer health and safety measures as the current density applied is low. In addition, some of the studies have been limited to testing only a select few materials and testing limited properties. In this research study, alternating magnetic field treatment was applied to alloys of different magnetic nature.

Moreover, there have been several studies investigating the effects of ET on the fatigue resistance of metallic alloys, however, very few studies have investigated the effects of ET on wear and cavitation erosion. Both sliding contact wear and cavitation erosion are cyclic loadings in nature. As with fatigue failure, wear and cavitation erosion failure initiation points can be caused by the presence residual stress or defects on the surface of the material [72]. To mitigate and alter these defects, ET has shown to have promising results. Hence cavitation erosion, fatigue and sliding contact wear tests were used as a means to compare the performance of the untreated and treated materials.

2.10 Aim and objectives

The aim of this research is to investigate the effect of alternating magnetic field treatment on the mechanical properties of metallic alloys using alternating magnetic field treatment.

The main objectives of this research involve:

- Designing electromagnetic field treatment equipment for treating metallic alloys. These techniques include alternating magnetic field treatment.

- Conducting experimental research to understand the effects of alternating magnetic field treatment on the fatigue life of aluminium alloy 2014-T6 and medium carbon steel (EN8 steel).

- Evaluating the effect of alternating magnetic field treatment on the wear behaviour of EN8 steel, nickel-aluminium bronze and aluminium alloy 2014-T6.

- Understanding the effects of alternating magnetic field treatments on the cavitation erosion of aluminium alloy 2014-T6, nickel aluminium-bronze, 70/30 brass and EN8 steel.

- Studying the detailed mechanisms alternating magnetic field treatments and how they affect the cavitation erosion behaviour of various alloys.

3 Design of a state of the art Electromagnetic Field Treatment equipment

3.1 Introduction

The use of various types of electromagnetic treatment processes for alloys in the solid-state have been documented in the literature [14, 80, 91, 92] and include electropulsing, magnetic pulse treatment, alternating magnetic field treatment and static magnetic treatment. The treatment variables include current density, the strength of the magnetic field, time, the number of pulses, the duration of each pulse or duration of exposure, etc. Furthermore, all the reported work has been conducted by using equipment that was built in-house by each group of researchers. As a result, there is no "standard" processing equipment for conducting any of the treatments that fall into the category of electromagnetic treatement for metallic alloys. This Chapter describes in detail the design, building and commissioning of the equipment that was used to apply alternating magnetic field treatment in the present study.

3.2 Alternating Magnetic Field treatment

The alternating magnetic field treatment equipment consists of two Magnetech Corp electromagnet soft iron cores which were used to create a magnetic field. The sample was placed in the centre between the two cores as shown in Figure 3.1.

(a) (b)

Figure 3.1. Magnetech Corp electromagnet soft iron (a) sample placed in core the middle of the core (b).

An Arduino Uno microcontroller was used to control the magnetisation intervals of each core. The treatment setup is shown in Figure 3.2. During the treatment, one of the cores was magnetised for an interval of 5 seconds. After this, the other core was magnetised for another 5 seconds. During the transition change from magnetising one core and demagnetising the other, eddy currents are induced in the treated sample. The electromagnetic core was powered by a 24V DC supply that was connected to the Arduino Uno microcontroller. The Arduino script was programmed in Arduino IDE using C++ computer language. The programmed script used for the control box of the alternating magnetic field treatment can be found in Appendix A. Three different types of spacers were used in order to accommodate the different sample geometry for each mechanical test. Spacers of thickness of 3.1mm, 6.2mm and 9mm were used for the pin-on-disc, cavitation erosion and fatigue samples respectively. These spacers were used to accommodate each sample between the two cores as each of these tests uses a different sample geometry.

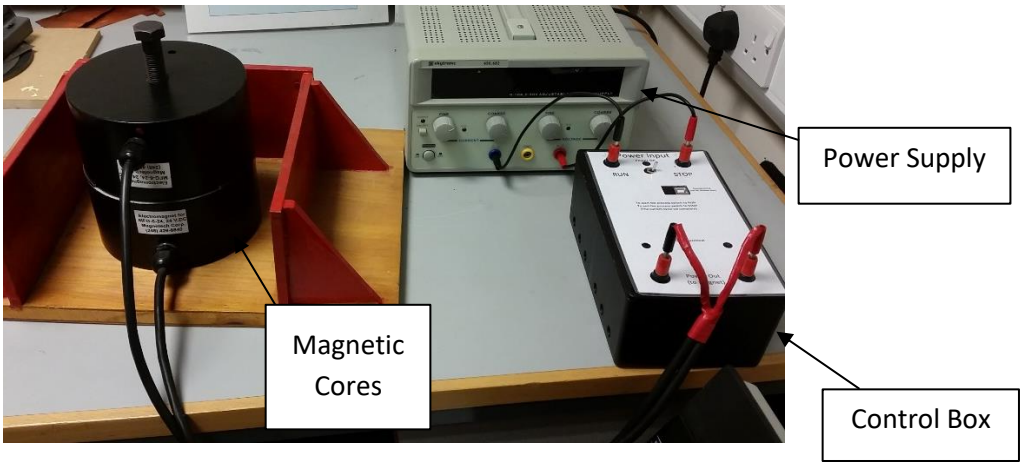

Figure 3.2. Set up of alternating magnetic field treatment rig.

3.2.1 Optimum time treatment conditions for Alternating Magnetic Field treatment

In order to characterise the optimum conditions for alternating magnetic field treatment, Vicker's microhardness testing was conducted before and after treatment. A series of tests were conducted with different magnetising voltages and treatment duration. Microhardness testing was conducted for a 4 mm diameter disc with thickness of 5 mm. The samples had

been ground and polished to a finish of 0.5 µm. Microhardness tests were performed using a Struers DuraScan microhardness tester at a load of 1 N. An average value of 20 indentations across two radii of the circular sample was obtained.

Figure 3.3 shows the microhardness results of the untreated and treated samples at three different magnetising voltages, 8V, 16V and 24V for a fixed treatment duration of 30 minutes. From the results, it can be clearly observed that the highest improvement after treatment was for sample 3 using a magnetising voltage of 24 volts. The percentage increase in hardness was 7.74%. For treatment of sample 1 and sample 2, a magnetising voltage of 8V and 16V was used respectively; these treatments yielded a percentage increase of hardness of 0.49% and 2.34%, respectively. From the results shown in Figure 3.3, the magnetising voltage that was selected for use in the research was 24V.

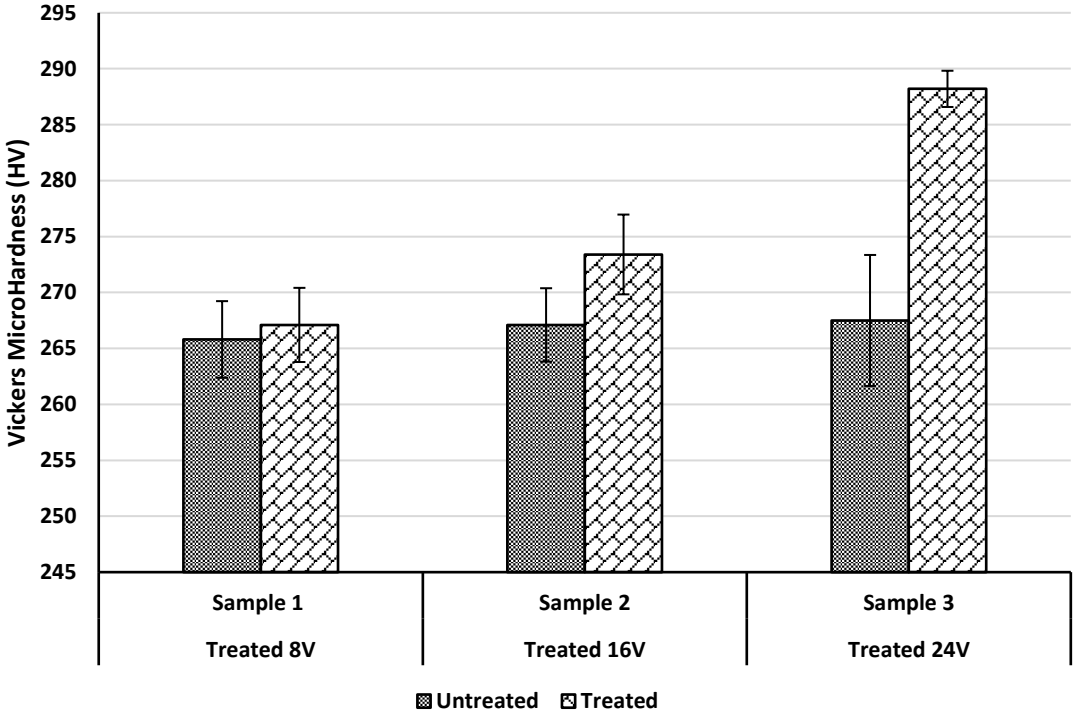

Figure 3.3. Microhardness results for untreated and alternating magnetic field treatment with different treatment voltages 8V, 16V and 24V.

The results shown in Figure 3.4 present the average Vickers microhardness results before and after treatment for the three alternating magnetic field exposure time parameters (15

minutes, 30 minutes and 45 minutes). The results indicate that the highest exposure of 45 minutes gave the best improvement of 7.82% in the microhardness value. However, there was not much difference between the results for a 30-minute (percentage increase of 7.74%) and 45-minute of exposure time. Furthermore, the 30-minute treatment exposure time gave a much lower standard deviation of 1.62 compared to that for the 45-minute exposure time (standard deviation of 3.60). The 15-minute alternating magnetic field treatment only produced a 3.63% improvement in the microhardness. Even though the 30-minute exposure time had resulted in a slightly lower microhardness improvement, it was selected for use in this research on the basis of the lower standard deviation and more uniform results of the measured microhardness values.

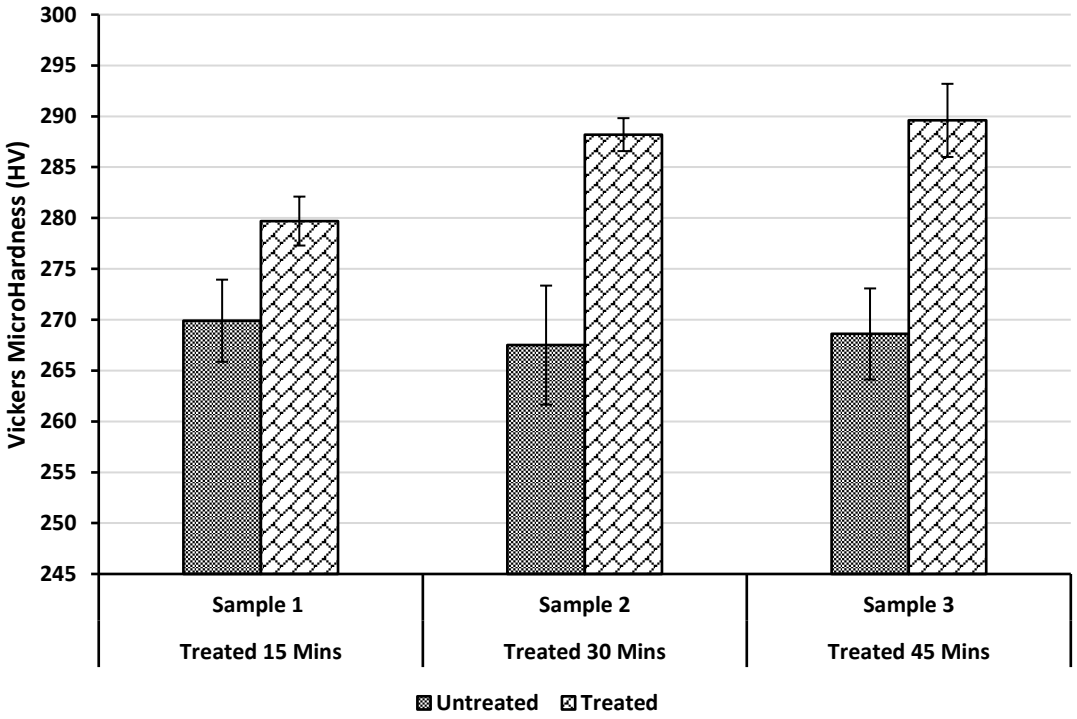

Figure 3.4. Microhardness results for untreated and alternating magnetic field treatment time with different exposure times 15 minutes, 30 minutes and 45 minutes.

3.2.2 Characterization of the Alternating Magnetic Field treatment

Each core was magnetized for a 5-second interval and the total time for this treatment was 30 minutes. The alternating magnetic field was measured with a Hirst GM08 Gaussmeter and

the registration was conducted using a Picoscope 4224 digital oscilloscope. Figure 3.5a, 5b and 5c display the magnetic field directions for the pin-on-disc, cavitation erosion and fatigue test samples. The magnitude of the magnetic field in each case is presented in Figure 3.6a, 6b and 6c. The variation in the magnetic flux density is due to the different spacers used to accommodate each type of test sample inside the core. As thicker spacers are used between the cores, the magnetic flux density is reduced due to increased distance between the two cores. The control box circuit diagram is shown in Figure 3.7.

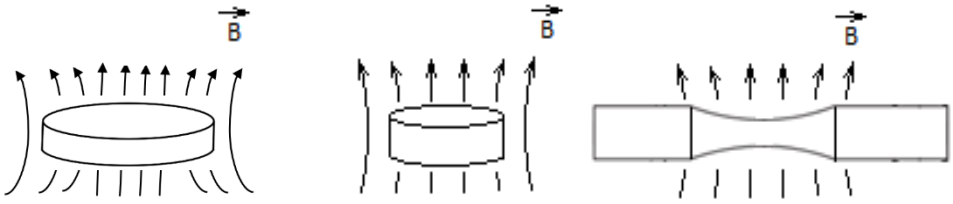

(a) (b) (c)

Figure 3.5. Schematic of treatment for (a) pin-on-disc sample, (b) cavitation erosion sample and (c) fatigue sample.

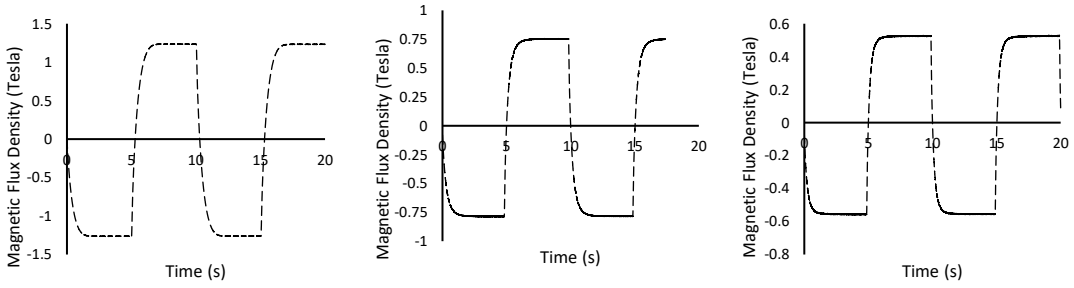

(a) (b) (c)

Figure 3.6. The magnitude of the magnetic flux density for (a) pin-on-disc sample, (b) cavitation erosion sample and (c) fatigue sample.

The temperature rise during treatment was measured for each sample before and after treatment using a K-type thermocouple connected to a Tenma 72-7715 digital thermometer in order to record the temperature increase for each treatment. An average temperature increase that was recorded for each type of sample and material in Table 3.1.

Table 3.1. Temperature rise recorded using a thermocouple during alternating magnetic field treatment.

	EN8 Steel	AA2014-T6	NAB	Brass
Fatigue Sample	12.0°C	14.0°C	N.A.	N.A.
Pin-on-Disc Sample	10.2°C	10.8°C	10.5°C	N.A.
Cavitation Erosion Sample	11.7°C	11.4°C	11.6°C	11.3°C

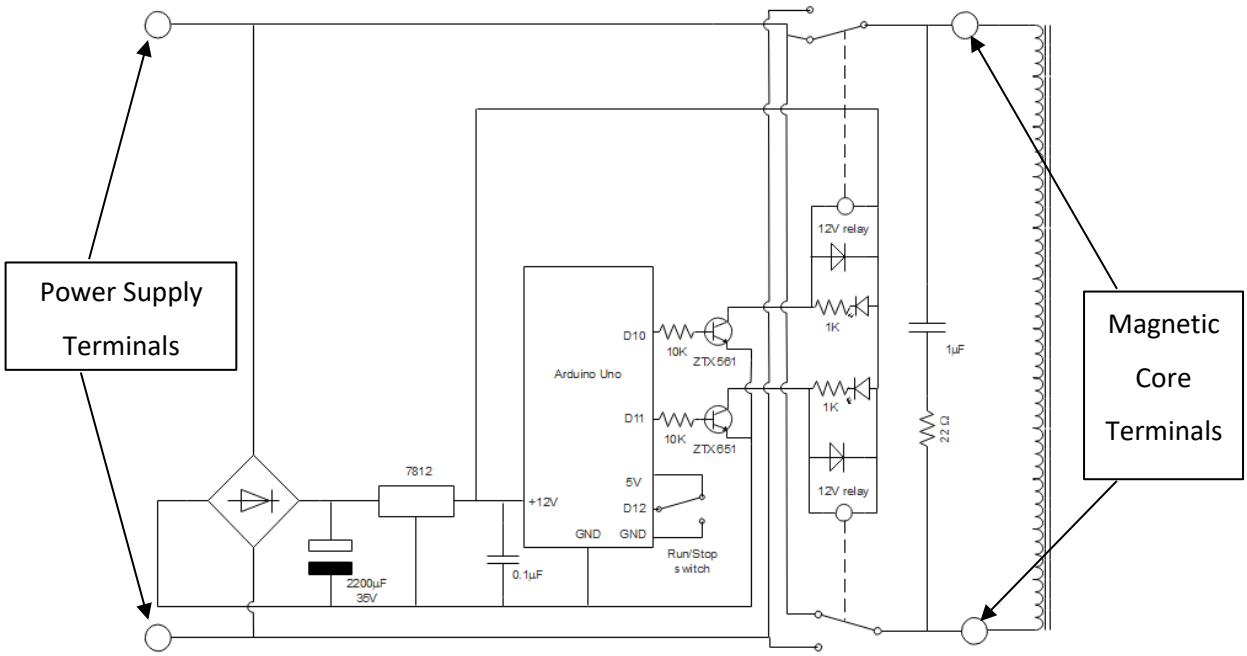

Figure 3.7. Circuit diagram of Alternating magnetic field control box.

This type of treatment is attractive for a number of reasons; firstly it only requires a low amount of voltage as it can be run from a 24V DC power supply compared to other conventional ways of treating materials such as heat-treatment.Secondly, it is potentially cost-effective to manufacture equipment for this type of treatment as the cost of purchasing the cores and the components for the control box is not high. Furthermore, this type of treatment is very simple to run as it does not require advanced training and expertise. This treatment only requires the sample to be placed between the two cores and to turn on the control box. Once the treatment is complete the system is turned off.

4 Methodology

4.1 Introduction

In this Chapter, an outline of the experimental methodology used is described. This research uses the following mechanical tests; cantilever fatigue testing, pin-on-disc wear, cavitation erosion, tensile testing, nano-indentation and micro-hardness as means to benchmark the untreated condition to the treated conditons. The test procedure, test conditions and standards used are described in each section.

To characterize and explain the effects of the treatment, XRD and electrical conductivity measurements were also carried out. Furthermore, failure analysis for fatigue testing cavitation erosion and pin-on-disc wear were performed using SEM on the treated and untreated conditions. TEM was conducted to analyse the microstructure of treated and untreated alloys. The procedure for sample preparation for characterisation and mechanical testing is also described in this Chapter.

4.2 Experimental setup for mechanical test methods

4.2.1 Experimental setup for rotating bending fatigue testing

Cantilever fatigue testing was performed using an SM1090 rotating-beam fatigue machine that was purchased from TecQuipment and shown in Figure 4.1. As displayed in Figure 4.2, the load is applied on the free end of the sample and the top part experiences tension and the bottom part compression. A ball bearing allows the sample to rotate freely while under load. Both tension and compression alternate throughout the cross-section under cyclic loading. A schematic representation of the cantilever fatigue loading is shown in Figure 4.3.

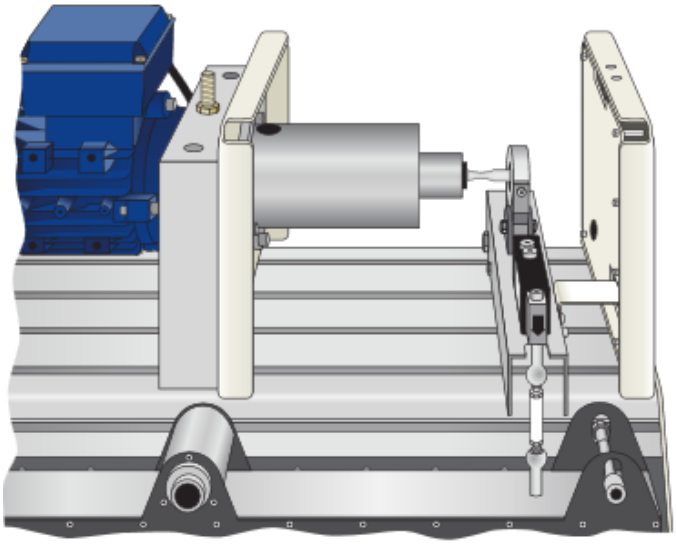

Figure 4.1. SM1090 rotating bending fatigue test machine [93].

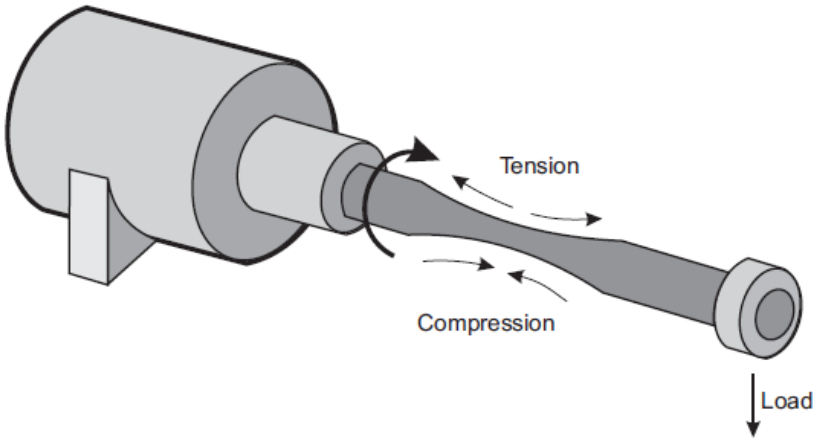

Figure 4.2. Rotating-bending cantilever beam [93].

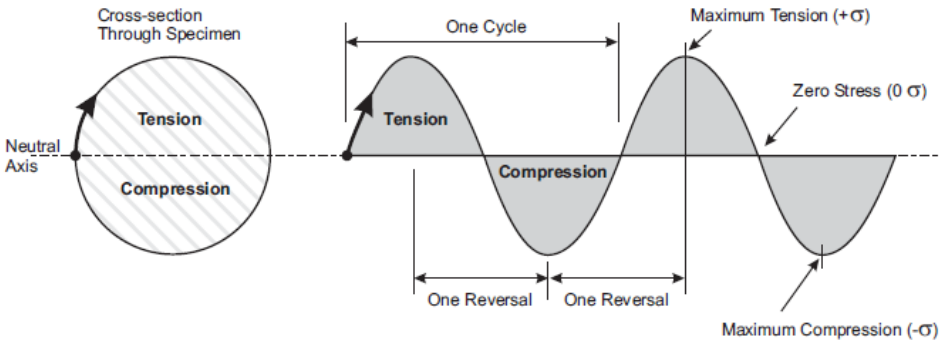

Figure 4.3. Schematic detailing the tension and compression loading cycle [93].

The test instructions were followed from the SM1090 rotating fatigue machine user manual to reduce test error [93]. At the start of each new test, lubrication (Ambergrase EXL) was applied to minimize the friction inside the bearing to increase the lifetime of the bearing. The load was applied to the sample by applying a dead weight prior to starting each test. The maximum load that can be applied to the fatigue machine was 80 N at a frequency of 63 Hz. The stress, σ, is a function of the distance to the load, l, shown in Figure 4.4, the load, F and the minimum neck diameter, D. Stress can be calculated using Equation 4.1:

$$\sigma = \frac{lF\ X\ 32}{\pi D^3} \qquad \text{Equation 4.1}$$

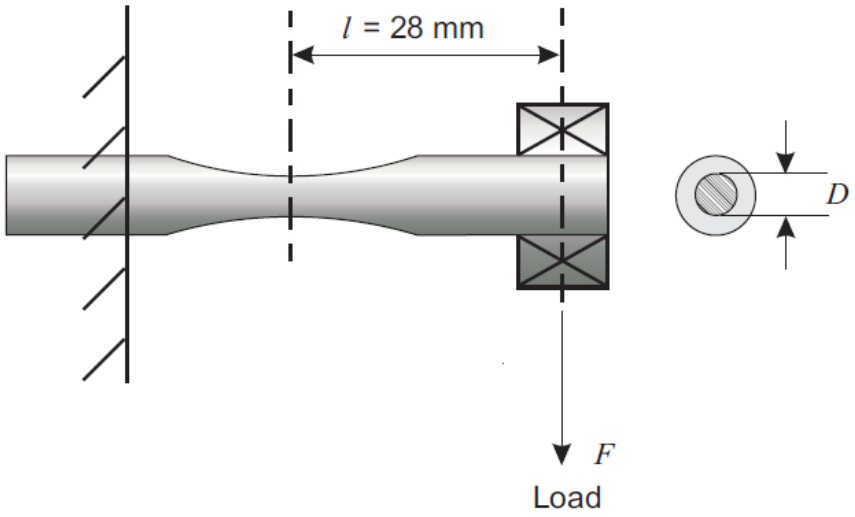

Figure 4.4. Distance to the load for fatigue specimen.

For the fatigue test, the frequency of the fatigue loading was set to f=60 Hz, as recommended by TechQuipment Ltd [93]. The samples were tested in a fully reversed fatigue loading with a stress ratio of R=-1. Samples were tested in the untreated and alternating magnetic field treated conditions. The treated samples were exposed to 30 mins of AMF treatment prior to the fatigue test. The effect of AMF on the fatigue life of aluminium alloy 2014-T6 and EN8 steel was investigated by comparing the fatigue life of untreated and treated samples. The applied stress ranged from 300 MPa to 525 MPa for EN8 steel and from 150 MPa to 280 MPa for the AA2014-T6 alloy. A total of 50 samples per alloy were used for fatigue testing. Tensile tests

were performed using a Tinius Olsen 25ST test machine at room temperature at a speed of 1 mm/s. Three treated and three untreated hourglass-shaped specimens for EN8 steel and AA2014-T6 were tensile tested.

4.2.2 Experimental setup for pin-on-disc testing

There are many methods that can be used to determine the tribological properties of materials such as pin-on-disc, four-ball, pin-on-cylinder, block-on-disc, thrust washers and crossed cylinder. For the purpose of this research, Pin-on-disc tests were conducted to test the slding contact wear properties. This test method was used as a mechanical test method for comparison of the untreated condition to the treated condition. The pin-on-disc tester calculates the friction and sliding wear properties of dry or lubricated surfaces of a variety of bulk materials and coatings. The pin-on-disc tester consists of a rotating disc of the material to be tested with a stationary sphere, usually made of cemented carbide, referred to as the pin which makes contact with the sample tested. Before starting, the normal load, rotational speed, and the wear track diameter are all set depending on the test conditions. The pin-on-disc tester records the coefficient of friction and the frictional force during the test. For the purpose of this research pin-on-disc tester will be used to test the sliding wear properties of untreated and treated EN8 steel, NAB and AA024-T6 in the lubricated condition.

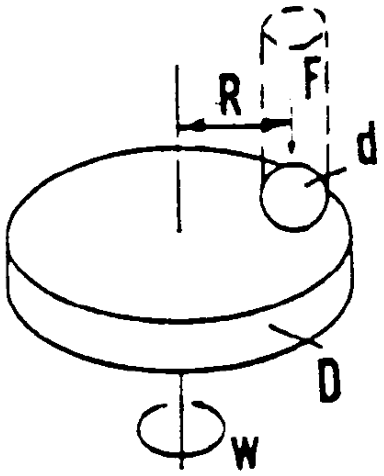

Figure 4.5. Pin-on-disc schematic diagram – F is the normal force on the pin, d is the ball diameter, D is the diameter of the test sample, R is the wear track radius and w is the rotation velocity of the disc.

Figure 4.5 shows a schematic representation of the basic principles for the pin-on-disc test, where F is the normal force on the pin, d is the ball diameter, D is the diameter of the sample, R is the wear track radius and w is the rotation velocity of the disc. In this study, a spherically-shaped ball was used as the pin. The coefficient of friction is the ratio of the frictional force to the loading force on the pin and is widely used to measure the lubricating properties of the lubricant and wear resistance of materials. Wear and friction results can be obtained by using a pin-on-disc tester. The measurement of the wear scar track width can reflect the anti-wear ability of a material [51].

The tribological properties of EN8 steel, NAB and AA 2014-T6 were evaluated using a POD 2 Pin-on-disc tester (Teer Coatings Ltd.) shown in Figure 4.6. The POD 2 Pin-on-disc tester has a friction force measurement sensitivity of 0.02 N. The alloys were tested using sunflower oil as a lubricant at sliding speed of 50 mm/s for a test period of 60 minutes. Sunflower oil used used as a lubricant; vegetable oils have been used in many tribological studies as lubricants because they are sustainable and friendly to the environment, while recent studies have demonstrated superior performance over conventional oils. The experimental conditions were conducted at an ambient temperature of 22°C and humidity of 45%. The contact ball bearings used in the tests had a diameter of 5 mm and were made of AISI52100 chrome steel with a Rockwell hardness of 60–67 and surface roughness R_a of 20 nm. A vertical load of 6N for AA2014-T6, 10N for EN8 steel and 10N for NAB was applied during pin-on-disc testing.

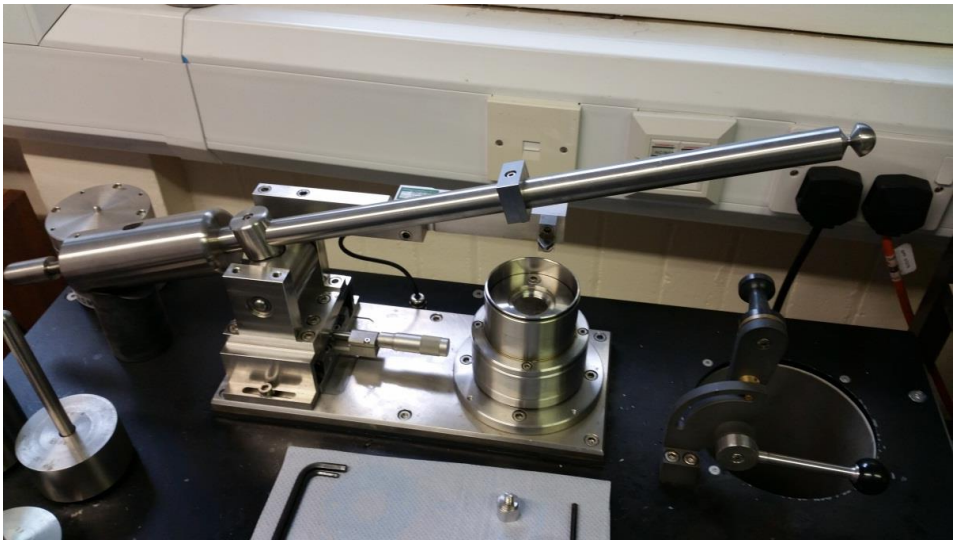

Figure 4.6. Pin-on-disc test equipment.

The test parameters are set in accordance with the ASTM 99-95a Pin-on-disc standard [94]. The specimen (25 – 27 mm diameter and 3 mm thickness) is placed on a rotating platform in the pin-on-disc machine. A 5 mm diameter ball is rigidly held perpendicular to the flat circular disc. The diameters tested for the pin-on-disc experiment are 12 mm for both untreated and alternating magnetic field treated samples. The results were used to determine the coefficient of friction, specific wear rate and the wear track width for the treated and untreated specimens.

The specific wear rate was calculated for the treated and untreated pin-on-disc samples. Prior to the test, each sample was cleaned thoroughly with acetone. A precision digital scale with accuracy of ± 0.1 mg was used to weigh the samples before and after pin-on-disk testing. The specific wear rates of the materials were obtained by:

$$W = \frac{\Delta w}{L \rho F} \qquad \text{Equation 4.2}$$

where W is the specific wear rate in mm^3/Nm, Δw is the weight loss measured in grams, L is the sliding distance in m, ρ is the density of the worn material in g/ mm^3 and F is the applied load in N. Specific wear rates was one of the measurements used to compare the untreated condition to the treated condition.

4.2.3 Experimental setup for cavitation erosion testing

Cavitation erosion testing was conducted to determine the wear resistance of the four alloys in the treated and untreated conditions. For these tests, a Vibra Sonic ultrasonic horn was used to produce cavitation damage at the face of the specimen while immersed in deionized water. Deionized water was chosen as the medium in accordence with the ASTM G32-10 standard to test only the cavitation erosion resistence of each material in the treated and untreated condition [95]. Furthermore, NAB and 70/30 brass alloys are typically used in cavitation erosion enviroments. The test apparatus consisted of a dedicated ultrasonic device (Vibra Sonic) which worked at a maximum electrical peak power of 750 W and a frequency equal to 20 kHz ± 50 Hz, with a vibration amplitude of 50 µm. The equipment is essentially

composed of a power generator and a mechanical unit with an ultrasonic probe attached to it. The latter part of the probe is formed using a titanium waveguide (Ti-6Al-4V). The ultrasonic horn will induce the cyclic formation of very high and very low pressures [68]. This process induces the formation and collapse of cavities in the liquid causing erosion damage [68, 95].

The vibrating frequency of the horn was set to 20 kHz according to the ASTM G32-10 standard [95]. This cavitation erosion test used the indirect method with a sample secured to a fixture and the ultrasonic horn resonating above it. The tip of the horn was submerged in the deionised water at a depth of 8 mm and the distance between the horn tip and the sample was set at 0.5 mm according to the ASTM G32-10 standard [95]. At the start of each test a new titanium waveguide probe was used. A heat exchanger tank is used to ensure that the test is conducted at a constant temperature of 20 ± 1 °C. The specimen support rig has been manufactured at the University of Hertfordshire and the set up can be observed in Figure 4.7. The technical drawing of the test rig can be found in Appendix B. Specimens of 10 mm diameter and 5 mm thickness were ground using 600 grit SiC paper to prepare the samples for the test. The erosion experiment was tested for a total of 6 hours for EN8 steel and AA2014-T6. The tests for the NAB samples were conducted for 8 hours in total. The samples were weighed before the test and at hourly intervals to measure the material weight loss. Mass loss was measured using a precision balance up to an accuracy of 0.0001 g (Denver Instrument). The pH of the water and the temperature of the horn tip were recorded every hour. To preserve the lifetime of the ultrasonic horn, compressed air flow was run through the ultrasonic transducer to cool the equipment. To contain the noise of the ultrasonic horn, a wooden box lined with foam was used to acoustically dampen noise from this type of test.

Figure 4.7. Cavitation erosion test set-up.

4.3 Experimental setup for characterization techniques

4.3.1 Experimental setup for X-ray diffraction analysis

X-ray diffraction is a non-destructive technique which can be used for phase identification and assess the residual stresses (RS). XRD and RS analyses were conducted using a Bruker D8 Advance X-ray diffractometer, with Cu-$K_{\alpha 1}$ radiation of wavelength 0.1540549 nm and radiation energy of 8.05 keV. The tube voltage and amperage were set at 40 kV and 40 mA respectively. The monochromator slit was set at 0.6 mm sample size. The peaks evaluated for EN8 steel, AA 2014-T6, brass and NAB, were $2\Theta = 137.2°$ (H K L of (3 1 0)), $2\Theta = 116.6°$ (H K L of (4 2 2)), $2\Theta = 112.6°$ (H K L of (4 0 0)) and $2\Theta = 115°$ (H K L of (4 0 0)) respectively. The method used to calculate the residual stresses was the Sliding Gravity method (which is the preferred method for industrial products) [96]. To improve the accuracy of the background, subtraction, smoothing, $K\alpha_2$ correction, absorption correction and polarisation corrections were performed. The stress model used was based on normal stress. All the data were analysed using the Leptos software version 7.9. In measuring RS using XRD, the strain in the crystal lattice is calculated and the associated RS is determined from the elastic constants assuming a linear elastic distortion of the appropriate crystal lattice plane.

4.3.2 Experimental setup for microhardness test

A Struers DuraScan hardness tester was used to conduct microhardness measurements for samples before and after treatment. Measurements were taken along the radius of each specimen. For the pin-on-disc and cavitation erosion investigations, the hardness results were acquired using the same test samples. Hardness values were obtained by averaging at least 60 indentations across two radii of circular samples. Enough distance was maintained between two measurements in order to avoid plastic deformation from each indentation. Microhardness tests were conducted in the untreated and treated conditions for the same sample.

4.3.3 Experimental setup for Nanoindentation tests

Mechanical properties for the pin-on-disc samples before and after treatment were obtained using the NanoTest Vantage platform 3 from Micro Materials Ltd (Wrexham UK). This mechanical test method was used to compare the untreated and treated condtion of EN8 steel, AA2014-T6 and NAB. The NanoTest Vantage platform 3 uses a pendulum-based depth-sensing system with the sample mounted vertically. The load is applied using an electromagnet as shown in Figure 4.8. Current in the coil causes the pendulum to rotate on its frictionless pivot so that the indentor penetrates the surface. To determine the hardness, elastic recovery parameter and H^3/E^2 ratio, nanoindentation tests were preformed using a three-sided pyramidal Diamond Berkovich indenter.

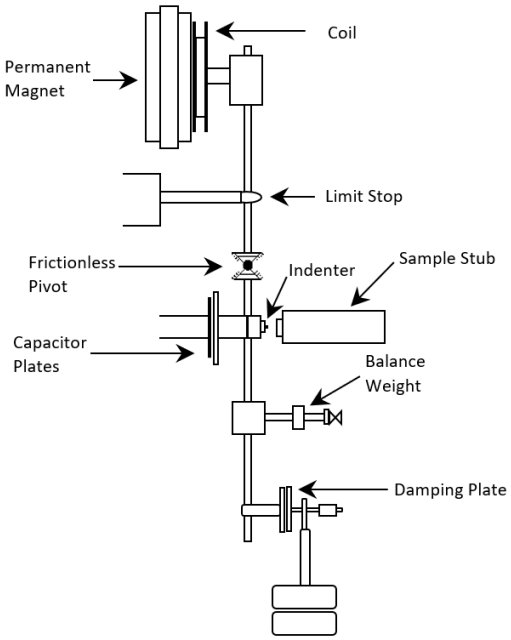

Figure 4.8. Schematic of the NanoTest Vantage platform 3.

A total of 100 indents were performed using a peak load of 50mN with a load hold time of 10 seconds, a dwell period of 20 seconds and unloading time 5 sec. The raw data were collected and processed automatically by the software using the Oliver-Pharr analysis [97]. The indentations were performed using a 10 by 10 grid matrix with 100µm spacing between each indentation. The Elastic Modulus of the sample can be calculated using the following equation:

$$E = \frac{1-{v_s}^2}{\frac{1}{E_r}-\frac{1-{v_i}^2}{E_i}} \qquad \text{Equation 4.3}$$

where E is the elastic modulus of the sample, v_s and v_i are the Poisson's ratio of the sample and the Berkovich indenter, E_i is the elastic modulus of the indenter and E_r is the reduced modulus of the sample after indentation. The Poisson's ratio values used for EN8 steel, NAB and AA2014-T6 were 0.3, 0.328 and 0.33 respectively [98]. All indentations were conducted inside an enviromental chamber set to a constant temperature of 23°C. Before testing, force calibration of the nano indenter was achieved by using precise calibration weights. The diamond area function and frame compliance of the nanoindenter was conducted by applying

various indentations at different loads on the two reference materials (tungsten and fused silica).

4.3.4 Experimental setup for electrical conductivity measurements

The electrical conductivity of an alloy can be an indirect measure of the density of distribution of dislocations and precipitates, as it is highly sensitive to the microstructure of the alloy [99]. An addition of any alloying element can lead to reduction in the electrical conductivity. The alloying of pure aluminium, strain hardening or precipitation hardening which are known to improve the mechanical properties can also reduce the electrical conductivity [100]. Salazar-Guapuriche et al. investigated the microhardness and conductivity in aluminium alloy 7010 during a natural ageing process. The increase in microhardness and the corresponding reduction of the electrical conductivity has been related to the formation of precipitates. It has been mentioned that the formation of GP zones and fine coherent and semi-coherent precipitates during natural ageing can decrease the electrical conductivity. However, the formation of precipitates can enhance the microhardness. This phenomenon is also supported by other research work [99]. Electrical conductivity along with microhardness have been correlated to the mechanical properties of aluminium alloy [99-102].

Electrical conductivity measurements were conducted to assess the effect of the alternating magnetic field treatment on the precipitation hardening of AA2014-T6. Electrical conductivity measurements were fulfilled in for all test samples by using the same sample in both the untreated and treated conditions. For the fatigue and cavitation erosion tests, a sample geometry of 10 mm diameter and 5 mm thickness was used. For the pin-on-disc tests the actual pin-on-disc sample for AA2014-T6 was used. These tests were conducted using a Foerster SIGMA TEST 2.069 conductivity meter at room temperature as shown in Figure 4.9. The accuracy of this equipment is rated at ± 0.5 % of the measured value at 60 kHz. During the test, samples were placed in the jig and a spring applied a constant force to make contact with the conductivity probe. The electrical conductivity was measured 15 times at the surface of tablet samples for both treated and untreated alloys. Measurements of electrical conductivity where taken in MS/m.

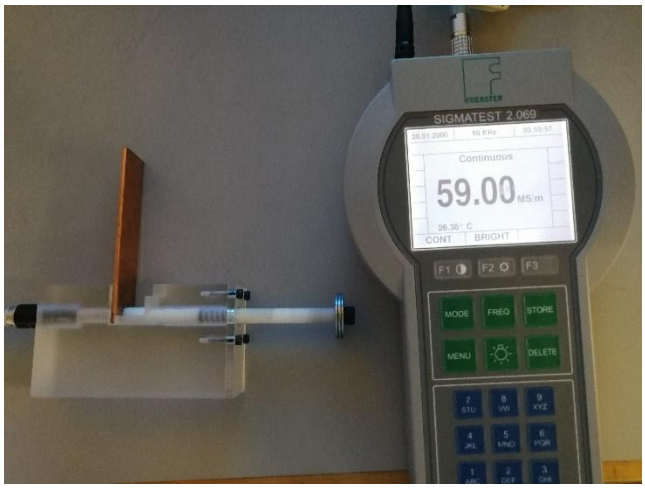

Figure 4.9. Electrical conductivity measurement set up.

4.3.5 Experimental setup for a surface roughness and surface profilometry

For the surface profilometry, a Mitutoyo Surftest SJ-500 2D surface profiler was employed to study the wear track scar profile and track surface roughness, Ra, for pin-on-disc samples. This measurment was used to compare the untreated and treated condition for wear track scar. The surface profile and the average surface roughness measurements were conducted on the wear tracks. A total of five measurements at different points of the wear track were obtained. The liner surface profile was measured by the equipment using a stylus profilometer with a styles tip radius and angle of 2µm and 60° respectively. The detector measuring force for the Mitutoyo Surftest SJ-500 2D surface is 0.75mN. To ensure sample stability, each measurement was conducted on a flat surface table.

4.3.6 Experimental setup for magnetic force microscopy

Magnetic force microscopy (MFM) was developed from atomic force microscopy (AFM) and is a key technique for characterizing magnetic properties within materials. The imaging principle is to detect the interaction between a magnetic probe and a magnetic field to generate a magnetic gradient distribution. When using the MFM, the contour following mode was used to scan the sample. This technique scans the sample surface twice (shown in Figure **4.10**a). The first scan in tapping mode records the surface morphology of the sample; in the

second pass, the z-scanner traces the previously acquired pass with the added z-offset. The magnetic probe is lifted to scan the surface of the sample.

The magnetic tip interacts with the magnetic field on the sample which results in deflection of the magnetic tip. The morphology of the magnetic domain is obtained by detecting a reflected laser beam and a position-sensitive photodiode. In this investigation, an Easyscan 2 AFM (shown in Figure **4.10**b) made by Nanosurf was used to observe changes in the magnetic domains within treated and untreated EN8 steel and NAB pin-on-disc samples. Using a Neodynium MagneticMulti74-G cantilever, the scanning range was 10 µm by 10 µm and the height of the probe for the measured surface was 60nm for NAB. For the EN8 steel sample a scanning range of 50 µm by 50 µm was used with a probe height of 100nm.

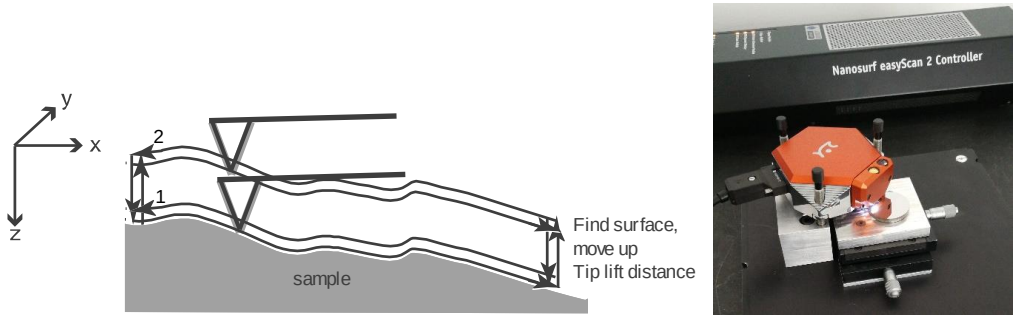

(a) (b)

Figure 4.10. (a) Illustration of contour following mode (b) Nanosurf Magnetic/Atomic Force Microscope.

4.4 Experimental setup for electron microscopy

SEM was employed using a JEOL JSM-5700 CarryScope scanning electron microscope operating at an accelerating voltage of 20kV. SEM was conducted to analyse the surface of samples from all three main areas of study, fatigue, cavitation erosion and wear. For the pin-on-disc testing, SEM was conducted to examine the wear tracks for treated and untreated NAB, EN8 steel and AA2014-T6 samples. Furthermore, the dimension of the wear scar tracks were measured and compared using the SEM. Finally, for the study investigating the effects of magnetic field treatment on the erosion resistance of metallic alloys, SEM was conducted to examine the surface morphology of untreated and treated alloys. SEM techniques such as electron backscattering and secondary electrons were used. The JEOL JSM-5700 CarryScope

is able to give a maximum resolution of around 5nm depending on the size of the electron beam. In this research, TEM was conducted to examine the microstructural changes of samples in the untreated and treated conditions. TEM was carried out using a JEOL JEM-1400F operating at 120 kV. The JEOL JEM-1400F TEM is able to give a maximum resolution of around 0.2nm.

4.5 Sample preparation procedures

4.5.1 Sample preparation for fatigue testing

Hourglass-shaped specimens for fatigue testing were machined from bars of 12.5 mm diameter using an XYZ Proto Trak SLX CNC lathe. The geometrical details of the hourglass-shaped for the EN8 steel and AA2014-T6 test samples are shown in Figure 4.11.

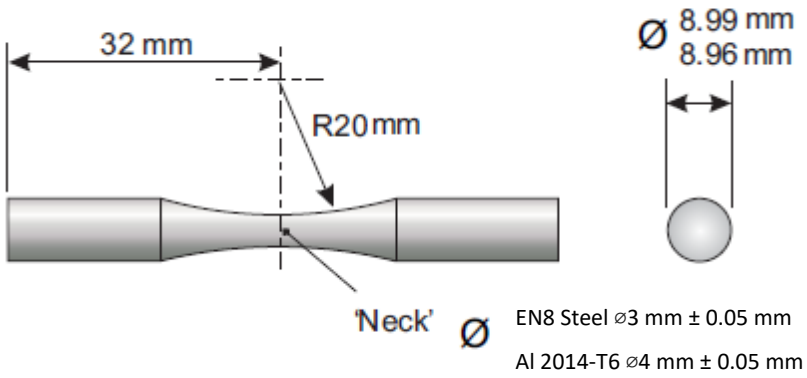

Figure 4.11. Sample geometry details for fatigue test samples.

The samples were designed using the CATIA V5 CAD software package. The neck area of the fatigue samples was polished by carrying out ten circular rotations using fine (3000) grit silicon carbide paper to reduce the surface roughness of the tested sample surface. These samples complied with the requirement of specification RF1020 given by the manufacturer and supplier of the rotating-bending fatigue machine SM1090 TechQuipment.

4.5.2 Sample preparation for pin-on-disc testing

NAB, EN8 steel and AA2014-T6 samples were prepared for pin-on-disc testing by sectioning NAB of 25.4 mm diameter bar, EN8 steel of 27 mm diameter bar and AA2014-T6 of 26 mm diameter bar to a thickness of 3.1 mm using a Struers Secotom-10 cut off machine under a very low feed rate of 0.03mm/s.

To prepare the samples for polishing, the specimens were mounted in black Bakelite resin using a Metaserv hot mounting press. Using the Struers Tegrapol polishing machine, the alloys were ground using 180, 340, 600 and 800 grit silicon carbide papers. The surface was then gradually polished using 9 μm, 3 μm and 0.3 μm diamond suspension to a surface roughness, R_a, of 15 nm. The test parameters were set in accordance with the ASTM 99-95a Pin-on-disc standard [94].

Prior to pin-on-disc testing, both the pin bearing ball and the discs were cleaned with isopropanol in an ultrasonic water bath for five minutes to remove any grease; further ultrasonic cleaning was carried out using acetone for five minutes. In this study, the same sample geometry and preparation were used to prepare samples for X-ray diffraction, microhardness, nanoindentation and electrical conductivity measurements.

4.5.3 Sample preparation for cavitation erosion testing

For the microhardness tests and the X-ray diffraction analysis, tablet-shaped sample (10mm diameter and 5mm height) specimens were prepared. For the polishing stage, the specimens were mounted in black Bakelite resin using a hot mount press. Using the Struers Tegrapol polishing machine, both alloys were ground and polished. The top surface was ground using 180, 340, 600 and 800 grit silicon carbide papers. The surface was then gradually polished using 9 μm, 3 μm and 0.05 μm diamond suspension.

4.5.4 Sample preparation for TEM

TEM preperation for AA2014-T6, NAB and the brass alloy were prepared using the electropolishing technique. For TEM preperation of EN8 steel , focused ion beam (FIB) milling

was carried out using a TESCAN LYRA3 equipped with a high-performance CANION FIB system for precise cross-section cutting. The EN8 steel foil sample was prepared from the flat side of the centre of the sample's surface.

Preparation of the AA2014-T6, NAB and 70/30 brass alloy TEM samples was carried out by cutting 500 μm from the sample bar using the Struers Secotom-10 cut off machine. The samples were then mounted on a manual specimen grinder using bees wax heated to 150°C to stick the sample in place. The samples were then manually ground using 400 grit silicon carbide paper to a flat surface. The wax was heated to 150°C and the other side of the sample was mounted. Both sides of each sample were pre-thinned to an initial thickness of around 150 - 100 μm. The specimen grinder was then heated up to 150°C to melt away the wax. The samples were then cleaned in an ultrasonic bath with acetone for 5 minutes. Once cleaned, 3 mm specimen discs were punched from the bulk specimens using a Fischione model 130 specimen punch.

To observe microstructures by TEM, samples need to be electron transparent. In the final stage of TEM sample preparation, the discs were electrolytically etched using a Fischione automatic twin-jet electropolisher shown in Figure 4.12. The Fischione Automatic Twin-Jet Electropolisher uses two jets to direct the electrolyte onto the specimen; this approach can simultaneously thin and polish both sides. This electrochemical reaction dissolves the metal ions uniformly at a controllable and reproducible rate. The typical thickness value for electron transparent metallic samples is 30 - 50 nm. The parameters used to electrolytically etch NAB, 70/30 brass and AA 2014-T6 are presented in Table 4.1. As soon as the TEM sample has become electron transparent an alarm goes off to alert the user. After this, the sample is placed in methanol to neutralize the acid and is dried using filter paper.

Figure 4.12. Fischione automatic twin-jet electropolisher with the low-temperature container.

Table 4.1. Etching solution and parameters used to etch nickel aluminium bronze and AA2014-t6.

Generic Material	Alloy	Solution	Conditions
Cu based alloys	Nickel-Aluminium Bronze	Nitric acid 30%, Methanol 70%	-30 °C, 30V
Cu based alloys	70/30 Brass	Nitric acid 30%, Methanol 70%	-30 °C, 30V
Al alloys	2000 series aluminium alloys	Nitric acid 10%, Methanol 90%	-10 °C, 10V

4.6 Chemical composition of samples

Cold rolled EN8 steel, NAB, 70/30 brass and extruded aluminium alloy 2014 in T6 temper were used in this investigation. The chemical compositions of these alloys are shown in Table 4.2. The materials were purchased from Thames Stockholders and were in the form of cylindrical rods. The EN8 steel, 70/30 brass and AA2014-T6 were purchased as rods with diameter of 12.7 mm. Rods of EN8 steel of 27 mm diameter, AA2014-T6 of 26 mm diameter and NAB of 25.4 mm diameter were also purchased from the same supplier and used for pin-on-disc testing.

Table 4.2. Nominal compositions range of metals used in the research

Metal	Composition, wt.%															
	Al	C	Cr	Cu	Fe	Mg	Mn	Mo	Ni	P	Pb	S	Si	Ti	Zn	Others
EN8 Steel*	-	0.36 - 0.44	-	-	Bal.	-	0.6 - 1.0	0.15	-	0.05		0.05	0.1 - 0.4	-	-	-
NAB**	8.5 - 10	-	-	Bal.	4.0 - 5.0	-	0.5	-	4.0 - 5.0	-	- 0.05	-	0.1	-	0.4	0.5
Brass*	-	-	-	Bal.	0.05	-	-	-	-	-	0.07	-	-	-	28.5 - 31.5	0.15
AA2014-T6*	Bal.	-	0.1	3.9 - 5.0	0.7	0.2 - 0.8	0.4 - 1.2	-	-	-	-	-	0.5- 1.2	0.15	0.25	0.15

*[98], **[103]

5 Fatigue Studies

5.1 Introduction

Magnetic field treatment has previously been shown to enhance the fatigue life of metallic alloys [16, 104, 105]. While the research work in this area is still growing, the mechanisms of the effect of the treatment are still not fully understood. The literature review in Chapter 2 has summarised previous work on the effect of electromagnetic field treatment on the fatigue life and classical fatigue theory. The proposed mechanisms that have led to improvement in fatigue life include the rearrangement of the microstructure of the materials due to the treatment [16, 76], crack healing [106, 107] and the generation of strengthening precipitates [108]. The issues and challenges related to the effectiveness of the electromagnetic treatment on the fatigue resistance have also been discussed by various researchers [3, 109, 110].

Several studies [111, 112] using conventional treatment like nitriding, carburizing and shot-peening have demonstrated the improvement of the long-term duration and reliability of machine parts under cyclic loading. However, only a limited number of studies have addressed the use of external magnetic and electric fields to improve the fatigue resistance of metallic alloys in spite of evidence that they may have a beneficial effect. For example, Fahmy et al. reported that the application of pulsed magnetic field treatment on low-carbon steel prolonged its fatigue life. Bao-Tong et al. applied an alternating magnetic field to medium-carbon steel specimens that had been subjected to fatigue loading and showed that the alternating magnetic field could repair the fatigue damage if the damage had not exceeded a critical value, but this value was not quantified. On the other hand, Bhat et al. who conducted fatigue tests for mild steel in the presence of a continuous magnetic field for the entire test showed that the fatigue life actually decreased when the magnetic field intensity exceeded a magnetic field of 180 mT.

Conrad et al. demonstrated that the fatigue life of copper increased following the application of a pulsed electric current; this observation was attributed to induced slip homogenization that promoted dislocation mobility in the material as a result of the application of the pulsed current. Furthermore, Roh et al. showed that electropulsing increased the ductility of aluminium alloys. Some investigations [4, 15, 24, 33] have demonstrated the ability of

electropulsing to extend fatigue life by means of crack healing. For example, Hosoi et al. achieved crack healing of stainless steel, while Zhou et al. [106] showed that pre-cracks within medium-carbon steel could be healed, but the mechanisms of crack healing have not been fully understood.

Researchers have shown that magnetic field treatment can influence mechanical properties such as micro-hardness, yield strength and induce changes in RS by changing the morphology of precipitates and the dislocation distribution within a material [113, 114]. Thus, the exposure of metallic components to a magnetic field may alter the lifetime of the component. However, there is not enough research to fully comprehend the relationship between fatigue resistance and exposure to a magnetic field, while the mechanisms governing the treatment are not entirely understood. In the light of this, the main objective of the investigation of this part of the study was to examine the effect of alternating magnetic field treatment on the fatigue life of EN8 steel and aluminium 2014-T6 alloys. While a large body of research has addressed the effects of electropulsing and pulsed magnetic field treatment, the number of investigations involving alternating magnetic field treatment is rather limited. In addition, the treatment developed at the University of Hertfordshire is cost-effective and easy to perform. EN8 steel is of interest because it is a standard load-bearing steel, while AA2014-alloy is widely used in aerospace applications.

5.2 Methodology

Chapter 4 section 4.6.1 (Sample preparation for fatigue testing) describes the methodology of the preparation of the samples for fatigue testing. The nominal compositions for EN8 steel and AA2014-T6 are presented in Table 4.1 and Table 4.2 in Chapter 4.

5.2.1 Experimental setup for alternating magnetic field treatment

Alternating magnetic field treatment was conducted by placing the specimens in a magnetizer. Figure 3.5c displays the magnetic field directions for different-shaped samples. The treatment duration was 30 minutes. The registration of the magnetic field without a specimen in the magnetizer is presented in Figure 3.6c. The magnetic field was measured using a Hirst GM08

Gaussmeter and the registration conducted using a Picoscope 4224 digital oscilloscope. The temperature of the sample during the treatment was measured using a K-type thermocouple that was in direct contact with the sample. A temperature increase of 12^{o}C and 14^{o}C for the EN8 and AA2014-T6 samples was recorded respectively.

5.2.2 Characterization Methods

In this Chapter, fatigue testing was conducted using a SM1090 rotating-beam fatigue machine from TecQuipment. Specimens were treated and tested under different conditions to failure. The fracture surfaces were examined in order to analyse the fracture mechanism by using scanning electron microscopy (SEM). In addition, residual stress measurements were conducted by means of X-ray diffraction. Changes in microstructure were further studied using transmission electron microscopy (TEM). Mechanical testing such as Vickers microhardness, tensile testing and residual stress measurements were also conducted in order to understand the effects of the treatment.

5.3 Results

5.3.1 Effect of alternating magnetic field treatment on fatigue life of metallic alloy

Figure 5.1a and Figure 5.1b shows the fatigue life S-N curve for EN8 steel and AA2014. The results show at the low cycle fatigue range for both EN8 steel and AA2014-T6 treated and untreated, there was no change in the fatigue behaviour. However, at the high cycle fatigue range, the results clearly indicate that after treatment there is an increase in fatigue endurance for both metals. For example, at a fully reversed stress level of 350 MPa for EN8 steel and 190 MPa for AA2014-T6, the fatigue life has increased by more than 3 times.

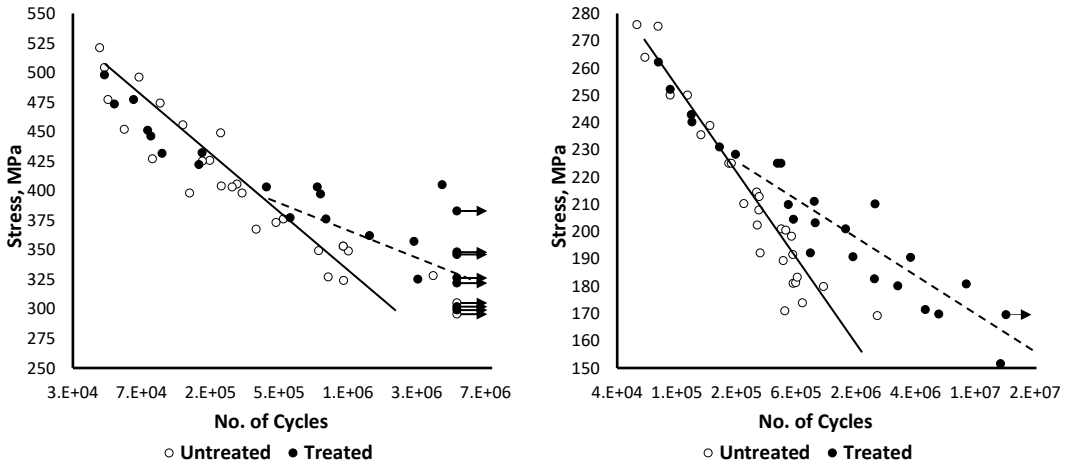

(a) (b)

Figure 5.1. S-N curves for untreated and treated (a) EN8 Steel and (b) AA2014-T6; data for samples where the test was stopped without sample fracture are marked as •→.

5.3.2 Effect of alternating magnetic field treatment on mechanical properties of EN8 Steel and AA2014-T6

The results of microhardness, tensile strength, electrical conductivity and RS are summarised in Table 5.1. The RS results show that after treatment there is an increase in compressive stresses by 19% and 30% for EN8 steel and 2014-T6 respectively. Table 5.1 also shows that there is a slight increase in microhardness after treatment. Another important observation is that there is a reduction in the mean-square deviation (MSD) in the microhardness values following treatment effectively meaning that there is a decrease in the scatter of the microhardness data for both treated alloys. This suggests that the properties of the samples had also become more uniform as a result of the treatment. Additionally, the electrical conductivity measurements for AA2014-T6 exhibited a decrease of 2.28% after treatment.

Table 5.1. Mean (M) and Mean-square deviation (MSD) Results of Microhardness, Tensile Strength, Electrical Conductivity and RS.

Sample Condition		Microhardness[1], HV		Electrical Conductivity[2], MS/m		Residual Stress[3], MPa		UTS[4], MPa	
		M	MSD	M	MSD	M	MSD	M	MSD
EN8 Steel	Untreated	264	12.3	N.A.		-268	71.7	886	18.1
	Treated	270	7.6			-320	39	914	15.5
AA2014-T6	Untreated	153	4.4	22.90	0.0074	-99	40.5	541	2.5
	Treated	158	2.8	22.38	0.0046	-130	20.9	550	3.6

[1]average of 60 indentations per sample (3 samples); [2]average of 20 measurements per sample (3 samples); [3,4]average of 3 samples

5.3.3 Effect of alternating magnetic field treatment on fatigue fracture characteristics

The results showed that following the treatment, the fatigue life of EN8 steel at a stress level of 350 MPa increased from 791,990 to 5,364,498 cycles. For the AA2014-T6 alloy, the fatigue life at a stress level of 190 MPa increased from 512,979 to 3,619,824 cycles. Both the EN8 steel and AA2014-T6 treated samples exhibited a mixture of dimple and cleavage fracture as observed by using SEM, the results of which are shown in Figure 5.2 and Figure 5.3 respectively. The untreated samples, show much more quasi-cleavage fracture [115] throughout the fractured surface. The treated sample contains more ductile dimple features of diverse sizes similar to those discussed by previous researchers who had investigated the fractography of steels and aluminium alloys [116, 117]. A few quasi-cleavage features are visible in both of the treated alloys that exhibit ductile torn edges [118] or peaks and valleys [119]. The fracture surface of the untreated EN8 steel has more secondary cracks similar to those observed by Zhang et al [120] compared to the treated condition. Small secondary cracks can also be observed in the untreated AA2014 alloy as displayed In Figure 5.3b.

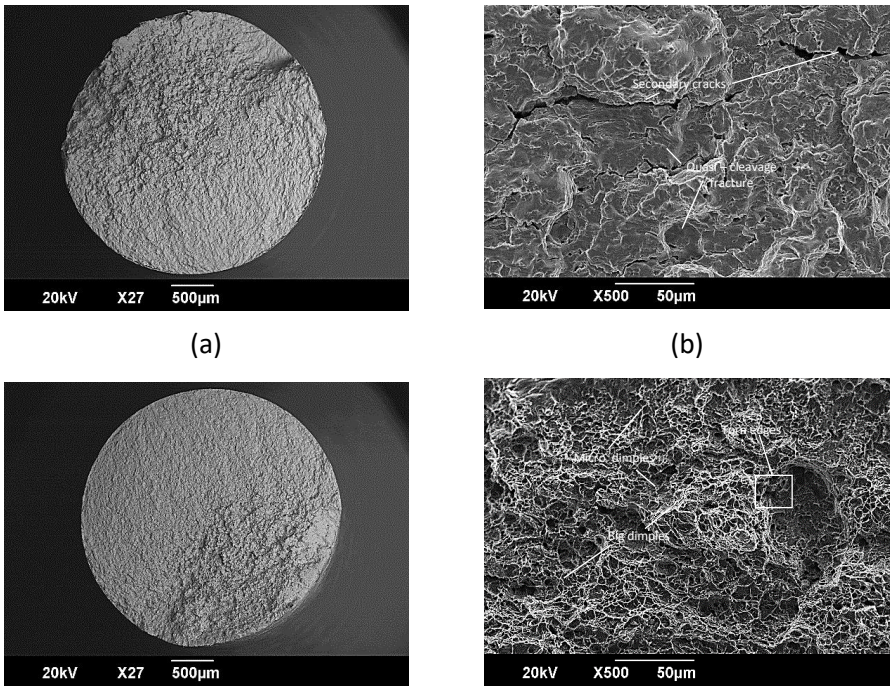

Figure 5.2. SEM images of EN8 Steel fractured surface for (a, b) untreated and (c, d) treated.

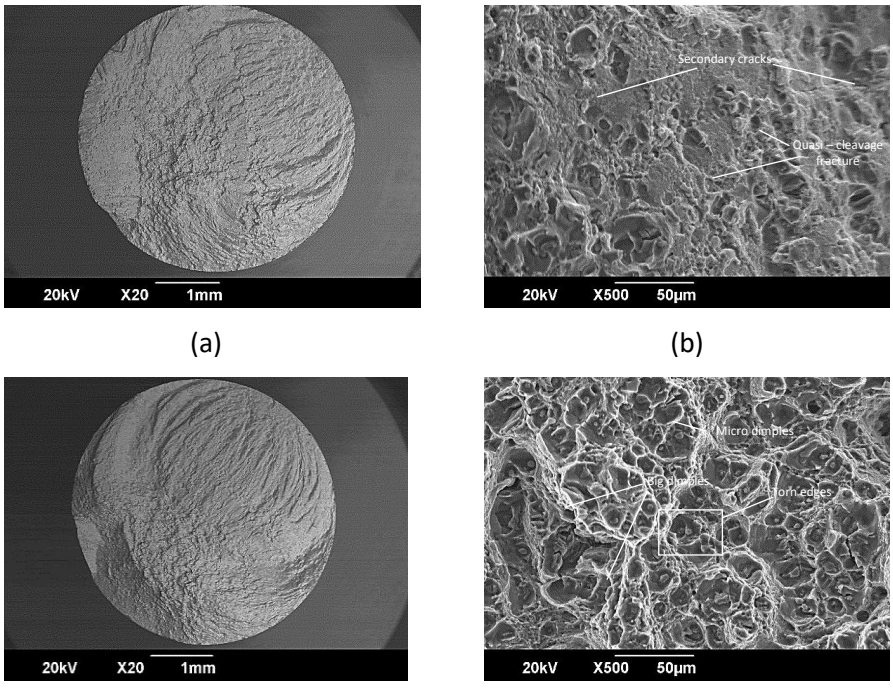

Figure 5.3. SEM images of AA2014-T6 fractured surface for (a, b) untreated and (c, d) treated.

5.3.4 TEM analysis of the effect of alternating magnetic field treatment on dislocations and precipitates

The results of TEM examination for the untreated EN8 steel in Figure 5.4 show local areas of high-density of dislocation structures such as dislocation tangles and pile-ups. Following the alternating magnetic field treatment, there appeared to be less dislocation pile up at the grain boundaries as well as less entanglement of dislocations. There is evidence of mobility of dislocations as a result of the treatment.

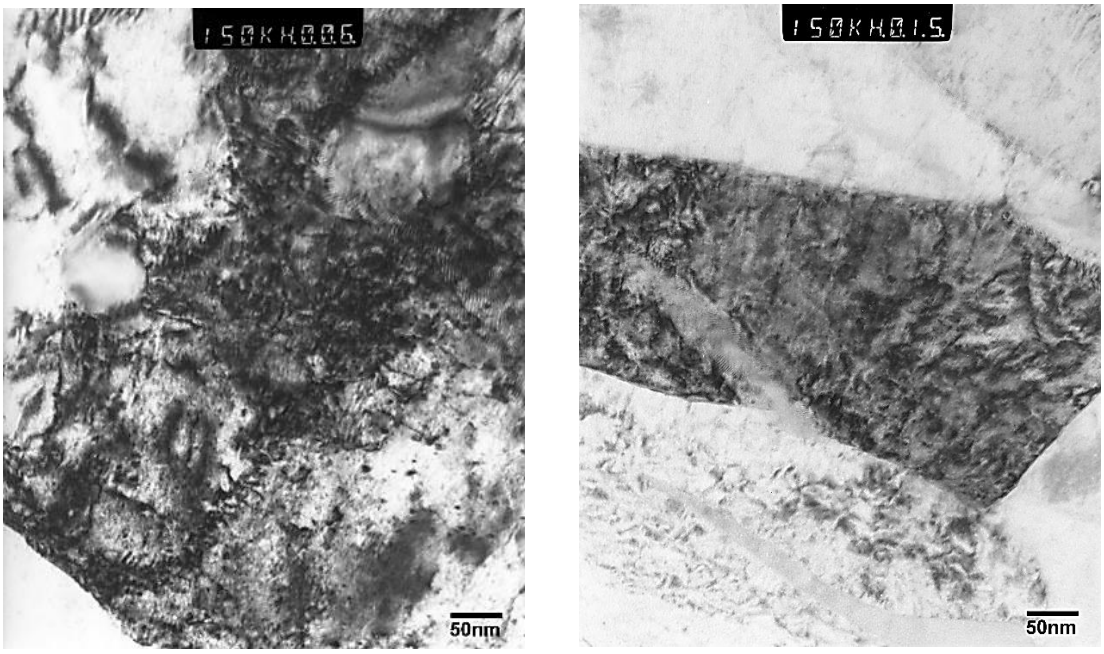

(a) (b)

Figure 5.4. TEM images of (a) untreated and (b) treated EN8 Steel.

TEM examination of aluminium 2014-T6 shows the presence of more precipitates for the treated sample compared to the untreated one (Figure 5.5a and Figure 5.5b). These precipitates are relatively uniformly distributed in the treated alloy. Taking into account their dimension and the decrease of the electrical conductivity of the alloy, it can be concluded that these are mainly GP zones and Θ'' precipitates.

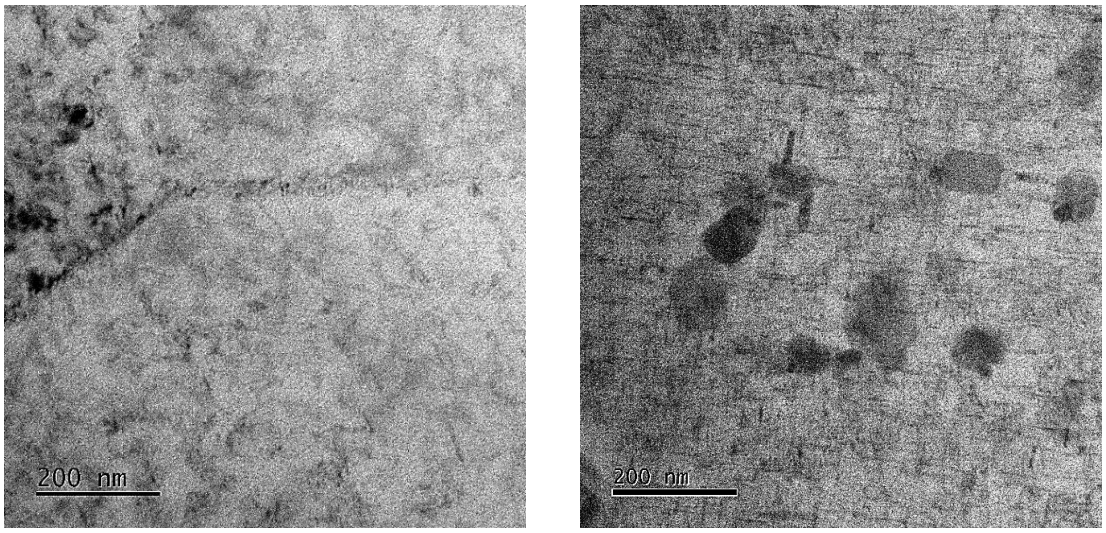

(a) (b)

Figure 5.5. TEM images of (a) untreated and (b) treated AA2014-T6.

6 Wear Studies

6.1 Introduction

Controlling friction and reducing wear using advanced technology are among the main means for prolonging service life and increasing the reliability of equipment [121-123]. There are two general approaches for reducing wear in mechanical systems; the separation of attrition faces of parts by the use of liquid or solid lubricants and the modification of materials and their properties including the application of coatings. The external parameters generally used in the traditional processing of materials are temperature, pressure and time. In recent years there has been increasing interest in processing materials by the application of external fields. A number of researchers have experimented with electrical and magnetic fields which have been shown to have an effect on the mechanical properties of materials. Chapter 2 has reviewed some of the research work that has been conducted on the application of electromagnetic field treatment to alter the wear resistance of metals. This includes information on the treatment parameters used by other authors and details of the effect on the microstructure of the materials and the wear behaviour. The problems and challenges related to the effectiveness of the electromagnetic treatment on the wear resistance were also discussed.

This Chapter reports on the effect of alternating magnetic field treatment on the frictional properties of EN8 steel, nickel-aluminium bronze and 2014-T6 aluminium alloy. The results of pin-on-disk experiments are presented; specifically the effect of the application of an alternating magnetic field on the wear tracks and the coefficient of friction for the three alloys has been considered. A small body of previous work has suggested that the application of a magnetic field can influence the wear resistance of metals, but the mechanisms governing the effect of the treatment are not fully understood. Most of the earlier investigations have addressed the effects of pulsed magnetic field treatment, while the number of studies involving alternating magnetic field treatment is rather limited. In consideration of this, the main objective of this part of the PhD project was to examine the effect of alternating magnetic field treatment on the frictional properties EN8 steel, NAB and AA2014-T6 alloys. EN8 steel is standard load-bearing steel, used in applications such as automotive components, axles, shafts etc. NAB is typically used for bushings and bearings, while AA2014-alloy is widely

used in aerospace applications. Specimens were treated and tested using pin-on-disc testing. The wear scar tracks were examined using scanning electron microscopy (SEM). In addition, residual stress measurements were conducted by means of X-ray diffraction for samples initially in the untreated state and subsequently in the treated condition. Studies of the magnetic domain structure of EN8 steel and NAB were conducted before and after treatment. Changes in microstructure were further studied using transmission electron microscopy (TEM).

6.2 Methodology

Chapter 4 section 4.6.1 (Sample preparation for fatigue testing) discribes the methodology of the preperation of the Pin-on-disc sample. The nominal compositions for EN8 steel, AA2014-T6 and NAB are presented in Table 4.1 to Table 4.3, respectively in Chapter 4.

6.2.1 Experimental setup for alternating magnetic field treatment

Alternating magnetic field treatment was conducted by placing the specimens in a magnetizer. Figure **3**.**5**a displays the magnetic field directions that were used for the pin-on-disc samples. The treatment duration was 30 minutes. The registration of the magnetic field without a specimen in the magnetizer is presented in Figure 3.6a. The magnetic field was measured using a Hirst GM08 Gaussmeter and the registration was conducted using a Picoscope 4224 digital oscilloscope.

6.2.2 Characterization Methods

Microhardness testing was conducted before and after treatment for EN8 steel, NAB and AA 2014-T6 using a Struers DuraScan microhardness tester with a load of 1N. The microhardness values were obtained by averaging the results of at least 60 indentations across two radii of the circular sample. Nanoindentation tests were conducted using the Micro Material NanoTest Vantage platform 3 equipped with a Diamond Berkovich indenter. A total of 100 indents were performed using a load of 50mN with a load hold time of 10 seconds, a dwell period of 20 seconds and unloading time 5 sec. The indents were performed using a 10 by 10

grid matrix with 100µm spacing between each indentation. Nanoindentation tests were conducted before and after treatment on the same sample. The hardness, elastic recovery parameter and H^3/E^2 ratio were calculated from the results.

Microhardness testing was conducted as a means to determine if there was a change in the mechanical properties of the metallic alloys after treatment. X-ray diffraction (using a Bruker D8 Advance) was performed to identify any phase changes in samples and to evaluate the RS before and after treatment of the same sample. The peaks that were used for RS analysis for EN8 steel, NAB and AA 2014-T6 were $2\Theta = 137°$, $2\Theta = 115.1°$ and $2\Theta = 116.6°$ respectively. For RS measurement, the Sliding Gravity method (which is the preferred method for industrial products) [96] was used. For the RS measurements, X-ray diffraction for samples was initially carried out in the untreated state; the same samples subsequently underwent alternating magnetic field treatment before X-ray diffraction for further RS measurement.

Electrical conductivity tests were conducted for the AA2014-T6 alloy in both the treated and untreated conditions. These tests were conducted using a Foerster SIGMA TEST 2.069 electrical conductivity meter at room temperature. Over 15 measurements were conducted per condition and an average value was then taken. Microstructural studies were carried out using SEM and TEM. For SEM examination, a JEOL JCM-5700 CarryScope was used to examine the worn surface of treated and untreated samples. A JEOL JEM-1400F was used for TEM to investigate the microstructure near the surface of the treated and untreated samples. The JEOL JEM-1400F was operated at 120 kV and was used for observations of changes for the NAB and AA2014-T6 alloys. For the EN8 steel, a FEI/Philips CM-20 TEM opperating at 200kV was used. MFM was conducted using a Nanosurf Easyscan 2 to observe changes in the magnetic domain structure of the untreated and treated EN8 steel and NAB specimens. A Neodynium magnet MagneticMulti74-G cantilever was used to scan the magnetic domain structure of the two alloys. Futher analysis of the morphology of the wear scar tracks was conducted using a 2D Mitutoyo Surftest SJ-500 2D surface profiler to characterize the wear scar track profile and the average surface roughness of the wear tracks.

6.3 Results

6.3.1 Effect of alternating magnetic field treatment on friction characteristics

Figure 6.1a to Figure 6.1c show the variation of the coefficient of friction with time as obtained from the pin-on-disk tests for untreated and treated EN8 steel, nickel-aluminium bronze and aluminium alloy 2014-t6, respectively. Figure 6.1d shows the specific wear rate of the treated and untreated EN8 steel, NAB and AA2014-T6 alloys. As seen in Figure 6.1a the coefficient of friction for the treated EN8 steel sample was lower than that for the untreated sample. After treatment, the average coefficient of friction was reduced by 18%. It is evident that after about 1 min into the test, the value of the coefficient of friction for the untreated sample started to initially increase slowly and subsequently (after about 7 min) to further increase at a much faster rate. After about 10 min, the value had risen to about 0.92 and kept increasing gradually to above 1. On the other hand, the value of the coefficient of friction for the treated sample remained almost constant at around 0.6 for about 25 min and began to gradually increase thereafter. Figure 6.1b shows that the treated NAB sample retained a lower coefficient of friction for a longer period of time than the untreated sample did (about twice as much). During the run-in stage, the coefficient of friction for the treated sample was 0.37 compared to a value of 0.44 for the untreated NAB (a 16% decrease). Figure 6.1c shows that in the case of AA2014-T6 the treated sample retained almost a constant coefficient of friction of about 0.13 for about 30 min, while the value for the untreated sample saw significant and progressive increase from the start of the test. Figure 6.1d shows the specific wear rate for the treated EN8 steel, NAB and AA2014-T6. The results show that as a result of the treatment there is a decreased of 41% for EN8 steel, 61% for NAB and 56% for AA2014-T6, respectively, compared to the untreated condition.

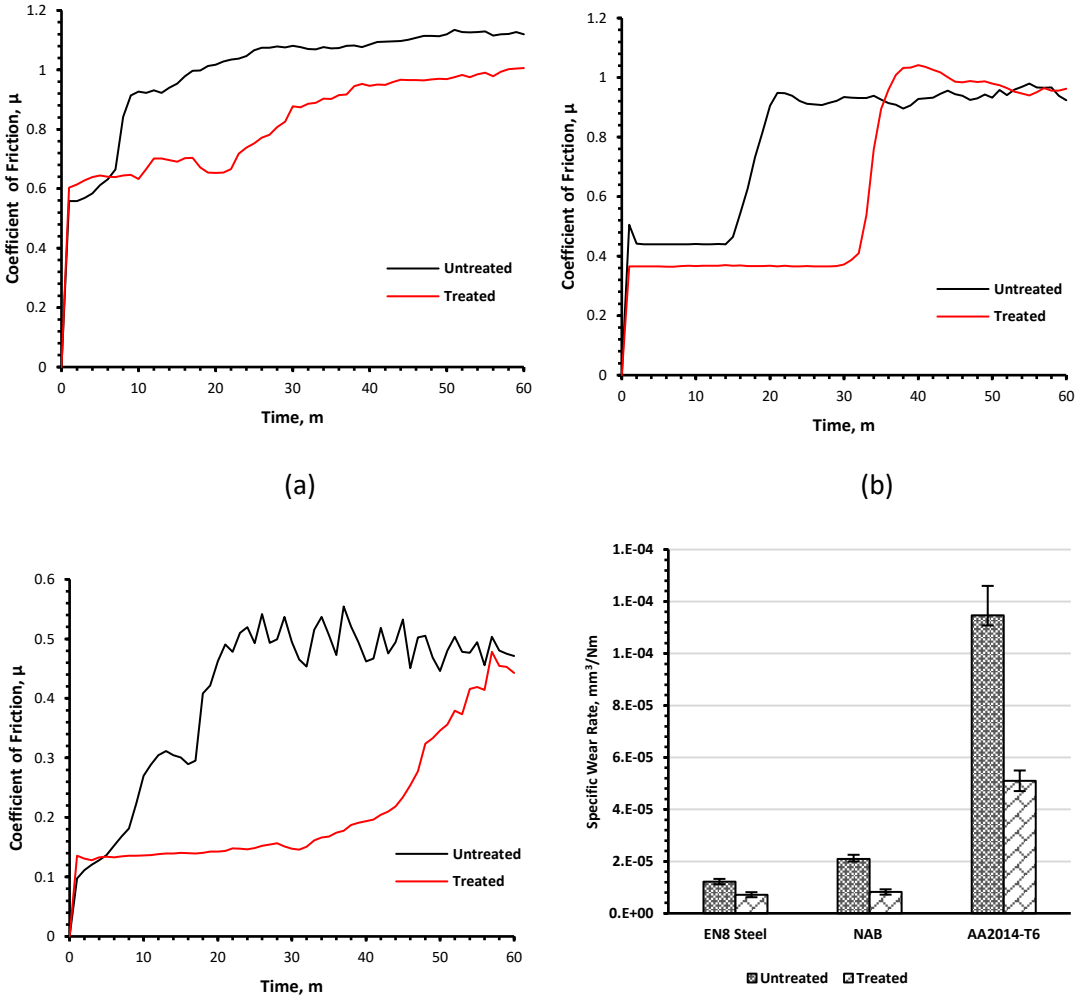

Figure 6.1. Variation of the coefficient of friction for untreated and treated (a) EN8 Steel, (b) NAB and (c) AA2014-T6 disc specimens and (d) specific wear rates for untreated and treated EN8 Steel, NAB and AA2014-T6.

The results of microhardness, average wear scar width, electrical conductivity and RS measurements for treated and untreated EN8 steel, NAB and AA 2014-T6 are summarised in Table 6.1. The RS results show that after treatment there is a significant increase in compressive residual stresses for EN8 steel, while the RS changed from tensile to compressive for AA2014-T6 alloy. In the case of NAB, the RS data show that following treatment, the NAB samples had experienced a drop in the tensile RS by approximately 40%. Another important observation is that after alternating magnetic field treatment there is a reduction in the wear scar width of 12%, 18% and 15% for EN8 steel, NAB and AA 2014-T6, respectively.

Furthermore, Table 6.1 also shows that there is a slight increase in hardness after treatment for all the alloys. Additionally, the electrical conductivity of AA2014-T6 after the treatment has decreased by about 0.9%. The average surface roughness of the wear tracks has decreased by 30% for EN8 steel, 20% for NAB and 44% for AA2014-T6.

Table 6.1. Mean (M) and Mean-square deviation (MSD) Results of microhardness, electrical conductivity, wear track width and Residual stress.

Sample Condition		Microhardness[1], H_V		Electrical Conductivity[2], MS/m		Residual Stress[3], MPa		Wear Scar Width[4], µm		Surface Roughness[5], R_a, µm	
		M	MSD	M	MSD	M	MSD	M	MSD	M	MSD
EN8 Steel	Untreated	268.8	± 12.4	N.A.		-290.7	± 20.2	316.7	± 5.1	0.532	± 0.121
	Treated	282.9	± 10.1			-346.2	± 25.7	283.2	± 5.5	0.373	± 0.031
NAB	Untreated	142.2	± 5.7	N.A.		39.6	± 116.7	272.5	± 8.8	0.201	± 0.019
	Treated	151.1	± 2.7			23.7	± 107.1	222.8	± 6.0	0.159	± 0.013
AA2014-T6	Untreated	221.8	± 19.7	22.99	± 0.039	59.0	± 36.9	517.5	± 7.0	0.580	± 0.026
	Treated	231.8	± 23.8	22.77	± 0.033	-12.0	± 23.3	439.7	± 10.5	0.326	± 0.008

[1]average of 60 indentations per sample (3 samples); [2]average of 20 measurements per sample (3 samples); [3]average of 3 samples; [4]average of 4 measurements 90 degrees per sample (3 samples); [5]average of 5 measurements per sample (3 samples)

6.3.2 Effect of alternating magnetic field treatment on the morphology of worn surfaces

Micrographs showing the wear scar width for the EN8 steel, NAB and AA2014-T6 pin-on-disc samples are presented in Figure 6.2, Figure 6.3 and Figure 6.4. The SEM micrographs for EN8 steel show the wear tracks for the untreated sample were deeper and slightly wider in comparison to those for the sample in the treated condition. From these observations, it is evident that the alternating magnetic treatment had resulted in an improvement of the wear resistance of EN8 steel. Observation from SEM reveals the wear mechanism for untreated and treated EN8 steel are both abrasive. However, in the untreated condition, there was more abrasive wear as deeper grooves and pitting can be observed. In the case of NAB and AA2014-T6, the untreated samples revealed several deep grooves as well as pitting on the surface. In contrast to the untreated samples, the grooves and pits that were observed for the treated NAB and AA2014-T6 samples were relatively shallow. In the case of untreated and treated NAB and AA2014-T6, the wear mechanisms appear to be abrasive, however, in the treated conditions, they appear to be less abrasive.

Support for SEM observation was conducted using a 2D surface profiler. Measurements of the wear track depth for the treated and untreated conditions and the results are presented in Figure 6.5, Figure 6.6 and Figure 6.7. For the EN8 steel sample (Figure 6.5), the wear tracks for the untreated sample were deeper and slightly wider in comparison to those for the sample in the treated condition. From these observations, it is evident that the alternating magnetic treatment had resulted in an improvement of the wear resistance of EN8 steel. In the case of NAB and AA2014-T6 (Figure 6.6 and Figure 6.7, respectively), the 2D surface profiler results indicate that the depth of the wear tracks produced for the untreated condition for both alloys was greater and wider than for the samples in the treated condition. In addition, bulging on both sides of the wear tracks was more prominent in the untreated case as opposed to the treated condition for AA2014-T6. Furthermore, the evidence in Fig. 4b shows more advanced stages of pull-out wear for AA2014-T6 in the untreated condition. Bulging was also apparent at the surface of the NAB untreated specimen, but in this case, the effect was slightly less compared to the AA2014-T6 sample.

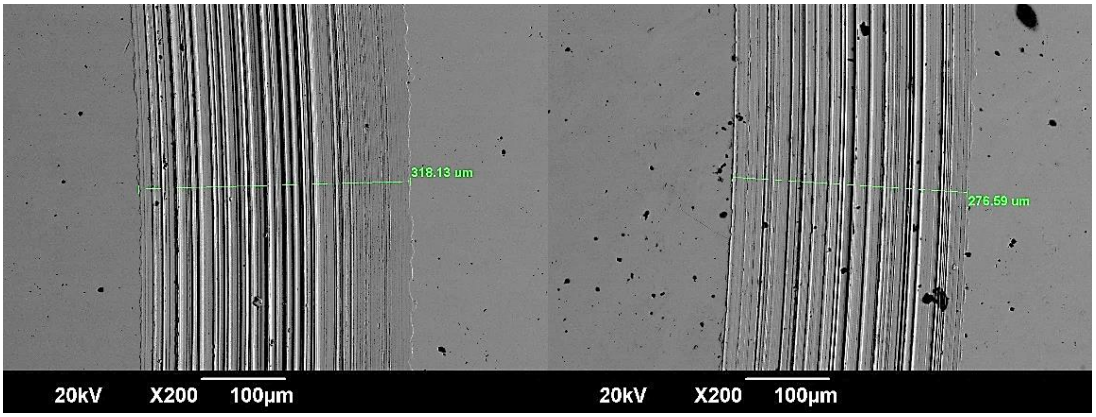

(a) (b)

Figure 6.2. SEM wear tracks of the surface of (a) untreated and (b) treated EN8 steel after 1 hour.

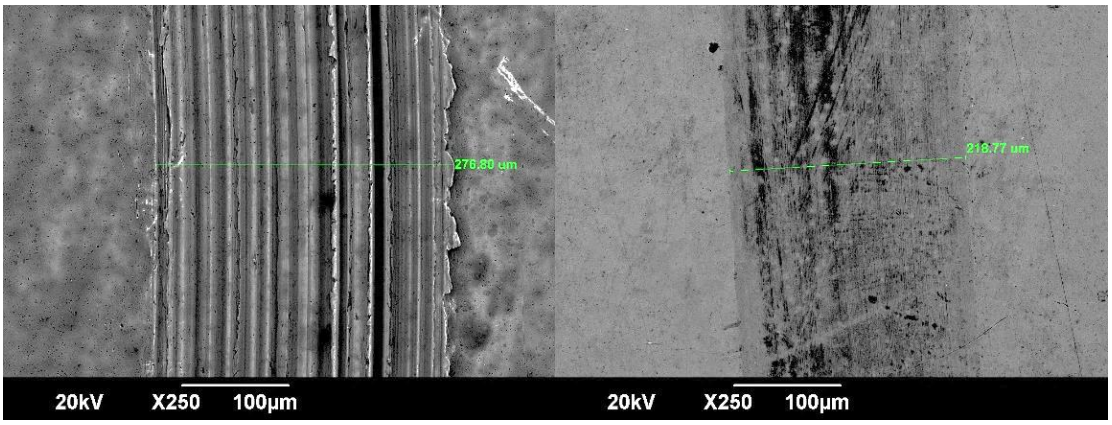

(a) (b)

Figure 6.3. SEM wear tracks of the surface of (a) untreated and (b) treated nickel-aluminium bronze after 1 hour.

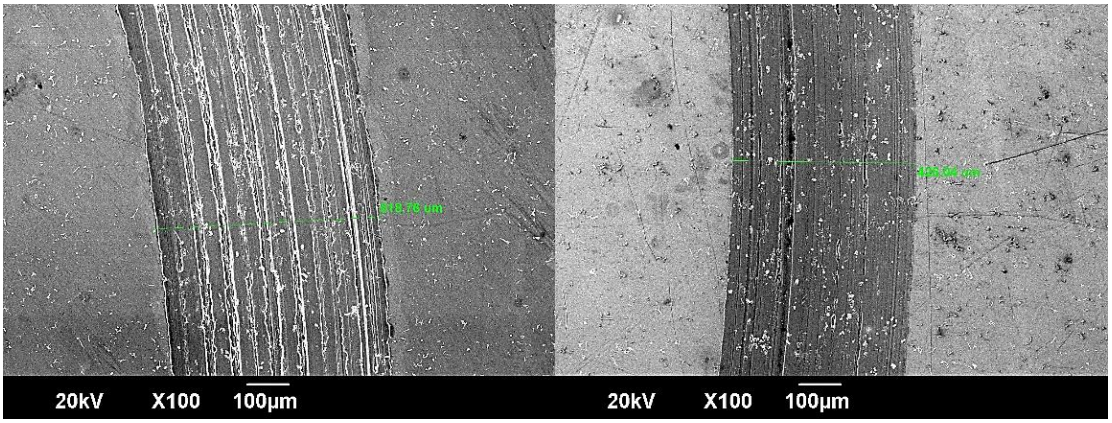

(a) (b)

Figure 6.4. SEM wear tracks of the surface of (a) untreated and (b) treated aluminium alloy 2014-T6 after 1 hour.

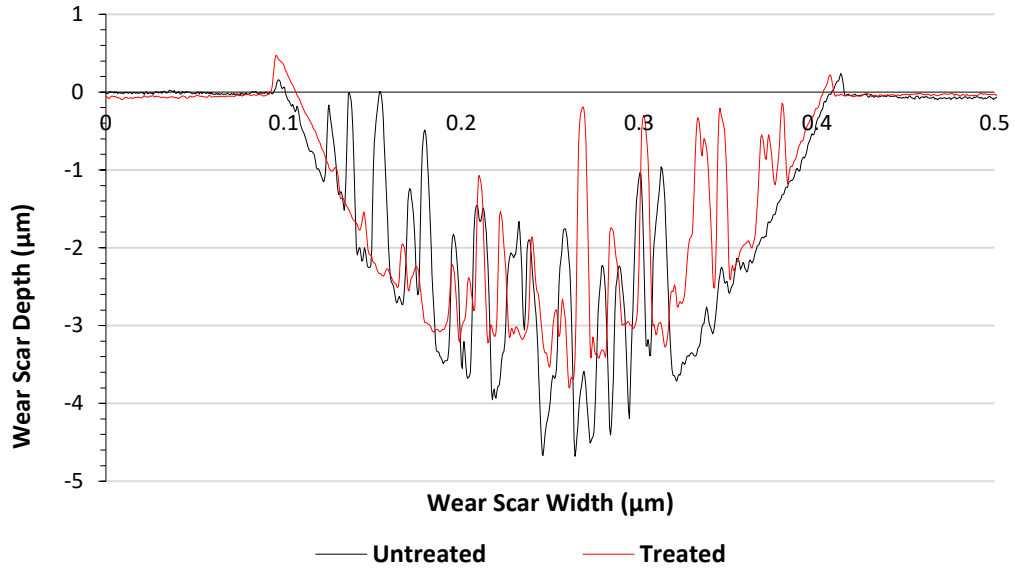

Figure 6.5. Comparison of 2D surface profile of Untreated (black) and treated (red) EN8 Steel.

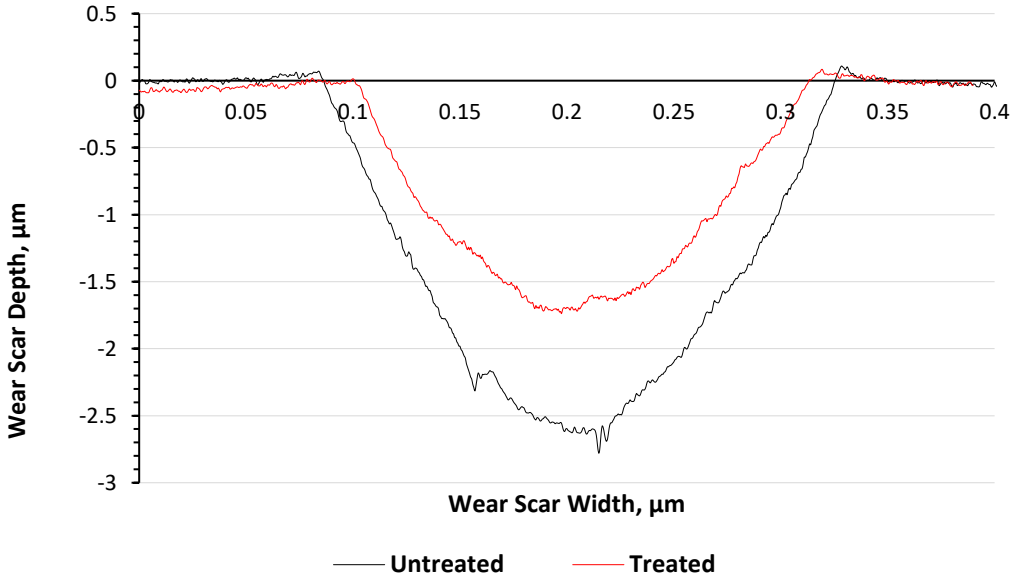

Figure 6.6. Comparison of 2D surface profile of Untreated (black) and treated (red) NAB.

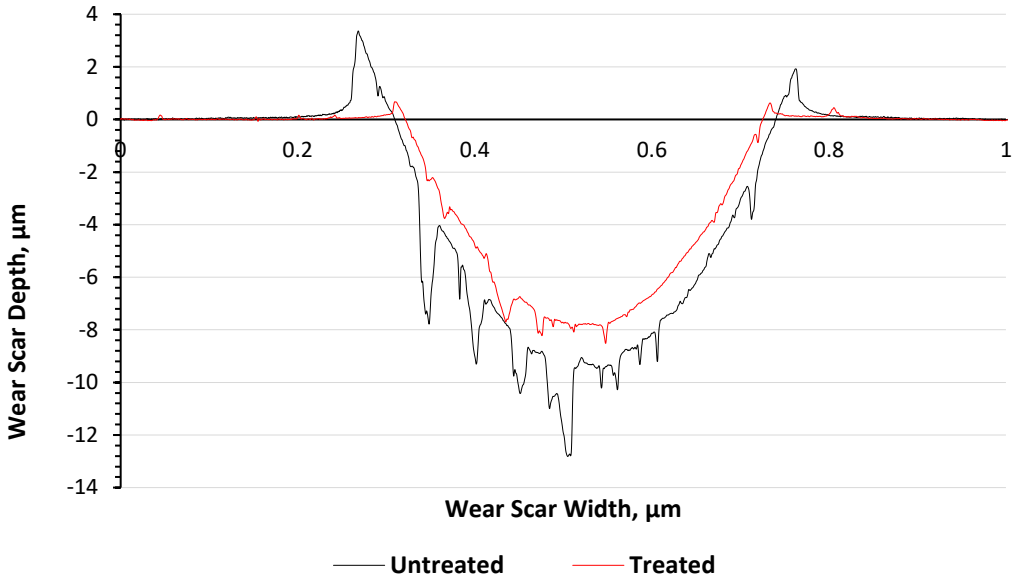

Figure 6.7. Comparison of 2D surface profile of Untreated (black) and treated (red) AA2014.

6.3.3 Effect of alternating magnetic field treatment on the nanomechancial properties of EN8 steel, NAB and AA2014-T6

Figure 6.5 to Figure 6.7 show a comparison of the 2D surface profiles of the wear tracks for untreated and treated EN8 steel (Figure 6.5), NAB (Figure 6.6) and AA2014-T6 (Figure 6.7). The results indicate that the depth of the wear tracks produced for all three alloys in the untreated condition was greater and wider compared to the samples in the treated condition. In addition, bulging on both sides of the wear tracks was more prominent in the untreated case as opposed to the treated condition for AA2014-T6. Furthermore, the evidence in Figure 6.7 shows more advanced stages of pull-out wear for AA2014-T6 in the untreated condition. Bulging was also apparent at the surface of the NAB untreated specimen, but in this case the effect was slightly less compared to the treated NAB sample.

Figure 6.8a – Figure 6.8c show a typical loading-unloading curve for magnetically treated and untreated EN8 steel, NAB and AA2014-T6 alloys. As shown in Figure 6.8a – Figure 6.8c, the treated samples had a lower prenatration depth than compared to the untreated condition. From the results it can be seen that the hardness of the treated condition increased compared to the untreated condition. The Nanoindentation testing of the hardness, elastic recovery

parameter and H^3/E^2 ratio are summerised in Table 6.2. Results show that the hardness, elastic recovery parameter and H^3/E^2 ratio increased as a result of the treatment.

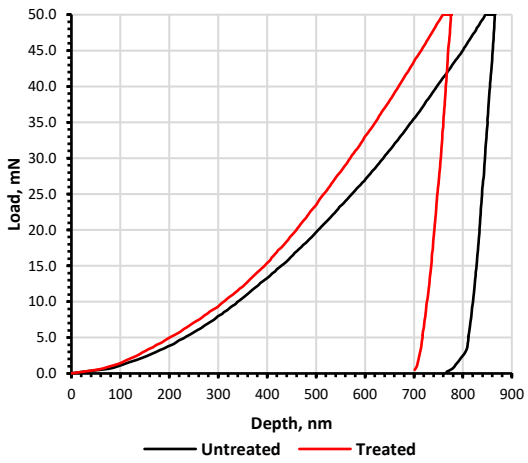

(a)

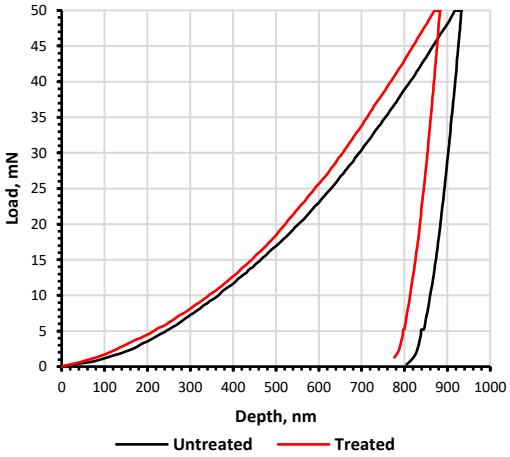

(b)

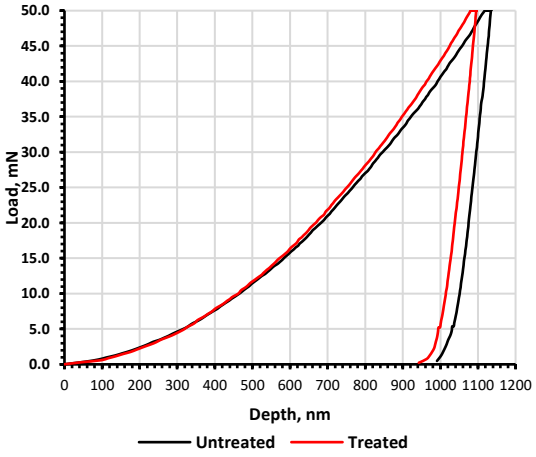

(c)

Figure 6.8. Typical nanoindetation loading-unlocading curves for treated and untreated (a) EN8 Steel, (b) NAB and (c) AA2014-T6 disc specimens.

Table 6.2. Mean (M) and Mean-square deviation (MSD) of treated and untreated nanoindentation results for EN8 steel, NAB and AA2014-T6.

Sample Condition		Hardness (GPa)		Elastic Recovery Parameter		H^3/E^2	
		M	MSD	M	MSD	M	MSD
EN8 Steel	Untreated	2.91	± 0.42	0.043	± 0.012	0.00044	± 0.00017
	Treated	3.41	± 0.34	0.051	± 0.006	0.00066	± 0.00044
NAB	Untreated	2.54	± 0.10	0.059	± 0.003	0.00087	± 0.00003
	Treated	2.60	± 0.12	0.062	± 0.003	0.00090	± 0.00005
AA2014-T6	Untreated	1.77	± 0.17	0.061	± 0.004	0.00066	± 0.00020
	Treated	1.85	± 0.19	0.063	± 0.005	0.00075	± 0.00112

6.3.4 Effect of alternating magnetic field treatment on magnetic domain structure of EN8 steel and NAB

Figure 6.9 and Figure 6.10 show the magnetic domain structure of untreated and treated EN8 steel and NAB samples respectively. When the magnetic moment vector direction between the magnetic probe and the magnetic domain of the sample is the same, the magnetic force probe and the magnetic moment vector are attracted to each other and will appear as dark regions in the MFM scan. If the magnetic domain structure of the sample repels the magnetic probe, the magnetic moment vector will appear as a bright region on the surface. From the results presented in Figure 6.9 for EN8 steel, it can be observed that after treatment there appears to be more magnetization and alignment of the domains within the sample, (Figure 6.9b). Furthermore, the magnetic domain structure after treatment appears more homogeneous than for the untreated sample. In the case of the NAB sample, the results of the MFM scan presented in Figure 6.10 appear to show evidence of more magnetization of the domains within the material.

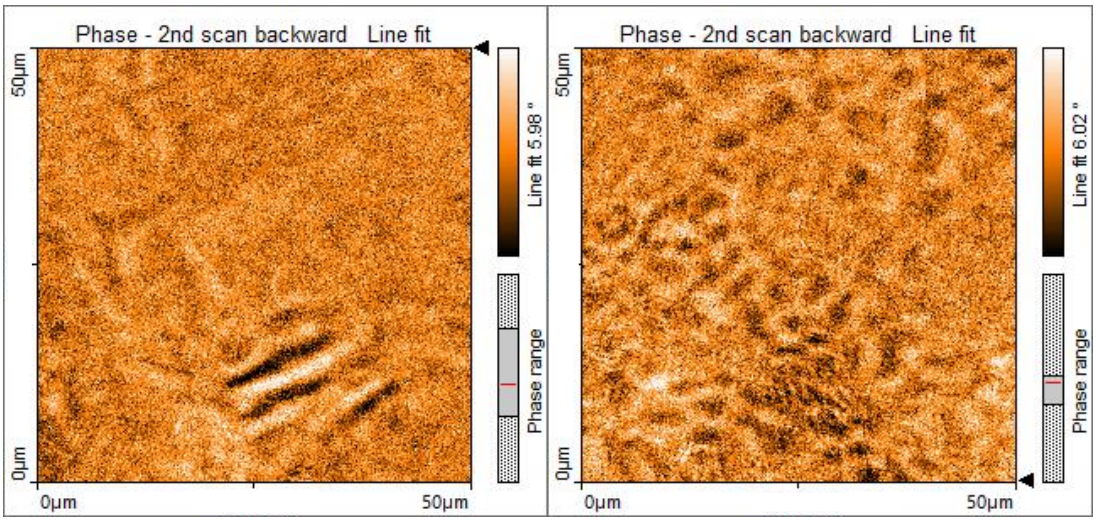

(a) (b)

Figure 6.9. Magnetic domain structure of (a) untreated and (b) treated EN8 steel.

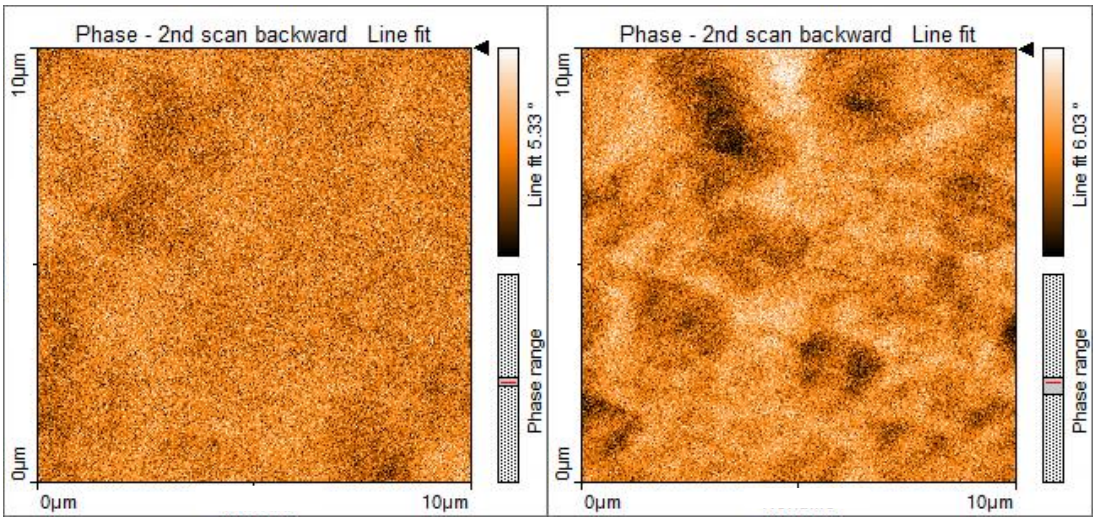

(a) (b)

Figure 6.10. Magnetic domain structure of (a) untreated and (b) treated NAB.

6.3.5 TEM analysis of the effect of alternating magnetic field treatment on dislocations and precipitates

The results of TEM examination of the untreated EN8 steel in Figure 6.11a show local areas of high-density of dislocation structures such as dislocation tangles and pile-ups along the grain boundary. Following the alternating magnetic field treatment, redistribution of dislocations

was observed as shown in Figure 6.11b. Furthermore, there appeared to be less dislocation pile up at the grain boundaries as well as less entanglement of dislocations.

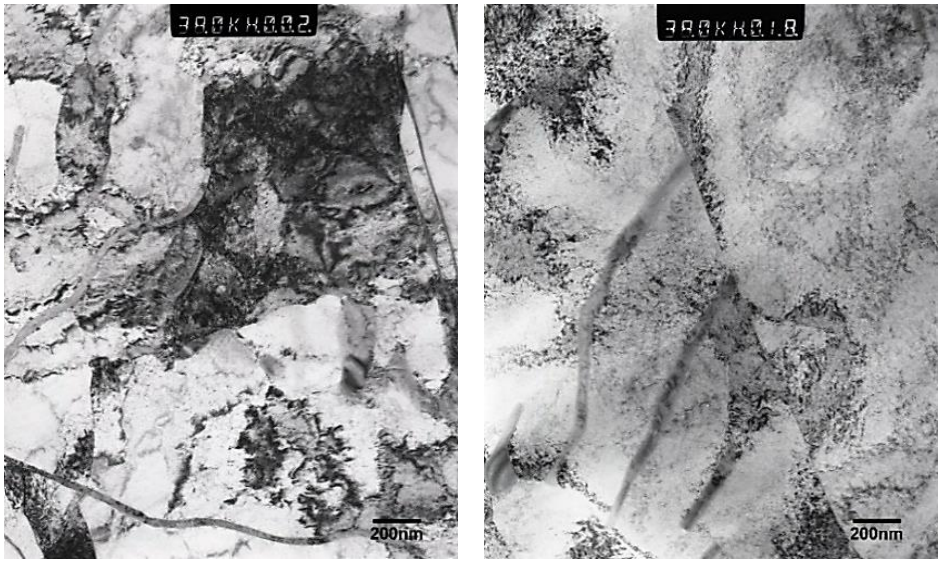

(a) (b)

Figure 6.11. TEM images of (a) untreated and (b) treated EN8 steel.

Typical bright field TEM micrographs of the treated and untreated NAB are shown in Figure 6.12. Figure 6.12a presents a typical area exhibiting a relatively high dislocation density; dislocation tangles, pile-ups and stacking faults are evident. Following the alternating magnetic field treatment, fewer dislocations, pile-ups and stacking faults were observed as shown in Figure 6.12b. There appeared to be fewer dislocation pile ups at the grain boundaries as well as less entanglement of dislocations. In addition, Figure 6.12b shows the emergence of more fine κ_{IV} spherical precipitates following alternating magnetic field treatment.

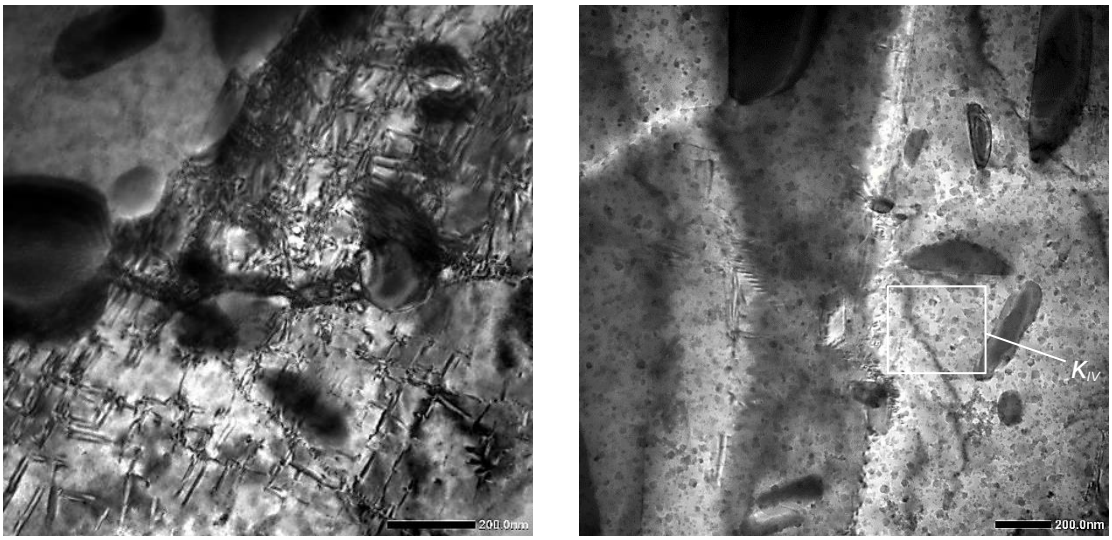

(a) (b)

Figure 6.12. TEM images of (a) untreated and (b) treated NAB.

Figure 6.13 presents typical bright field TEM micrographs of AA 2014-T6 before and after alternating magnetic field treatment. Figure 6.13a shows evidence of relatively high dislocation density pile-ups in the untreated AA2014-T6 sample, while fewer dislocation pile-ups are present in the treated sample as shown in Figure 6.13b. Furthermore, a higher density of fine needle-shaped precipitates was present for the sample in the treated condition. These precipitates are relatively uniformly distributed in the treated alloy. TEM mapping displayed in Figure 6.14 suggests that these are mainly GP zones and Θ'' precipitates [99-101, 104].

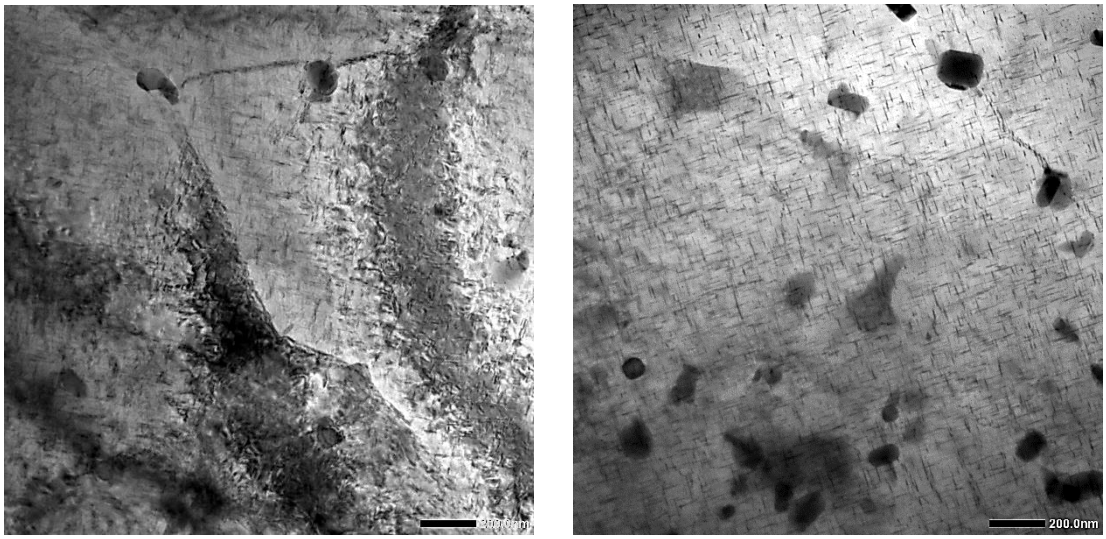

(a) (b)

Figure 6.13. TEM images of (a) untreated and (b) treated AA2014-T6.

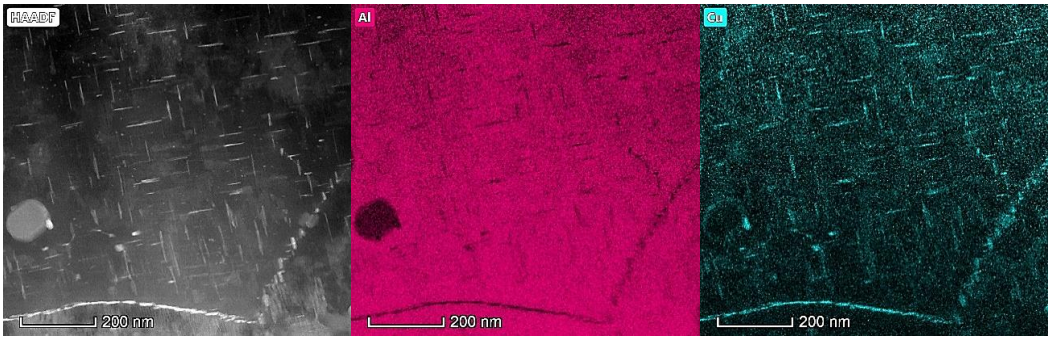

(a) (b) (c)

Figure 6.14. (a) TEM image and TEM mapping of (b) aluminium and (c) copper in treated AA2014-T6.

7 Cavitation Erosion Studies

7.1 Introduction

Cavitation erosion is highly destructive in nature and can cause severe loss in the performance of ships and may eventually lead to frequent docks, inspections and preventative maintenance or replacement of damaged parts. Studies conducted by Snegovskij et al. have shown that after magnetically treating propellers, the wear resistance capability increased by 1.5-2 times compared to the untreated samples. These researchers also reported that the cavitation-damaged area became smaller following magnetic treatment. It was proposed that the effect of the magnetic field treatment was to increase the mobility of atoms to rearrange the microstructure of the alloy leading to an improvement in the hardness of the propeller material. Unfortunately, Snegovskij et al. did not substantiate their explanation as they investigated only the macroscopic changes and no SEM/TEM or XRD results were presented to support the results of their research. Improvement in the erosion-corrosion resistance of the alloys after magnetic field treatment has generally been attributed to an increase in the hardness of the treated material [10, 124-126]. For example, Babutskyi et al. reported that there was an increase in the hardness of AISI 52100 steel following pulsed magnetic field (PMF) treatment. The authors proposed that there was destabilisation of the retained austenite due to the PMF treatment leading to partial transformation into martensite. Ma et al. also obtained an increase in hardness, after applying PMF treatment to high-speed steel. From XRD studies, they observed a 24% increase in dislocation density. It was suggested that the treatment caused dislocations to multiply and caused movement of dislocations. It was argued that this increase in dislocation density was the main cause of the increase in microhardness [126]. Another type of treatment, electropulsing, which involves treatment by an electrical current of high density was investigated by Qin et al. [127]. Their research investigated the effects of electropulsing on deformed pearlitic steel wire and reported an increase in the hardness value of the steel. TEM results showed that the effect of the electropulsing treatment led to strain relief and to the formation of finer grains.

In this chapter, the effect of alternating magnetic field treatment on the cavitation erosion resistance of EN8 steel, NAB, 70/30 brass and AA2014-T6 aluminium are studied. EN8 steel is a standard load-bearing steel that is widely used in applications such as automotive

components. NAB and 70/30 brass are two of the most common alloys used for marine applications due to their corrosion resistance and strength, while AA2014-T6 alloy is typically used in aerospace applications owing to its high strength-to-weight ratio.

7.2 Methodology

Chapter 4 section 4.6.3 (sample preparation for cavitation testing) describes the methodology of the preparation of the cavitation erosion samples. The nominal compositions range for AA2014-T6, EN8 steel NAB and 70/30 brass alloys are presented in Table 4.1 and Table 4.4 of Chapter 4.

7.2.1 Experimental setup for alternating magnetic field treatment

For alternating magnetic field treatment, each specimen was positioned inside a magnetizer. The magnetic field direction for the cavitation erosion samples is shown in Figure **3**.**5**b. The treatment duration was 30 minutes. An example of the registration of the magnetic field without a specimen in the magnetizer can be seen in Figure **3**.**6**b. The magnetic flux density was recorded using a Hirst GM08 Gaussmeter and the registration was conducted using a Picoscope 4224. The magnetic flux density recorded in the absence of the sample was 0.76 Tesla.

7.2.2 Characterization Methods

In this chapter the effect of AMF treatment on the cavitation erosion behaviour of EN8 steel, NAB, brass and AA2014-T6 was investigated. The alloys under investigation were treated and tested up to 6 hours for EN8 steel, AA2014-T6 and brass alloy. In the case of NAB cavitation erosion testing was conducted up to 8 hours. The morphology of the eroded surfaces was examined using scanning electron microscopy (SEM). Mechanical testing such as Vickers microhardness was conducted in order to understand the effects of the treatment. In addition, residual stress measurements were conducted using X-ray diffraction. Observations of the magnetic domain structure of EN8 steel and NAB before and after treatment were conducted using magnetic force microscopy (MFM). Electrical conductivity measurements of AA2014-T6 were conducted before and after treatment. Finally, changes in microstructure

were further studied using transmission electron microscopy (TEM). Further details to the methodology of these tests can be found in Chapter 4.

7.3 Results

7.3.1 Cavitation Erosion of EN8 steel, NAB, brass and AA2014-T6

The results of mass loss with time for EN8 steel, NAB, brass and AA2014-T6 alloy before and after treatment are shown from Figure 7.1a-d. The standard deviation is represented in the form of error bars in the figures. From the results, it can be observed that after 6 hours of cavitation erosion testing, the treated EN8 steel has a better erosion resistance of 35% compared to the untreated condition. In the case of the other alloys, the improvement in the erosion resistance at the end of the erosion tests for the treated NAB and AA2014-T6 was 42% and 20%, respectively. For the brass alloy, the improvement in the erosion resistance after 6 hours was 41% due to the treatment.

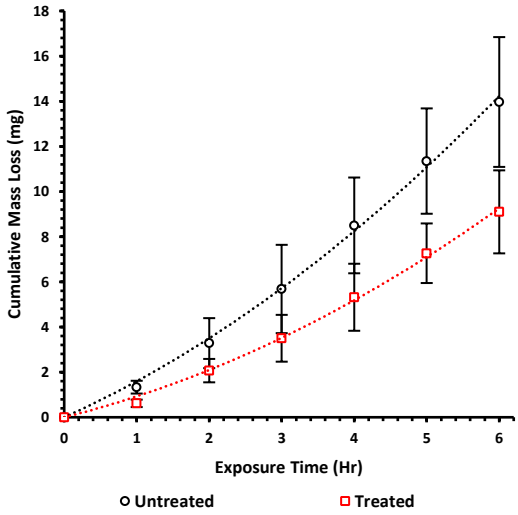

(a)

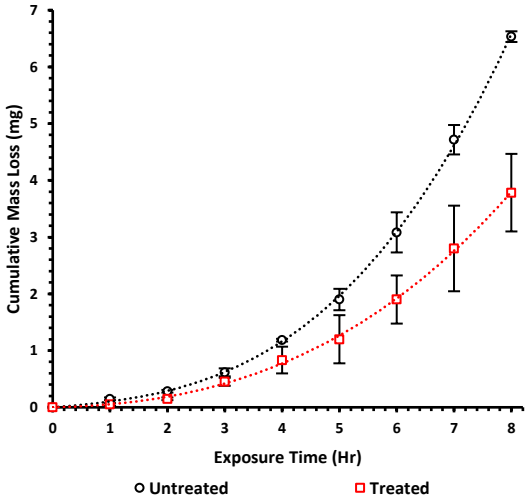

(b)

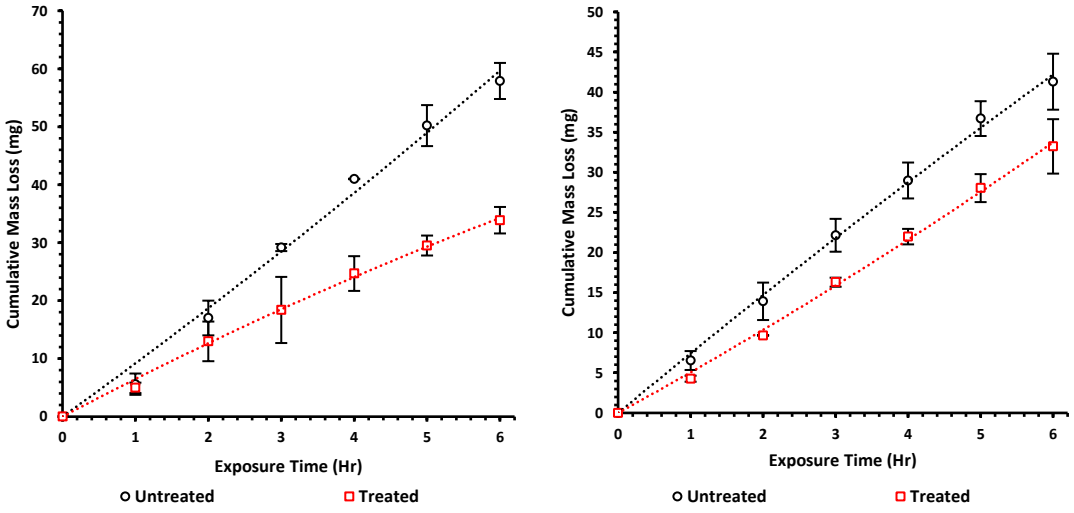

(c) (d)

Figure 7.1. Comparison of Cumulative cavitation erosion rate verse time untreated and treated (a) EN8 Steel, (b) NAB, (c) Brass and (d) AA2014-T6

7.3.2 Characterization of EN8 steel, NAB, brass and AA2014-T6

The measurements of microhardness and RS for the treated and untreated conditions of EN8 steel, NAB, 70/30 brass and AA2014-T6 alloys are shown in Table 7.1 which also shows the results of electrical conductivity for AA2014-T6. The percentage increase in microhardness after treatment for EN8 steel was 3.8%, for NAB 4%, for 70/30 brass 4.1% and for AA2014-T6 4.9%. From the RS results, it can be observed that there was a significant increase in compressive RS after treatment. After treatment, the percentage increase in compressive RS for EN8 steel was 45.5%, for NAB 121% and for AA2014-T6 88.4%. In the case of 70/30 brass, the percentage increase in compressive RS after treatment was 145.9%. The electrical conductivity measurements for AA2014-T6 showed a reduction in the electrical conductivity measurements of 24% after treatment.

Table 7.1. Mean (M), Mean-square deviation (MSD) and coefficient of variation (CV) for results of microhardness, electrical conductivity and Residual stress.

Sample Condition		Microhardness[1], H_V			Electrical Conductivity[2], MS/m		Residual Stress[3], MPa	
		M	MSD	CV	M	MSD	M	MSD
EN8 Steel	Untreated	265.35	6.87	0.0259	N.A.		-268.4	± 71.7
	Treated	275.33	6.82	0.0248			-319.9	± 39.0
NAB	Untreated	228.19	11.17	0.0490	N.A.		-64.1	± 128.7
	Treated	237.37	6.22	0.0262			-105.6	± 114.9
Brass	Untreated	155.29	12.9	0.0831	N.A.		-177.6	± 213.6
	Treated	161.71	8.78	0.0543			-436.7	± 106.6
AA2014-T6	Untreated	155.71	4.3	0.0276	23.23	0.008	-99.3	± 40.5
	Treated	163.35	1.84	0.0113	22.67	0.017	-129.5	± 20.9

[1] average of 60 indentations per sample (3 untreated and 3 treated samples); [2] average of 20 measurements per sample (3 untreated and 3 treated samples); [3] average of 3 untreated and 3 treated samples. M is a mean; MSD is a mean-square deviation and CV is a coefficient of variation (CV = MSD/M).

7.3.3 Scanning Electron Microscopy of eroded surface for EN8 steel, NAB, brass and AA2014-T6

SEM micrographs of the cavitation-eroded surface for EN8 steel, NAB, 70/30 brass and AA2014-T6 in the treated and untreated conditions are presented in Figure 7.2 to Figure 7.5. To investigate the initial stages of cavitation erosion, samples of EN8 steel, NAB and 70/30 brass alloy that had undergone cavitation erosion for 30 minutes were used. In the case of the AA2014-T6, SEM was conducted after testing for 5 minutes to study the initial stages of cavitation erosion. From the images, it can be observed that there is evidence of more pitting and erosion in the samples in the untreated condition when compared to samples in the treated condition. For EN8 Steel, NAB and AA2014-T6, the treated condition exhibited the least amount of erosion when compared to the untreated condition. In the case of the 70/30 brass alloy, the SEM morphology revealed that the least erosion occurred again in the treated condition. This trend is consistent with the cumulative results for wear loss.

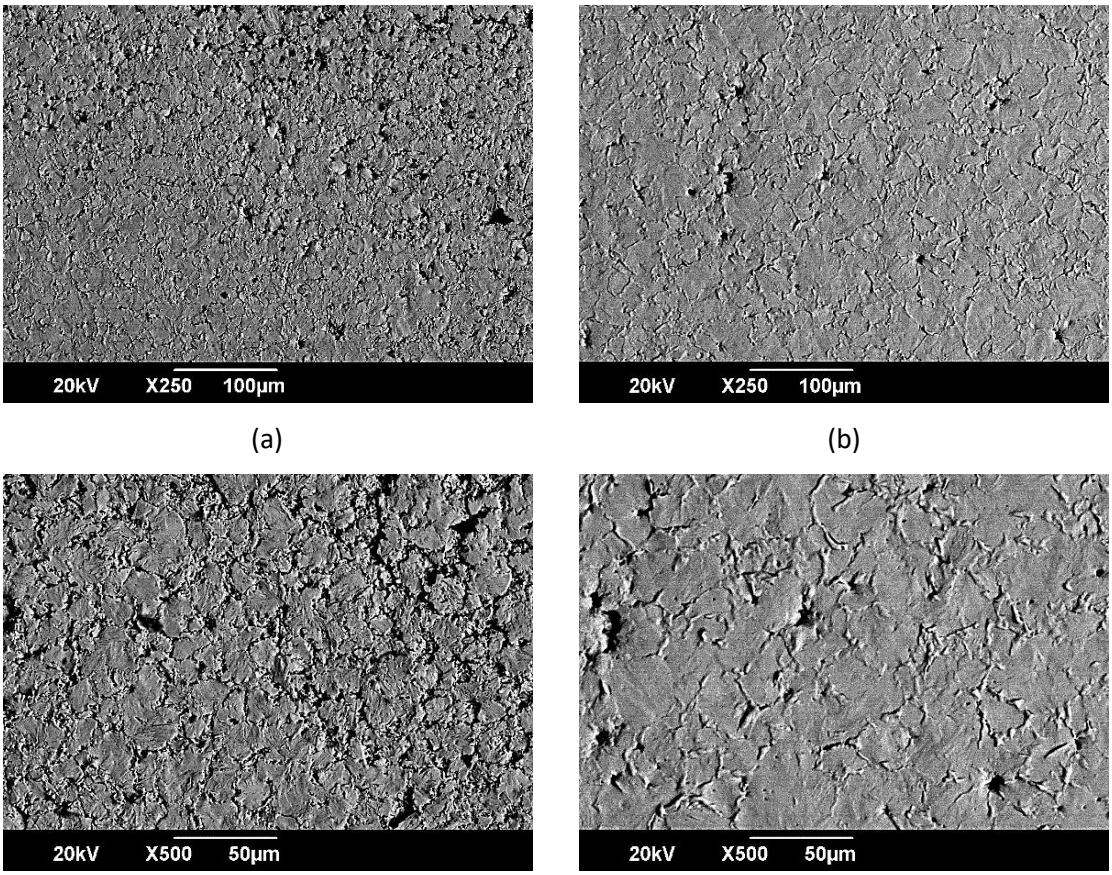

(a) (b)

(c) (d)

Figure 7.2. SEM images for 30 minutes cavitation erosion for (Figure 4a and 4c) EN8 Steel untreated and (Figure 4b and 4d) treated samples.

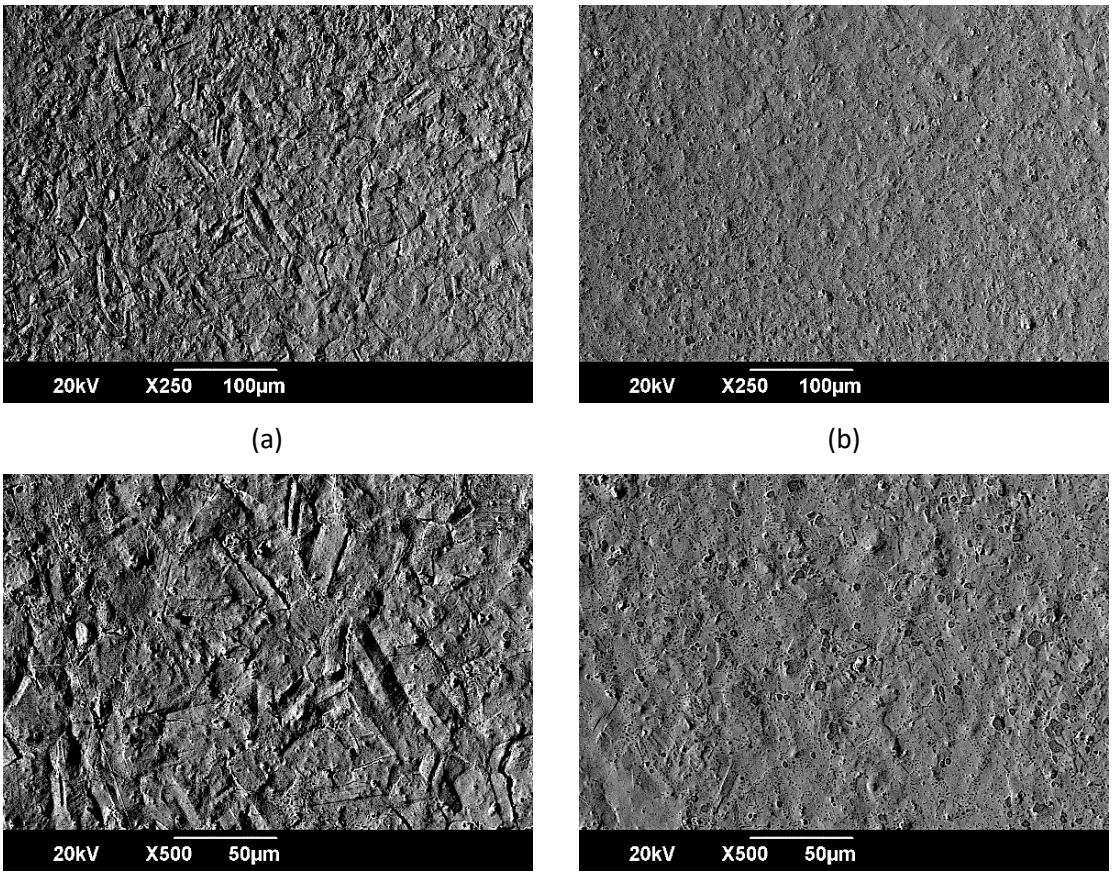

(a) (b)

(c) (d)

Figure 7.3. SEM images for 30 minutes cavitation erosion for NAB (Figure 5a and 5c) untreated and (Figure 5b and 5d) treated samples.

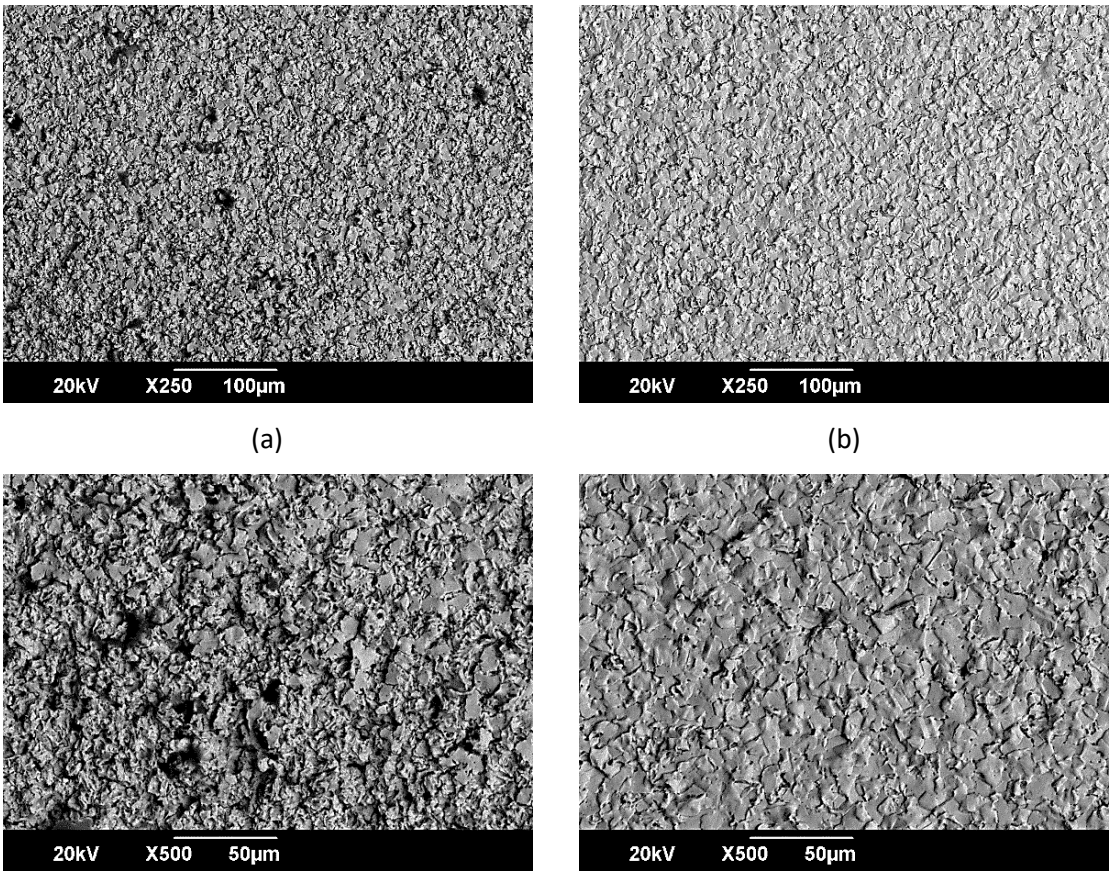

Figure 7.4. SEM images for 30 minutes cavitation erosion for 70/30 brass alloy (Figure 6a and 6c) untreated and (Figure 6b and 6d) treated samples.

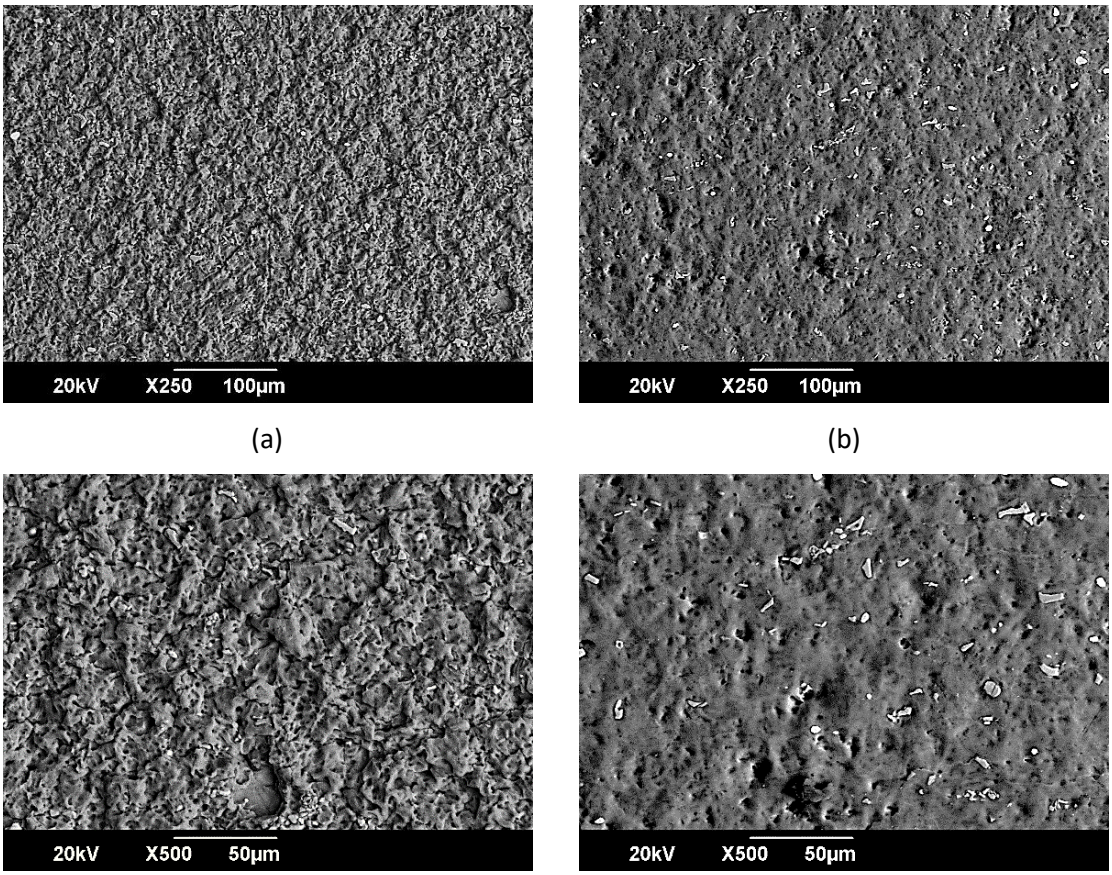

(a) (b)

(c) (d)

Figure 7.5. SEM images for 5 minutes cavitation erosion for AA2014-T6 (Figure 7a and 7c) untreated and (Figure 7b and 7d) treated samples.

7.3.4 Magnetic Force Microscopy of EN8 steel and NAB

MFM results for EN8 steel before and after treatment are presented in Figure 7.6a and Figure 7.6b, while Figure 7.6c and Figure 7.6d show the MFM results for untreated and treated NAB. From the results presented in Figure 7.6a and Figure 7.6b, it is evident that after treatment there is more magnetization and alignment of the magnetic domains as a result of the treatment. Moreover, the structure of the magnetic domain appears to be more homogeneous than in the untreated condition. The MFM scans in Figure 7.6c and Figure 7.6d suggest that the treated NAB exhibits larger and more defined areas of an attractive magnetic force gradient as opposed to the untreated condition. The formation of these larger and more defined areas of attractive magnetic force domain, are likely due to the formation of κ_{IV} precipitation (Fe_3Al and NiAl) which are magnetic.

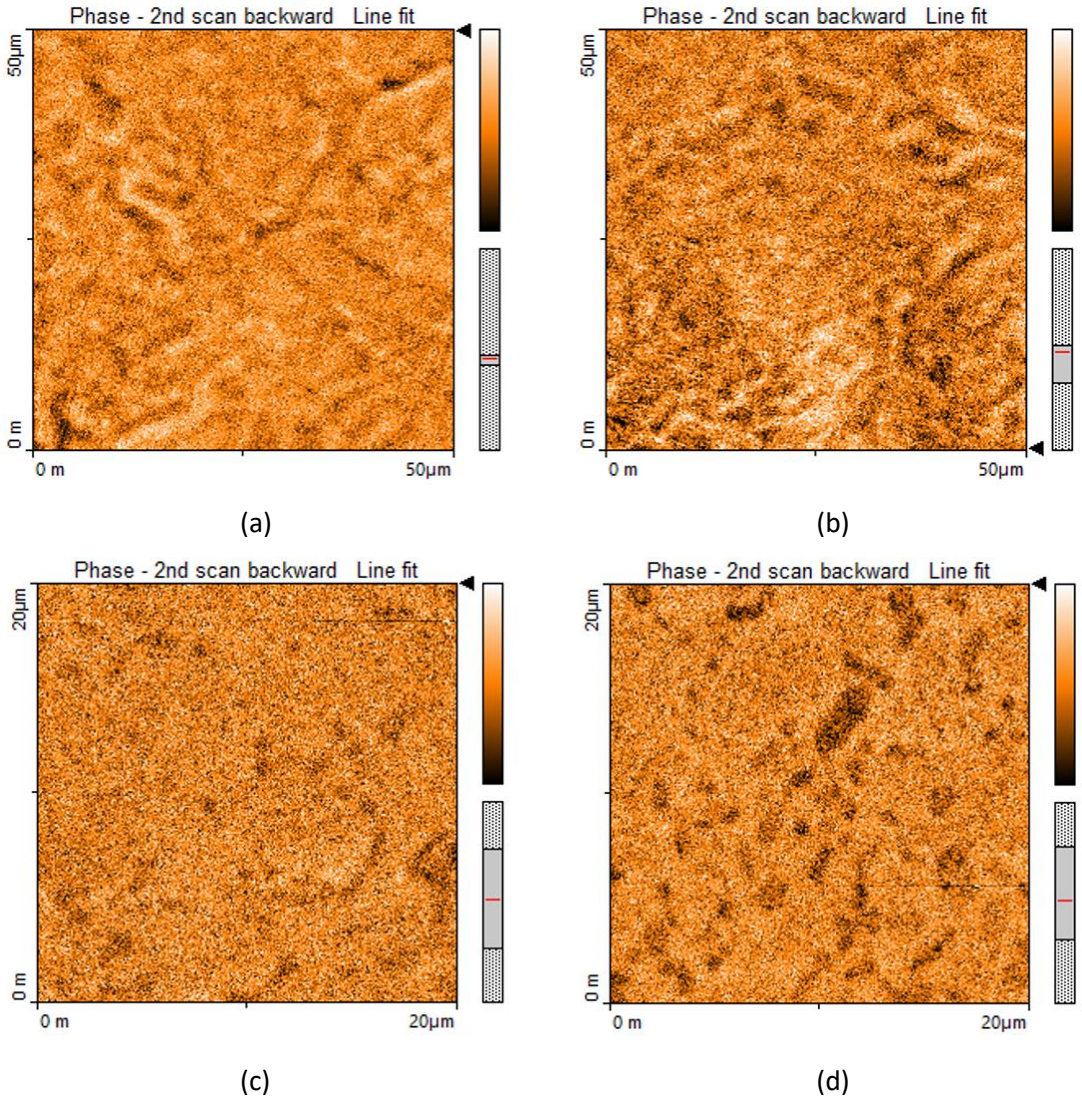

Figure 7.6. MFM images for EN8 steel (a) untreated and (b) treated and for NAB (c) untreated and (d) treated.

7.3.5 Transmission Electron Microscopy of EN8 steel, NAB, brass and AA2014-T6

Brightfield TEM micrographs for EN8 steel, NAB, 70/30 brass and AA2014-T6 in the untreated and treated conditions are shown in Figure 7.7 to Figure 7.10. An untreated EN8 steel sample in Figure 7.7a shows local areas of high-density of dislocation structures including dislocation entanglement and pile-ups along grain boundaries. In the case of the AMF treated condtition, redistribution of dislocations was observed to take place as shown in Figure 7.7b accompanied by reduction in the entanglement and pile up of dislocations at the grain boundaries as the

concentration of the dislocations became less localised. Similar observations of dislocation redistribution, reduction of dislocations at grain boundaries can also be observed in the treated conditions for NAB, 70/30 brass and AA2014-T6 in Figure 7.8 to Figure 7.10. These observations provide evidence that the treatment facilitates the movement of dislocations and recovery processes.

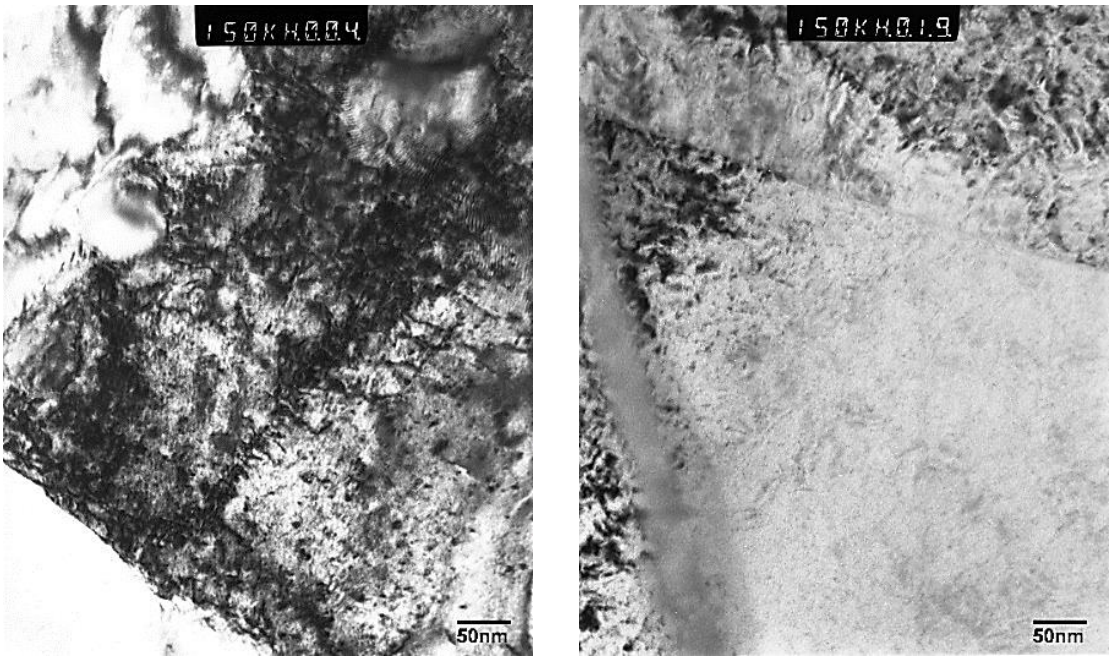

(a) (b)

Figure 7.7. TEM images of EN8 Steel (a) untreated and (b) treated samples.

In the case of the treated NAB, fewer stacking faults were observed as shown in Figure 7.8b. The reduction in the dislocation density took place by annihilation of dislocations as a result of the treatment. In addition, Figure 7.8b shows the formation of fine κ_{IV} spherical precipitates following the treatment. These were identified as κ_{IV} precipitates based on their characteristic shape and size [103].

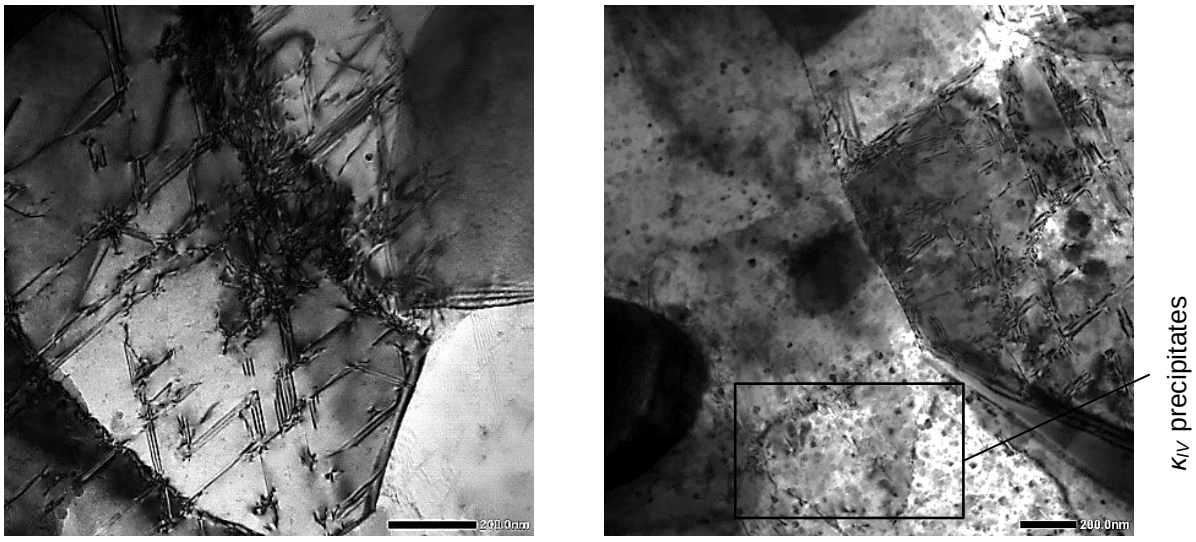

(a) (b)

Figure 7.8. TEM images of Nickel-Aluminium Bronze alloy (a) untreated and (b) treated. samples

Figure 7.9a and Figure 7.9b show the TEM micrographs for 70/30 brass in the untreated and AMF treated conditions, respectively. Again, there is evidence of dislocation redistribution and reduction of both dislocation entanglement and pile-up at the grain boundaries following treatment. Furthermore, ordering of dislocations is apparent in the treated condition as well as formation of bigger clusters of Fe impurities.

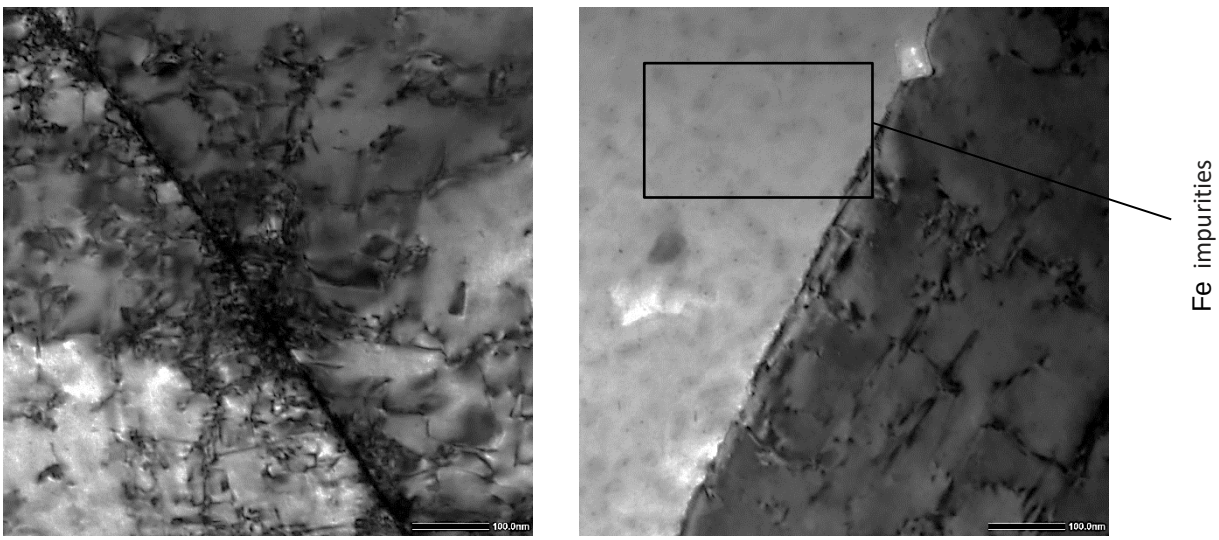

(a) (b)

Figure 7.9. TEM images of 70/30 Brass alloy (a) untreated and (b) treated samples.

TEM micrographs for AA2014-T6 alloy in the untreated and treated conditions are shown in Figure 7.10a and Figure 7.10b. In addition to the observations of dislocation redistribution, reduction of dislocation entanglement and reduction of dislocation pile-up at the grain boundaries Figure 7.10b shows that the presence of GP zones and theta double prime Θ'' are also more prevalent following treatment.

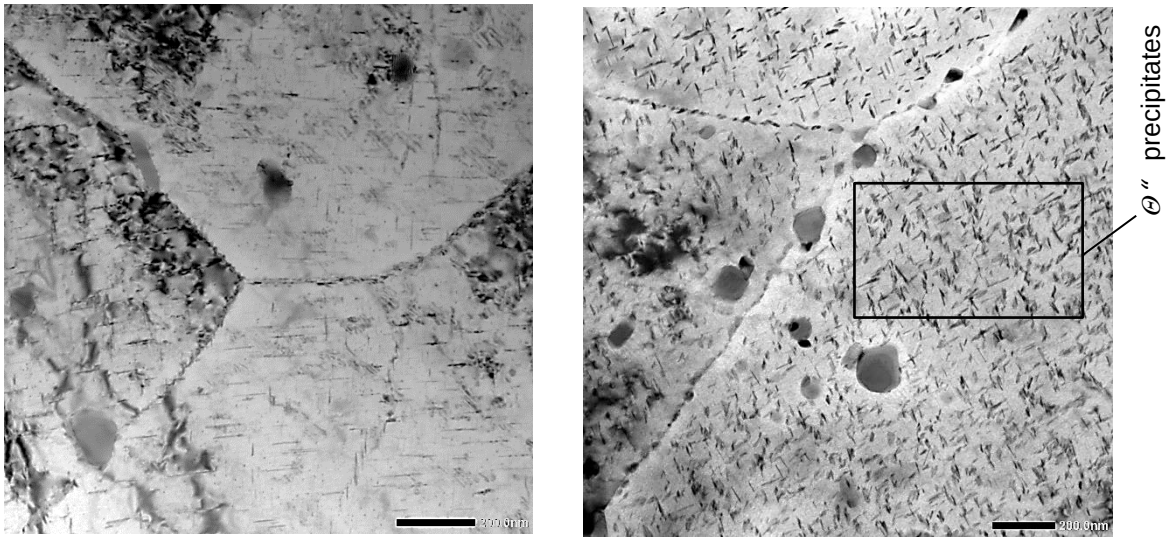

(a) (b)

Figure 7.10. TEM images of Aluminium Alloy 2014-T6 (a) untreated and (b) treated samples.

8 Discussion

8.1 Fatigue behaviour

The results in Chapter 5 show a significant increase in the fatigue endurance for both EN8 steel and AA2014-T6 alloy following alternating magnetic field treatment. Normally a higher fatigue endurance is achieved for metals with higher ultimate tensile strength (UTS). In the present study, minor increases in microhardness and UTS were observed for both EN8 steel and AA2014-T6 after the application of the magnetic field. This observation was attributed to a substantial increase in compressive RS in the near-surface layers of the treated metals; in addition, in the case of AA2014-T6, there was evidence of precipitation hardening. A slight increase in hardness and a significant reduction in the scatter of the hardness values for both alloys after treatment was also observed (Chapter 5 Table 5.1). The effect of RS on fatigue strength has previously been discussed by various researchers [111, 128, 129] who showed that a decrease in tensile RS and the redistribution of RS can be major factors of the fatigue endurance improvement achieved in the study. In the case of the treated AA2014-T6, an increase in the density of the strengthening precipitates and their homogeneous distribution (Chapter 5 Figure **5**.**5**b) after treatment was another reason for fatigue strength improvement. Electrical conductivity measurements were conducted for AA2014-T6 before and after treatment. Previous research has determined that there is a non-linear correlation between electrical conductivity and hardness/strength for heat-treatable aluminium alloys. The steady decrease of electrical conductivity is mainly due to the growth of very fine and coherent precipitates such as GP zones during the ageing process [101]. These GP zones are very effective in scattering electrons leading to a decrease in the electrical conductivity of the matrix. This electron scattering effect is induced by the coherent strains associated with the GP zone precipitates [101].

8.1.1 Simulation of AMF treatment for Fatigue studies

The recorded temperature using a thermocouple increase during the treatment was very low of the order of 12-14^{o}C and this is not sufficiently high to reduce RS and promote substantial precipitation. The thermal effect was thus too low to be considered as the cause of the

observed effects. Previous research has shown that the application of a high magnetic field results in both a thermal and a non-thermal effect [11, 82]. The mechanisms of the effect of magnetic field treatment may vary depending on the magnetic properties of the material; EN8 steel is ferromagnetic, while aluminium AA2014-T6 alloy is paramagnetic. To discuss the possible mechanisms, it will be useful to first analyse the treatment conditions affecting the two materials. As mentioned earlier, a magnetic flux density of 0.54T was measured in the absence of samples between the poles of the magnetizer. During the treatment of both metals, the settings of the magnetizer were not changed. This means that the AA2014-T6 samples were exposed to a magnetic flux of nearly the same value (0.54T) during the treatment as AA2014-T6 has a relative permeability, μ, of about 1. In the case of the EN8 samples, exposure of the metal took place at a higher magnetic flux density as steel is magnetized during external magnetic field exposure; the result was that the total magnetic field flux density affecting the material increased. In addition, eddy currents were induced into the samples during the treatment due to the stepwise change of the magnetic field direction (change of polarity). The value of the magnetic field for EN8 steel was 1.08T and was accompanied by polarity change every 5 seconds. Each change can be due to the induction of pulsed eddy currents into the samples. Therefore, the treated samples were affected by both the alternating magnetic field and the pulsed electric current (eddy currents).

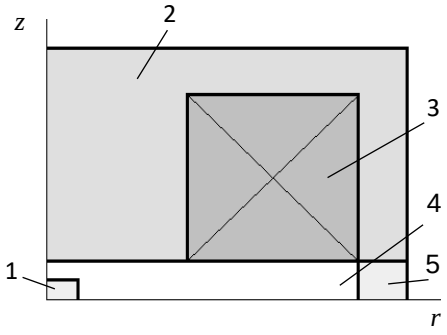

Figure 8.1. Schematic view of ¼ geometrical model of magnetizer with sample: 1 – sample, 2 – core; 3 – winding (consists of 70 turns), 4 – air, 5 – spacer.

Numerical modelling based on finite element analysis using QuickField 6 software was employed to estimate the treatment parameters (eddy currents and magnetic field distribution). This was conducted as a solution of the transient magnetic field problem and

was solved using 2-D formulations. A geometrical model for the calculations (Figure 8.1) was built based on the actual geometric parameters of the magnetizer and the samples (only tablet-shaped samples were modelled). The physical properties of the modelled materials used for the calculations are presented in Table 8.1.

Table 8.1. Physical properties of components of the model.

Property	Core (steel)	Spacer (steel)	Winding wire (copper)	EN8 sample	AA2014-T6 sample	Surrounding air
Electrical conductivity, MS/m	10	10	56	10	23	0
Relative permeability	B-H curve*	B-H curve*	1	B-H curve*	1	1

*The magnetic flux density vs magnetic field strength (B-H) curve for steel was taken from [130]

The time variation of the full current, *I(t)*, passing through a turn of the winding can be written in the form of a sign function:

$$\boldsymbol{I(t) = I_0 sign\left(sin\left(\frac{2\pi t}{T}\right)\right)}, \qquad \text{Equation 8.1}$$

where *T* is a period of time within which the field into the magnetizer acts in both directions (in the present case it is 10 s (see Chapter 3 Figure 3.5c). The value of I_0 was determined based on the best fitting of the calculated and registered profile of the magnetic field (0.54T). Calculations were carried out for time equal to 15s for the following three cases: (i) magnetizer without any samples and magnetizer with (ii) EN8 steel and (iii) AA2014-T6 samples located at the centre of the magnetizer (the central point of the samples was coincident with the central point of the magnetizer as shown in Figure 8.1).

The results of the numerical modelling of the treatment are presented in Figure 8.2 and show that the EN8 steel samples were subjected to a magnetic flux density of about 1.6T. Samples of AA2014-T6 were subjected to a 0.54T magnetic field. Changing the polarity of the magnetic field causes the induction of eddy currents to reach their maximum values at the cylindrical surface of the samples. These values are 5.5×10^6 A/m^2 and 4.8×10^6 A/m^2 for EN8 steel and

AA2014-T6 respectively (see Figure 8.3). The currents induced in the inner parts of the samples have lower values as eddy currents are distributed with a maximum value at the surface of the cylindrical sample.

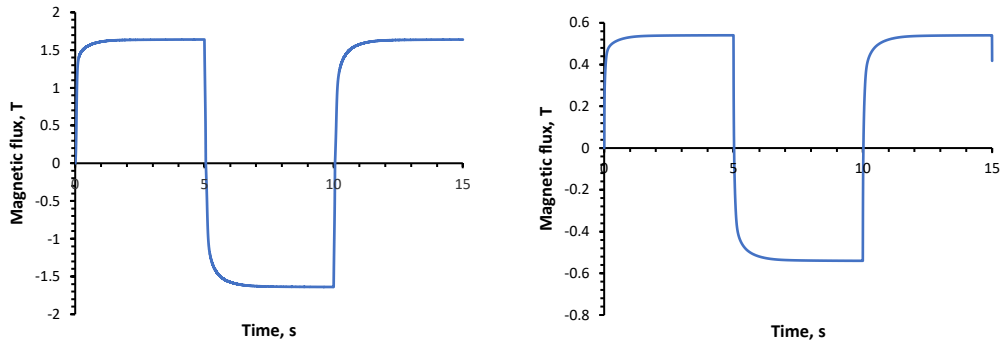

(a) (b)

Figure 8.2. Calculated magnetic flux density in the central point of sample (a) EN8 Steel and (b) AA2014-T6.

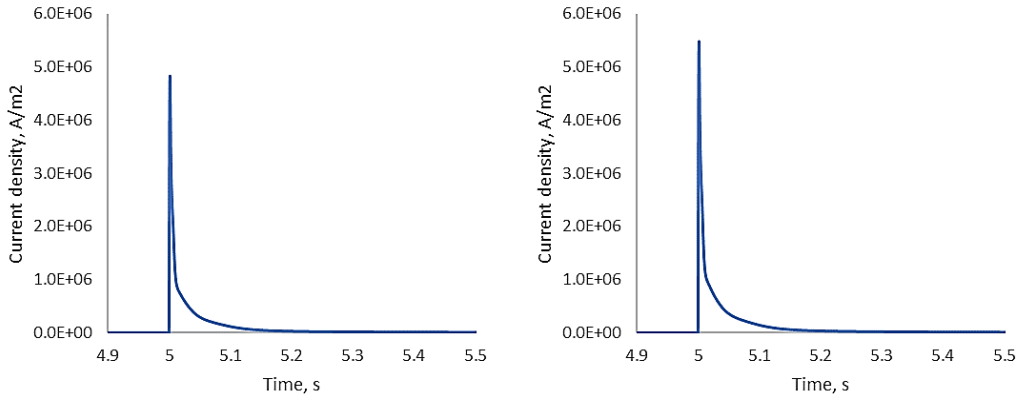

(a) (b)

Figure 8.3. Calculated eddy currents on cylindrical surface of samples: (a) EN8 Steel (b) AA2014-T6.

In spite of the difference in geometry between the fatigue and tablet-shaped samples used in this research, it can be assumed that the EN8 and AA2014-T6 samples were affected by similar levels of magnetic flux densities (close to 1.6T and 0.54T respectively) and pulsed eddy current densities.

The effect of pulsed electric current on the relaxation of RS has previously been discussed widely in the literature [131, 132]. It has been reported that stress relaxation and redistribution take place when the electric current density exceeds some threshold value which varies depending on the metal/alloy used and is in the range of 10^8 to 10^9 A/m^2. Based on the present numerical modelling, the current density values are of the order of about 5×10^6 to 6×10^6 A/m^2. These values are much lower than the threshold values for stress relaxation and the results suggest that the induced eddy currents are not the main cause of RS relaxation in the present study.

Some authors [12, 82, 83] argue that the effects of both a magnetic field and a pulsed electric current on the relaxation of stresses are based on an increase in dislocation mobility in metals. The increase of the mobility of dislocations is the result of their being depinned from obstacles due to the application of the magnetic field and/or the electric current. Having become free, the dislocations can travel due to the available stored energy (mainly RS) in the processed metal. This stored energy can be significant and has been shown to reach up to 60% of the work of the initial plastic deformation of metal [133]. Consideration of the fact that the EN8 steel and AA2014-T6 samples were obtained by cold-rolling and extrusion, the presence of stored energy in the two materials is most likely. The RS in the two untreated alloys was measured by XRD; a value of -260MPa was obtained for EN8 steel and -99MPa for AA2014 samples.

Several mechanisms of dislocation depinning are discussed in the literature , but in the present study that used the application of an alternating magnetic field, the depinning due to magnetic domain rotation [12, 105] is most probable for EN8 steel. Application of a magnetic flux density of 1.6T to the EN8 steel samples will be enough to cause magnetization of the metal and alignment of the magnetic domains and will increase their magnitude within the metal according to the direction of the external field [134-136]. As the field is altered into the opposite direction, it causes re-orientation of the magnetic domains. The domain walls are active obstacles for dislocations, therefore rotation of the domains can trigger dislocation depinning. Magnetostriction of the samples due to the application of the magnetic field can also be an additional factor triggering dislocation depinning [11, 81].

The above-discussed mechanisms of RS reduction for EN8 steel cannot be applied to explain the observed effects for the AA2014-T6 alloy as aluminium is paramagnetic. From this point of view, the most adequate model which can be used to explain the changes caused by the magnetic field in paramagnetic materials was presented by Molotskii [137-140]. The model is based on the suggestion that the magnetic field changes the spin multiplicity of the radical pairs formed by dangling bonds of dislocation cores and paramagnetic obstacles. As a result, depinning of the dislocations becomes more probable. According to Molotskii [137-140], a strong bond between atoms exists only in the ground singlet (S) state where the electron spins are antiparallel. In the excited triplet (T) state with parallel spins, the bonding is weak or even absent. Under the application of a magnetic field, the S-to-T transition becomes possible and the population of T states in dislocation-obstacle systems increases and enables dislocation depinning. In the case of AA2014-T6, this model can explain not only changes in RS due to the movement of dislocations after depinning but also the increase of the density of precipitates. The aluminium alloy used in the present research was supplied in the T6 temper so the alloy had been solution heat-treated and artificially aged. Usually, the ageing temperature and time are chosen to meet the required mechanical properties. At the same time, there is some level of residual or “free” solute Cu that remains in solid solution in the alloy and this level depends on the ageing conditions. Taking into account the above-mentioned model it can be suggested that the application of the magnetic field causes an increase in the population of T states in systems consisting of Al and “free” solute Cu atoms. As a result, after exposure of the AA2014-T6 alloy to the magnetic field, increased diffusion mobility of Cu atoms can lead to secondary ageing which is usually accompanied by an increase in tensile strength and fracture toughness.

The amplified mobility of dislocations during treatment can be the reason for the increased compressive RS in both metals within the near-surface region, as detected by XRD measurements in the present study. Since the outer free surface of the samples is a natural sink for dislocations, it is much easier for them to move towards the surface. This movement can cause strain accumulation in the near-surface region and a subsequent increase in compressive RS. In the study, the initiation of fatigue cracks took place at the surface.

Therefore, the increase of compressive RS caused by the magnetic field has resulted in the improvement of the fatigue endurance for both EN8 steel and AA2014-T6 aluminium.

The magnetic field triggers dislocation mobility supported by the stored energy as the driving force for dislocation rearrangement in both metals. It also leads to secondary precipitation in the AA2014-T6 alloy and causes the change to compressive RS and homogenisation of the fine microstructure. These effects result in the increase in the fatigue endurance of the investigated alloys and the appearance of a ductile component at the fractured surface of samples.

As highlighted in this study, the effects of magnetic treatment are rather complex and this is the reason why their complete understanding is still a challenge. For example, for both metals and as shown in this study, the effect of the induced eddy currents during treatment should not be excluded. In spite of their relatively low amplitudes and short period of time of individual pulsing, the number of pulses acting on the sample totalled 360 times. In turn, the eddy current pulses were accompanied by their own pulsed magnetic fields and therefore, more attention needs to be paid to solid-state and fundamental physics to further understand the observed effects.

8.1.2 Summary on Fatigue studies

In Chapter 5, an experimental study was carried out on the effect of alternating magnetic field treatment on the fatigue strength of ferromagnetic EN8 steel and paramagnetic AA2014-T6 aluminium alloy. Following the AMF treatment, both alloys have led to substantial increase in the fatigue endurance. However, only a minor increase in microhardness and tensile strength were achieved for both alloys. It is evident from SEM analysis that both alloys ductile fatigue fracture became dominant in the treated conditions. TEM analysis indicated that there is a reduction in the dislocation pile up after treatment for both EN8 steel and AA2014-T6 alloy. In the case of aluminium AA2014-T6, the treatment further generated strengthening precipitates in the material. Furthermore, the AMF treatment was accompanied by changes in magnetic field direction and in magnetic polarity and had a non-thermal effect on the two alloys leading to dislocation depinning and increased mobility of dislocations giving rise to an increase in the compressive stresses.

8.2 Friction behaviour

In Chapter 6, the investigation shows evidence of improvement in the wear and friction properties of EN8 steel, NAB and AA2014-T6 alloy as a result of alternating magnetic field treatment. Figure 6.1a-c shows that the COF for the untreated sample was rather unstable and was higher than that for the treated sample. In Figure 6.1d, it is shown that the specific wear rate was higher for the untreated samples for all alloys. The worn surface of the untreated samples exhibited greater roughness as well as deeper ploughing grooves with evidence of abrasive wear. This can be detected from the SEM micrographs in Figure 6.2 to 6.5 and in the 2D surface profile in Figure 6.5 to 6.8 for all alloys. In order to understand the reasons for the difference in the wear and friction characteristics of the two sets of samples, nanoindentation tests were carried out to evaluate the mechanical properties at the surface of the EN8 steel, NAB and AA2014-T6 alloys. The nanoindentation results revealed that following the treatment there was an increase in both the hardness and the H^3/E^2 ratio for all alloys. These results suggested that after treatment the resistance to plastic deformation of EN8 steel, NAB and AA2014-T6 had increased and thus exhibited lower wear. At the same time the loading-unloading results showed a small increase in the elastic recovery parameter from 4.3% to 5.1% for steel, 5.9% to 6.2% for NAB and 6.1% to 6.3% for AA2014-T6 following treatment. This implied that the contact between the pin and the treated alloys had become less plastic and more elastic leading to lower abrasion and to a more stable coefficient of friction resulting to a lower wear rate.

The main factor that has contributed to the increase in resistance to plastic deformation of the EN8 steel is the increase in compressive RS (and consequently surface hardness). The XRD data have shown a decrease in tensile RS in the near-surface layer of NAB and the presence of higher compressive RS for the aluminium alloy following the treatment. The effects of RS and hardness on wear behaviour are well-known [50, 51, 141-144] and are conventionally achieved by heat-treatment, coating and shot-peening. However, in the present investigation, a process based on the application of an alternating magnetic field has been used instead. Such a technique may be attractive in that it is fast and cost-effective; for its successful development it is important to understand the mechanism leading to changes in the RS and hardness of metals.

The TEM images presented in Chapter 6 (Figure 6.11 – 6.15) indicate a reduction in the dislocation pile-up at the grain boundaries and a more even dislocation distribution following the treatment for all alloys. This confirms facilitation of the mobility of dislocations due to the magnetic field. The increased dislocation mobility within the near-surface region caused dislocation movement to the outer surface of the sample as the surface is a natural sink for the dislocations. This, in turn, caused increased straining at the surface layer of the material and led to the creation of more compressive residual stresses or a reduction in tensile RS as detected by XRD (see Chapter 6 Table 6.1) and to higher micro/nano hardness [145, 146].

In addition to the reduction of pile-up of dislocations in AA2014-T6, the generation of more strengthening precipitates was also apparent. The TEM observations for the NAB alloy also showed more uniform dislocation distribution after treatment, while a substantially higher amount of the κ_{IV} phase (the main contributor to NAB strengthening) was detected. There is also evidence that the microhardness of the AA2014-T6 and NAB alloys increased as a result of the application of the alternating magnetic field treatment. The lower standard deviation for the microhardness results following treatment suggests that in both cases, the treatment had led to a more homogeneous microstructure. This type of homogenisation of the microstructure, together with reduced tensile RS at the surface of the sample creates conditions to reduce friction and wear. Dislocation movement is normally activated thermally; however, the measured increase in temperature during the treatment of both alloys was very low (about 10 - 11^{o}C) and such rise is not sufficiently high to promote any notable changes in microstructure and properties. It is therefore likely that these effects were activated athermally. This observation is in agreement with previous research by Tang et al. [11] who reported that the application of a pulsed magnetic field had brought about changes in the mechanical properties of 30CrMnSi high-strength steel through an athermal mechanism.

8.2.1 Simulation of AMF treatment for Friction studies

The observed effects arise not only from the alternating magnetic field, but also from the resulting eddy currents that were induced into the sample during the transition change of the magnetic field polarity which occurred every 5 seconds. Thus, the samples were exposed to both an alternating magnetic field and a pulsed electric current during processing. QuickField 6 software (Tera Analysis, Svendborg, Denmark) was employed in order to obtain the eddy

current distribution on the surface of the sample. The solution that was obtained was based on a 2D formulation of a transient magnetic field problem. The physical properties used for the finite element analysis is presented in Table 8.2.

Table 8.2. Physical properties of materials used during modelling.

Property	Core (steel)	Spacer (steel)	Winding wire (copper)	NAB sample	AA2014-T6 sample	EN8 steel sample	Surrounding air
Conductivity, MS/m	10	10	56	2.3	23	10	0
Relative permeability	B-H curve*	B-H curve*	1	1.5	1	B-H curve*	1

*The magnetic flux density vs magnetic field strength (B-H) curve for steel was taken from [130]

The full current time variation, *I(t)*, passing through one turn of magnetizer windings can be presented by the following equation:

$$\boldsymbol{I(t) = I_0 sign\left(sin\left(\frac{2\pi t}{T}\right)\right)}, \qquad \text{Equation 8.2}$$

where *T* is the period of time that the field acts in both directions of the magnetizer (5 s as shown in Chapter 6 Table 6.1b). The value of I_0 was determined based on the best fitting of the calculated and registered profiles of the magnetic flux density for the magnetizer in the absence of a sample; according to the results shown in Chapter 3 Figure 3.5a, the value of the magnetic flux density was 1.24T. Modelling was fulfilled for the magnetizer with an EN8 steel sample located at the centre of the magnetizer. Figure 8.4 shows a 1/4 geometrical model of the treatment arrangement that was used for the numerical modelling.

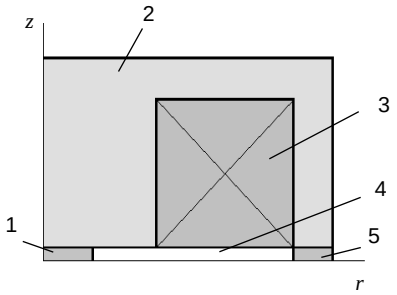

Figure 8.4. Schematic view of model used during simulation: 1 – disc sample, 2 – magnetizer core; 3 – winding (consists of 70 turns), 4 – air, 5 – spacer.

According to the modelling results, during the treatment the EN8 steel sample was exposed to a magnetic flux density of about 2.58T as it is magnetized under an external magnetic field. Table 8.3 shows the simulated current densities during polarity change of the external magnetic field on the flat sample surface for EN8 steel, NAB and AA2014-T6 near the outer radius of the sample.

Table 8.3. Simulated current densities for EN8 steel, NAB and AA2014-T6 pin on disc samples.

Alloy	EN8 steel	NAB	AA2014-T6
Current Density	5.2 x 10^6 A/m^2	1.2 x 10^6 A/m^2	9.2 x 10^6 A/m^2

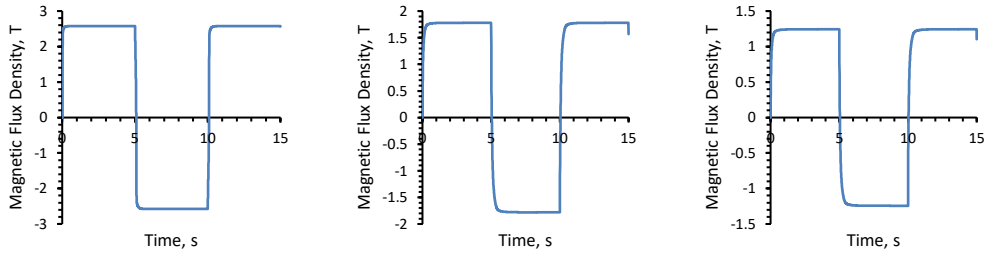

(a) (b) (c)

Figure 8.5. Calculated magnetic flux using the QuickField 6 software: (a) in central point of magnetizer for (a) EN8 steel, (b) NAB and (c) AA2014-T6 pin-on-disc alloys.

Previous studies have shown that notable changes in the mechanical properties and redistribution of residual stresses and their relaxation can take place when the electric current density exceeds a value of 10^8 A/m^2. As shown in Table 8.3 it is clear that the value of the calculated current density from the numerical modelling is significantly lower than the threshold level that is needed for changes in the mechanical properties to take place for all the alloys under investigation. Some researchers [12, 82, 83] have demonstrated that the application of a magnetic field can lead to relaxation and redistribution of residual stresses in ferromagnetic steels by activating dislocation movement. Pinned dislocations can become unpinned and move more easily due to the presence of stored energy (mainly in the form RS) that is caused during processing (cold rolling, drawing, welding, etc.) This stored energy in

manufactured metal components can be relatively high and has been shown to reach up to 60% of the work of the initial plastic deformation within the alloy [133].

In the present study that used the application of an alternating magnetic field to the EN8 steel, the depinning of dislocations due to magnetic domain rotation [105] is most likely to have occurred. The periodic magnetization of steel up to 2.58T, which according to the simulation took place during the treatment, is sufficiently high to cause magnetic saturation of the steel with gradual alignment of the magnetic domains. In addition, there is motion of the domain walls and expansion of the volume of those domains that have the largest magnetic moment coinciding with the direction of the external magnetic field. Under the treatment, the magnetic field alternates in the opposite direction and this causes reorientation of the magnetic domains. A change in the appearance of the domain structure before and after the treatment as shown from the MFM scans (Chapter 6 Figure 6.9), indicates significant changes in the domain structure of the material during the treatment. As magnetic domain walls are pinned by dislocations , the reversible rotation of the magnetic domains can trigger dislocation depinning from their quasi-stable states and lead to further motion that is driven by the stored energy in the cold-rolled EN8 steel. An additional factor that can trigger dislocation depinning is the magnetostriction of the samples due to the application of the magnetic field [11, 82]. The MFM results have revealed a more uniform distribution of magnetic domains, while the microhardness and RS measurements exhibit a lower mean-square deviation. These observations suggest that, in addition to improved hardness, there is evidence of microstructural homogenisation at the sample surface following the application of alternating magnetic treatment and that this also has a role in improving resistance to wear and reduction of the coefficient of friction.

In order to understand the driving mechanisms that lead to microstructural and property changes through the use of an alternating magnetic field, it is important to consider the nature of the two alloys; for example, NAB has soft ferromagnetic properties due to its composition (which contains iron and nickel), while AA2014-T6 alloy is paramagnetic. In addition, there must be consideration of the applied parameters of the external field. In the current work, the magnetic flux density that was applied between the two magnetic poles was 1.24 T; the AA2014-T6 samples were thus exposed to a magnetic flux density of 1.24 T because this alloy

has relative permeability, μ_{AA2014}, of 1. However, the NAB samples encountered a higher magnetic flux density, as this bronze has relative permeability, μ_{NAB}, of 1.5 and it is magnetised under an external magnetic field; therefore the total magnetic flux density to which the NAB alloy was exposed was higher in comparison to that for AA2014-T6. In addition, there must be consideration of the fact that the stepwise change of the magnetic field polarity had induced eddy currents into the samples. In total, the change of the magnetic flux density was 2.48 T every 5 seconds for AA2014-T6 alloy. During each polarity change, pulsed eddy currents were induced and therefore the samples were exposed to not only an alternating magnetic field but also to a periodic pulsed electric current.

According to the numerical modelling results, the NAB samples were exposed to a magnetic flux density of around 1.8 T (due to its relative permeability of 1.5). The change of the polarity of the magnetic field (see Figure 8.5) causes maximum eddy currents (current density) of 1.26 x 10^6 A/m^2 and 9.2 x 10^6 A/m^2 for NAB and AA2014-T6 respectively (see Table 8.3); these maximum values were reached at the cylindrical surface of the samples. A number of researchers including Baranov et al. [131] and Stepanov et al. [147] observed the relaxation of RS in metals as a result of the application of a pulsed electric current. According to Baranov et al. [131], notable changes in the mechanical properties and relaxation as well as redistribution of RS occur when the electric current density exceeds a threshold level of about 1 x 10^8 to 1 x 10^9 A/m^2. Following on from this, Stepanov et al. [147] observed relaxation of RS in stainless steel, copper, molybdenum and tantalum by applying even higher current densities that exceeded 1 x 10^{10} A/m^2. Lu et al. [80] also reported relaxation of RS in 1070 steel, but by using a pulsed magnetic field. In their work, they operated under conditions of what they termed “strong pulsed magnetic treatment,” but did not define the value of the magnetic flux density. The results of numerical modelling from the present study show that the current density values during the treatment were significantly lower than the threshold level proposed by Baranov et al. [131]. These results suggest that in the present investigation, the induced eddy currents were not the main cause of RS relaxation.

The work of Molotskii has provided the theoretical basis to suggest that the application of a magnetic field to a paramagnetic alloy (like AA2014) may trigger movement of dislocations. It is proposed that such motion is the result of the release of internal (residual) energy that

accumulates in the material during manufacture. It was also suggested that the bonding energy of dislocation-to-paramagnetic obstacles (like impurities, vacancies, etc.) is dependent on the spin multiplicity of the radical pairs that are formed by the dislocation core and the obstacles. The radical pairs occur either in a singlet (with high binding energy) or in a triplet (with low binding energy) spin state. Application of a magnetic field may induce a transition from a singlet to a triplet state. As a consequence, the number of triplet states increases and weak coupling facilitates the unpinning of dislocations from obstacles. This stimulates dislocation movement due to the presence of a random field of long-range RS (stored internal energy). As AA2014-T6 is paramagnetic, the above-mentioned mechanism can explain the increase in the number of strengthening precipitates during the treatment. The alloy in the as-received state still contains some residual or "free" solute Cu in solution with aluminium. The application of the alternating magnetic field has caused an increase in the rate of diffusion of "free" solute Cu atoms to precipitate out of the solid solution to form GP zones and θ''. These changes can be referred to as secondary ageing which is usually accompanied by increased strength of aluminium alloys.

The TEM and XRD analyses have shown changes in the microstructure of the NAB due to alternating magnetic field treatment. These changes are in the form of fewer and less tangled dislocations and more cuboidal κ_{IV} precipitates. The composition, morphology and crystal structure of the κ precipitates were recently studied by Wood who has reported that the κ_{IV} precipitates (along with the precipitates κ_I, κ_{II} *and* κ_{Iii} summarised in Table 8.4) have an ordered crystal structure that is based on either Fe_3Al or NiAl. An investigation by Shull et al. demonstrated the magnetic nature of Fe_3Al; according to Mitra [148], NiAl is also magnetic. Like all magnetic materials, these structural phases contain magnetic domains. When in the as-received state (without the application of the magnetic field), the magnetic moments of atoms in the NAB phases line up with one another, creating small magnetic domains oriented in random magnetisation directions. This situation is evident in Figure 8.6a, where randomly oriented magnetic domains in untreated NAB are presented schematically. Figure 8.6d presents an actual MFM scan of the untreated NAB (from the selected area shown in Chapter 6 Figure 6.10).

Table 8.4. Chemical composition of the individual phases in C98500AC-NAB alloy [149].

Micro-structural phases	Chemical composition in % weight						Morphology	Structure
	Cu	Si	Al	Mn	Fe	Ni		
Alloy	80.25	0.03	8.79	3.56	4.63	5.10	-	-
□	85.39	–	7.19	0.87	3.35	3.20	FCC solid solution	-
κ_I	15.08	1.66	13.29	1.72	57.53	10.72	Rosetta globular	Fe_3Al (DO_3)
κ_{II}	17.61	1.52	14.02	1.50	51.90	13.44	Dendritic	Fe_3Al (DO_3)
κ_{III}	45.15	–	18.76	1.19	10.90	24.00	Lamellar	NiAl (B_2)
κ_{IV}	13.00	7.00	19.00	2.00	64.00	6.00	Cuboidal	Fe_3Al (DO_3)

The application of an external magnetic field of 1.24 T causes rotation of the magnetic domains, yielding a higher magnetic flux density and magnetizing of NAB at levels up to 1.8 T. It can be suggested that at such levels of magnetic flux density, saturation will take place and the magnetic domains opposing the field will be swallowed up and disappear at least in some volume of the alloy with a high concentration of Fe_3Al and NiAl phases. A single-domain structure thus appears there as presented in Figure 8.6b. As reported by Chesnel [150], when the magnetic flux density approaches zero, the alternating polarity of the magnets will lead to changes in the magnetic domain pattern and to a gradual increase in the number of domains. On the other hand, when the applied magnetic field approaches its maximum value, a decrease in the number of magnetic domains takes place. This alternating process continues throughout the treatment. The effect of the treatment is to minimise the internal energy of the material. This will involve a spontaneous division into separate magnetic domains with some final remanent domain pattern as shown in Figure 8.6c and Figure 8.6e. According to Celik et al. and Wu et al. , the mobility of dislocations will increase substantially due to such domain wall movement. In addition, magnetostriction accompanying domain rotation induces micro-strains in the material. Altogether these factors can provide the driving mechanism for the redistribution of dislocations in NAB when alternating magnetic field treatment is applied. The process of magnetic domain rotation can be used to explain the behaviour of the κ_I, κ_{II} and κ_{III} phases, but the κ_{IV} precipitates exhibit significantly different behaviour due to their smaller size in comparison to the other precipitates. As shown in Chapter 6 Figure 6.15b, most of the κ_{IV} precipitates have size ranging from about 10 nm to 30 nm. Within precipitates of this size range, magnetic particles have a single-domain state without magnetisation as

reported by Binns and they remain in this state for all applied magnetic fields [151, 152]. When in this state, they are characterised by high coercivity, therefore during reversing of the magnetisation of the κ_{IV} phase, the widest possible hysteresis loop for a particle of that composition is achieved. As a result, the largest possible work is performed on the material by the external field and this is dissipated as heat. This increased heating which is most likely localised around the κ_{IV} phase particles can promote extra diffusion mobility of "free" solute Fe and Al atoms to form more κ_{IV} (ie. Fe_3Al) precipitates from the retained β-phase and the α-phase.

Another possible mechanism that can promote diffusion mobility of solute Fe and small κ_{IV} phase particles is based on dipolar interaction which can cause an attraction or repulsion of magnetic dipoles. The energy levels of these interactions can be compared by considering a group of Fe atoms or single-domain κ_{IV} phase particles of the same size and magnetic moment, m. Let the distance between two atoms (particles) be *r*. When a magnetic field is applied, the magnetic moment of atoms or particles will be aligned along the field direction as presented in

Figure 8.7a. According to Zhang et al. and Cyrot [153], in this case the magnetic dipolar interaction energy, E_D, can be expressed as:

$$\boldsymbol{E_D = -\frac{\mu_0 m^2}{4\pi}\frac{3cos^2\theta - 1}{r^3}} \qquad \text{Equation 8.3}$$

where μ_0 is the vacuum magnetic permeability and θ is the angle between the vector r and the z-axis. This equation shows that the magnetic dipolar interaction energy, E_D, depends on the relative position of the interactive dipoles which is described by a geometric factor, f, where $f = \frac{3cos^2\theta - 1}{r^3}$. Figure 8.7b presents the calculated values of the geometric factor as a function of the relative position of the dipoles.

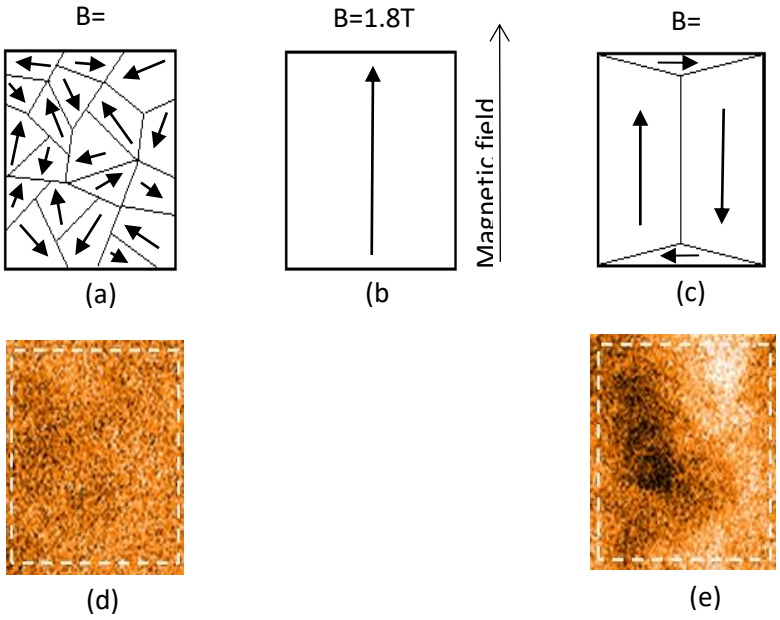

Figure 8.6. Domains and domain wall kinetics in tested samples; initial condition (a), after maximum magnetic field (saturation) (b), after treatment (c), fragment of MFM scan of sample in initial condition (see its location in Figure 7a) (d) and fragme.

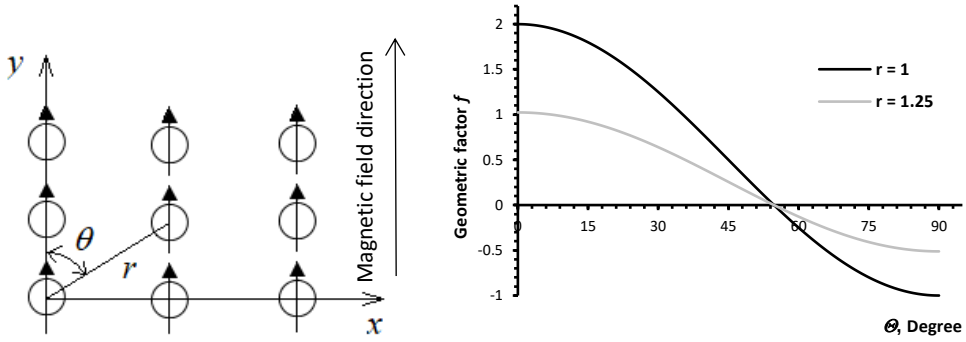

Figure 8.7. Alignment of Fe atoms or κ_{IV} single-domain dipoles under a magnetic field (a); variation of the geometrical factor *f*, of the dipolar interaction energy E_D, for $0^0 \leq \theta \leq 360^0$ and for $r = 1$ and $r = 1.25$ (b).

From the calculated estimates of the geometrical factor, f, when two dipoles are parallel to the magnetic field direction, the magnetic dipolar interaction energy, E_D, is negative and

the dipoles attract each other. On the other hand, when two dipoles are oriented perpendicular to the field direction, they repulse each other as the magnetic dipolar interaction energy, E_D, is positive. The maximum energy of attraction is two times higher than the maximum repulsive energy. Under this condition, the higher diffusion mobility of Fe atoms and Fe_3Al nuclei can facilitate the formation of more κ_{IV} precipitates.

Another source of κ_{IV} precipitates can be the eutectoid transformation of the β phase to the copper-rich α-phase plus κ eutectoid and further secondary κ precipitation based on Fe_3Al and NiAl. The XRD results in Figure 8.8 show that at $2\theta = 49.8^0$, there was a slight increase in the copper-rich α-phase as a result of the transformation of the β-phase to the α-phase and secondary κ precipitates (most probably κ_{IV}). The intensity of κ at $2\theta = 44.17^0$ increased only marginally and the peak has shifted slightly to the left (to a lower angle) after treatment. The width of this peak has also increased slightly as the shift (to the left) on the left-hand side of the peak is greater than the shift (to the left) on the right-hand side of the peak. This suggests that the secondary κ_{IV} precipitates produced by the treatment have a slightly higher lattice parameter. Based on results of the effect of composition on the lattice parameter of Fe_3Al as observed by Taylor and Jones , this change suggests that the secondary κ_{IV} may contain more iron and/or nickel.

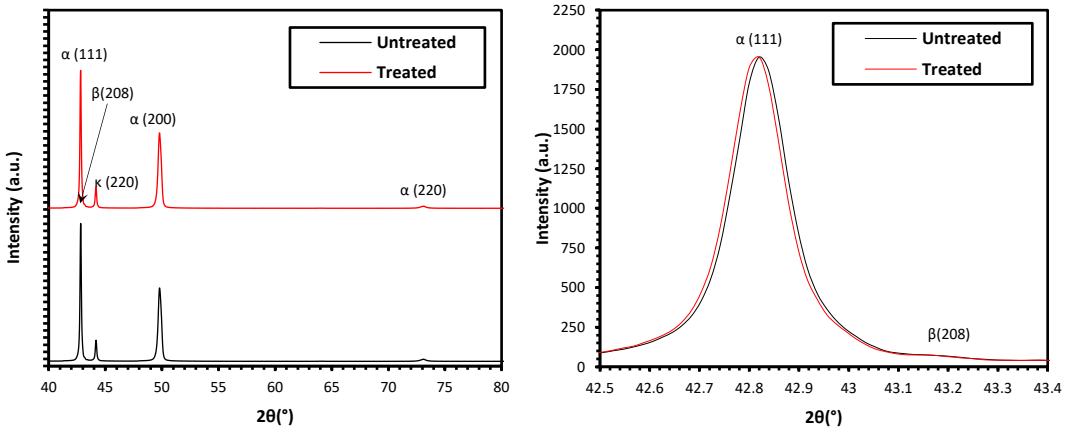

(a) (b)

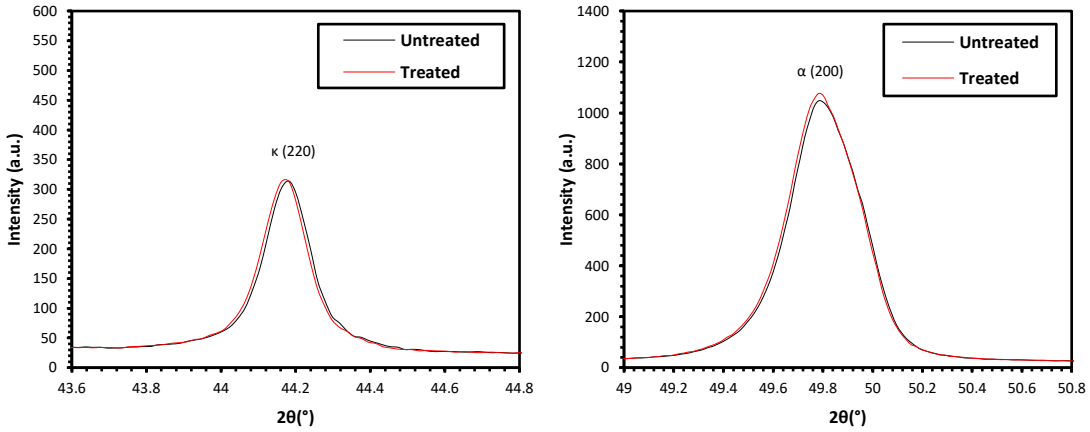

(c) (d)

Figure 8.8. XRD pattern NAB and diffraction peak profiles of untreated (black) and AMF treated (red) samples XRD patterns (a), (111) diffraction peak (b), (220) diffraction peak (c) and (200) diffraction peak (d).

The observed precipitation strengthening of both NAB and AA2014-T6 significantly improves the friction and wear of the two alloys. The reduction of tensile RS for the NAB alloy and the generation of compressive RS at the surface of the AA2014-T6 has benefited both alloys in terms of their tribological behaviour. These changes have taken place due to the increased mobility of dislocations as a result of alternating magnetic field treatment. The movement of dislocations towards the surface is more favourable since the external free surface of the samples can act as a natural sink for dislocations. Such movement is likely to create strain accumulation within the near-surface layer with a subsequent decrease of tensile RS in NAB and an increase of compressive RS in AA2014-T6.

As the research continues in order to gain better understanding of the mechanism leading to the effect of alternating magnetic field treatment, the possible influence of the induced eddy currents must not be dismissed entirely. Despite their relatively low amplitude (5.2 x 10^6 A/m^2 for EN8 steel, 1.26 x 10^6 A/m^2 for NAB and 9.2 x 10^6 A/m^2 for AA2014-T6) and their brief existence, eddy currents can create an additional back-force facilitating electromigration of both atoms and dislocations in metals to various equilibrium positions.

8.2.2 Summary on Friction studies

In Chapter 6, the effect of alternating magnetic field treatment on the friction and wear resistance of EN8 steel, NAB and AA2014-T6 aluminium alloy using AISI52100 steel ball bearing as the counter face material was investigated by carrying out a series of mechanical and tribological experiments. Based on the observations shown, the values of the specific wear rate, wear scar width and coefficient of friction for the treated were lower than those for the untreated samples as a result of a treatment. The tested alloys exhibited improved mechanical properties following alternating magnetic field treatment which led to an increase in the microhardness. XRD RS analysis revealed a decrease in tensile residual stresses in the near-surface layer of NAB and the formation of compressive (from tensile) residual stresses for the AA2014-T6 alloy and EN8 steel following the treatment. In addition, TEM analysis for three alloys indicated that there was a reduction in the dislocation pile up and a more uniform dispersion of dislocations in the treated samples, while in the case of the NAB and AA2014-T6 alloys, the treatment facilitated the generation of strengthening precipitates.

The precipitation mechanisms for a paramagnetic material like AA2014-T6 under the application of an alternating magnetic field can be affected by the multiplicity of the radical pairs that are formed by the dislocation core. This can also facilitate such dislocation movement to bypass obstacles and can enable diffusion mobility of “free” solute Cu atoms in the aluminium matrix. In the case of the soft magnetic NAB, dislocation mobility and precipitation of the κ_{IV} phase after alternating magnetic field treatment can be the result of magnetic domain rotation and dipolar interaction.

For the EN8 steel, the alternating magnetic field treatment was accompanied by changes in magnetic field direction and in magnetic polarity and had a non-thermal effect leading to dislocation depinning and to increased mobility of dislocations towards the outer surface of the samples. This gave rise to an increase in the compressive stresses and to an increase in microhardness; these changes are responsible for the improved wear resistance and reduction of the coefficient of friction.

8.3 Cavitation Erosion behaviour

In Chapter 7, the effects of alternating magnetic field treatment on the erosion resistance of NAB, EN8 steel, 70/30 brass and AA2014-T6 were investigated. The erosion rate, topographical and microstructural analyses for the cavitation erosion experiments were conducted on all four alloys. The experimental results show improvement in the erosion resistance of NAB, EN8 steel, 70/30 brass and AA2014-T6 compared to the alloys in the untreated condition. This includes an increase in the microhardness and to higher compressive residual stresses resulting in higher erosion resistance.

While previous investigations [10, 104, 108] have demonstrated improved mechanical properties in several alloys, researchers still lack complete understanding of the effect of a magnetic field on the behaviour of metallic materials. Specifically, the magnetic nature of different alloys has not been addressed in earlier research. The present work attempts to extend current knowledge in this area by considering the response to the treatment of alloys that have different magnetic behaviour at room temperature; EN8 steel is ferromagnetic, AA2014 alloy is paramagnetic, while the 70/30 brass is diamagnetic. The NAB alloy is also diamagnetic, but it can form tiny ferromagnetic precipitates and so it can be described to have "soft" magnetic properties. This presents an opportunity to discuss the mechanisms governing the observed enhancement in properties and to understand whether the observed changes and improvements are universal for all metals or whether they depend on their specific magnetic nature.

The present work has shown that the four alloys which had been subjected to alternating magnetic field treatment exhibited increased resistance to cavitation erosion. The TEM results revealed that there was movement of dislocations in all four alloys as a result of alternating magnetic field treatment. In the case of the NAB bronze and the AA2014-T6 alloy there was also evidence of precipitation, while coalescence of iron particles was observed in 70/30 brass. The function of the magnetic field in bringing about these changes must be questioned. The most common variables that are used to describe the thermodynamic state of a material are pressure, temperature and composition. In their classic book on thermodynamics, Lewis and Randal [154] recognised the fact that other independent variables like an electric and a magnetic field can also change the thermodynamic properties of a material. A small number

of theoretical studies have been undertaken to investigate the effect of magnetic fields on phase transformations. One of the few studies involving computational phase diagram predictions was carried out by Gao et al and focused on the effect of magnetic fields on the α/ϒ phase fields in the Fe-Si system. Changes in the α/ϒ temperature transition were observed as the field strength increased. The magnetic α phase field was enlarged with increasing magnetic flux density at the expense of the paramagnetic ϒ phase. From their results, it is apparent that magnetization can have a significant effect on phase transformations and that it can favour the formation of magnetic phases at the expense of non-magnetic ones. According to Gao et al [155], there is an additional contribution to the Gibbs Free energy when an external magnetic field is applied. The total free energy change, can be presented in the form shown in Equation 8.4.

$$\Delta \boldsymbol{G} = \Delta \boldsymbol{G}_{\boldsymbol{non-magnetic}} + \Delta \boldsymbol{G}_{\boldsymbol{magnetic\ (internal)}} + \Delta \boldsymbol{G}_{\boldsymbol{magnetic\ (external)}} \qquad \text{Equation 8.4}$$

which shows an external magnetic contribution in addition to an internal magnetic contribution and a non-magnetic contribution. The application of an external magnetic field does not affect the non-magnetic and the internal magnetic contributions, but does have an effect on the external contribution which can be calculated by Equation 8.5.

$$\Delta G_{magnetic\ (external)} = -\mu \int_0^H M\, dH \qquad \text{Equation 8.5}$$

where M is the magnetisation, H is the magnetic flux density and μ is the vacuum permeability. In the present work, the application of the magnetic field to the NAB alloy has led to precipitation of the κ_{IV} phase which is based on Fe_3Al and NiAl both of which are magnetic. This additional precipitation was caused by the effect of magnetization due to the treatment. The coalescence of the magnetic iron particles in the 70/30 brass alloy is also likely to be due to a change in the thermodynamic properties of the alloy as a result of magnetization. In the case of the AA2014-T6 alloy, precipitation of GP zones and Θ'' was observed from the aluminium-copper solid solution which, at room temperature, is metastable and therefore has a small positive Gibbs Free energy in comparison to the alloy in the stable state. The

transformation of the metastable solid solution to the equilibrium Θ ($CuAl_2$) phase is kinetically extremely slow at room temperature and requires high temperatures. At room temperature, the natural precipitation of extremely fine GP zones and Θ'' takes place (from the solid solution) since the diffusion distance required for their formation is very small and thus this alloy can harden by natural ageing at room temperature. The application of the magnetic field has led to additional precipitation from the metastable aluminium-copper solid solution to form GP zones and Θ''. Being in a metastable state, the aluminium alloy would have a small positive Gibbs Free energy and the need to lower the Free energy acts as a driving force to precipitate fine GP zones and Θ''. It must be noted that the level of the alternating magnetic field that was applied during the present study was not high enough to lead to the equilibrium Θ ($CuAl_2$) phase.

The non-magnetic contribution to the Gibbs Free energy is mainly due to chemical changes; in addition, there are also smaller contributions that are related to stress (and strain) and to surface changes. All four alloys that were investigated were in the cold-worked state. As a metal is cold-worked by rolling, drawing and extrusion, its Gibbs Free energy increases by an amount which is approximately equal to the stored strain energy (with some energy lost as heat). This stored energy has been shown to reach up to about 60% of the work of the initial plastic deformation at some conditions (levels and rates of plastic strain) [133, 156]. When in the stressed/strained state, metals contain defects including dislocations that pile up at grain boundaries and contain residual stresses. The application of the alternating magnetic field provided the push for the four alloys to release their stored energy and thus reduce their Gibbs Free energy.

The present investigation has shown that the four tested alloys, irrespective of their magnetic nature, had improved resistance against cavitation erosion following the application of alternating magnetic field treatment. The observed microstructural changes involving precipitation and movement of dislocations are normally activated by heat and in the present study they were achieved by the application of and external magnetic field.

8.3.1 Simulation of AMF treatment for cavitation erosion studies

In the present study, eddy currents were induced in each sample when the polarity of the magnetic field was changed (step change). This occurred every 5 seconds during the treatment process and is likely to have led to heating of the samples. A question that therefore

needs to be addressed is whether the treatment has led to heating to such temperatures as to allow the observed microstructural changes. This was carried out by numerical modelling of the magnetic field and eddy current distributions for each sample in order to predict the level of increase of temperature during treatment. This was undertaken by employing QuickField 6 software (Tera Analysis, Svendborg, Denmark). The solution was obtained for a 2-D formulation of a transient magnetic field problem. Figure 8.9 shows a geometrical quarter model of the treatment arrangement used during numerical modelling. The physical properties of the samples and the model components used in the simulation are presented in Table 8.5.

Table 8.5. Physical properties of the materials used during modelling.

Property	EN8 Steel sample	NAB	Brass	AA2014-T6	Core (steel)	Spacer (steel)	Winding wire (copper)	Air
Conductivity, MS/m	10	2.3	13.8	23	10	10	56	0
Relative permeability	B-H curve*	1.5**	1	1	B-H curve*	B-H curve*	1	1
The magnetic flux density vs magnetic field strength (B-H) curve for steel was taken from [130] and [103]**								

The full current time variation $I(t)$, passing through every single turn of the magnetiser windings can be presented by the equation:

$$I(t) = I_0 sign\left(sin\left(\frac{2\pi t}{T}\right)\right), \qquad \text{Equation 8.6}$$

where T = 10 s is the period of time that the field acts in both directions during magnetisation. The value of I_0 was determined based on the best fitting of the calculated and registered profiles of the magnetic field for the magnetiser without a sample; the value obtained was 0.82 T (Chapter 3 Figure **3.6**b).

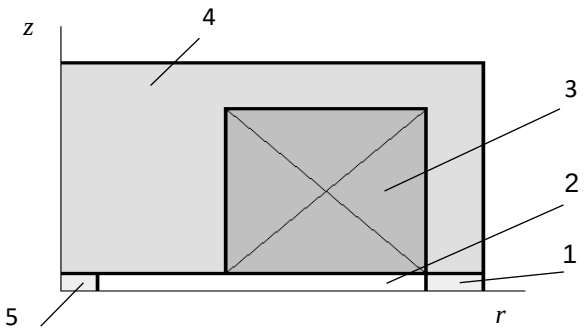

Figure 8.9. Schematic presentation of magnetiser with sample (¼ model): 1 – steel spacer, 2 – air gap; 3 – winding (consists of 70 turns), 4 – core, 5 – sample.

Numerical modelling was then fulfilled for the magnetiser with samples located at the centre as illustrated in Figure 8.10. According to the results, the EN8 steel sample was exposed to a magnetic flux density of about 2.95 T and the NAB sample to about 1.18 T as they were magnetised under the external magnetic field. The 70/30 brass and AA2014-T6 samples were exposed to a magnetic flux density of 0.82 T due to having a relative permeability of 1. Switching the polarity of the magnetic field gives a total change of magnetic flux density of 5.9 T and 2.36 T for the EN8 steel and NAB samples respectively. In the case of both the 70/30 brass and the AA2014-T6 alloy, the total change of the magnetic flux density is 1.64 T. This magnetic field variation every 5 s induces eddy currents in the samples and an example of the eddy current induced in the edge point of AA2014-T6 sample is presented in Figure 8.10a which presents the distribution of the maximum eddy currents vs. radius on a flat surface of the samples. As shown in Figure 8.10b, the maximum current density values of the resulting eddy currents at the edge of the cylindrical surface of the samples was 1.22×10^6 A/m^2, 2.92×10^6 A/m^2, 0.61×10^6 A/m^2 and 4.63×10^6 A/m^2 for EN8 steel, 70/30 brass, NAB and AA2014-T6, respectively.

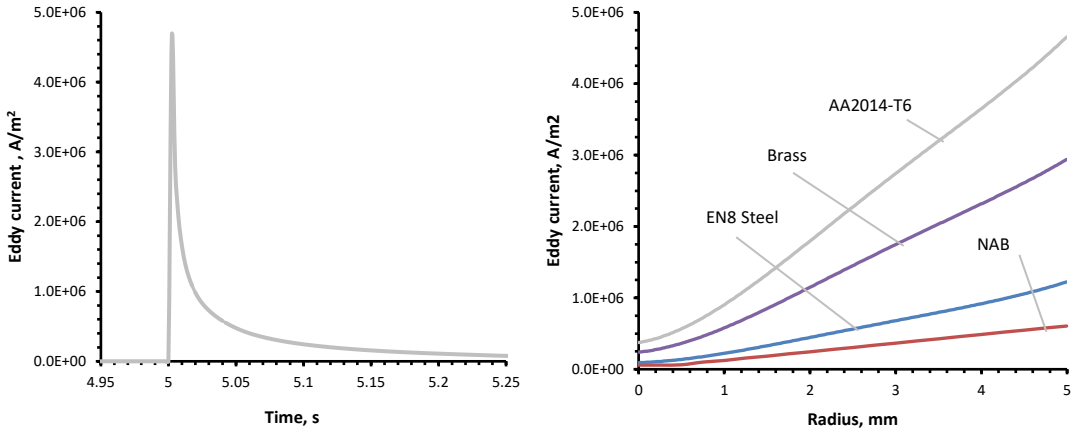

(a) (b)

Figure 8.10. Eddy current induced at the edge point of the AA2014-T6 sample (a) and distribution of maximum eddy currents vs. radius on a flat surface of samples (b).

The spacers were slightly thicker than the sample geometry (see Figure 8.9), preventing mutual attraction between the cores. The results showed that the temperature increase as a result of the eddy currents was very small (about 11.5 ˚C); such a low temperature increase is unlikely to induce the kind of changes observed, that is, movement of dislocations and to the formation of precipitates. For this reason, it can be concluded that temperature was unlikely to be a factor leading to the observed microstructural changes and that the effect was athermal.

8.3.2 Microstructural changes enhancing erosion resistance and their driving mechanisms.

In this investigation, two types of microstructural changes were detected as a result of alternating magnetic field treatment. The first one is the movement and redistribution of dislocations. All four investigated metals showed reduction of dislocation density at the grain boundaries as presented in Chapter 7 Figure 7.7 – 7.11 with high-density dislocation structures such as dislocation tangles and pile-ups annihilating and/or dispersing following the treatment. The second group of changes involve precipitation of secondary phases; in the case of NAB, there was evidence of more κ_{IV} precipitates (Figure 7.8b), while precipitation of Θ'' occurred in the AA2014-T6 samples (Chapter 7 Figure 7.10b). These precipitates are key strengthening phases in these two alloys. In addition, there was coalescence of Fe clusters in

70/30 brass (Chapter 7 Figure 7.9b). The most probable mechanism of the movement, dispersion and redistribution of dislocations away from grain boundaries is their increased mobility which was stimulated by the treatment; this led to the mutual annihilation of dislocations of opposite sign. While grain boundaries can act as typical areas of obstruction to dislocation motion, they seem to be relatively clear of dislocations after treatment. Another natural sink for dislocations is the outer free surface (boundaries) of the samples. Treatment-stimulated dislocations from below the alloy surface were observed to easily move towards the surface. The existence of this mechanism has been confirmed experimentally by Vdovin and Kasumov [157]. In a unique experiment that they conducted, an electric current was passed through a copper foil that had been placed in a TEM. When the electric current was switched on, these researchers recorded dislocation movement from the depth of the sample towards its surface where the dislocations disappeared. As the dislocations move towards the surface, the accumulation of micro-strains in the subsurface regions is likely to take place and will lead to an increase in surface compressive RS and, as a consequence, an increase in hardness [145, 158] (see Chapter 7 Table 7.1). The resulting beneficial effect of compressive RS in improving cavitation erosion resistance is well-known [159, 160]. In addition, secondary precipitation of κ_{IV} and Θ' phases in NAB and AA2014-T6 respectively also enhance the hardness and strength (see Chapter 7 Table 7.1) of these alloys and increase their resistance to cavitation erosion. A similar effect appears to have taken place by the formation of iron clusters in 70/30 brass.

In the case of aluminium AA2014 and the NAB alloy, the movement of dislocations and the increased diffusivity of elements from solid solutions (to form precipitates) as a result of the treatment were evident. The uniform precipitation and dispersion of dislocations led to a more homogeneous microstructure and more uniform properties as shown by the lower mean-square deviation for the hardness and RS measurements. This is an important effect of the AMF treatment, as it is well-established that microstructural homogenisation in metals is especially important for increased resistance against cavitation erosion [161-165]. The conclusion concerning the formation of a more homogeneous structure after processing can be drawn from the analysis of the microstructure that reveals a lower level of dislocation entanglement, reduction of dislocation pile-ups and a more uniform distribution of dislocations. In addition, in the case of EN8 steel, the MFM results show evidence of a more

uniform distribution of magnetic domains, while the mean-square deviation of the results of the microhardness measurements is lower after treatment. To ensure accuracy of the microhardness results, 180 measurements were obtained per metal alloy per condition. Metal homogeneity (uniformity of microstructure) was further estimated from the coefficient of variation of hardness (CVH). Based on the data presented in Chapter 7 Table 7.1, there was a general reduction of CVH for EN8 steel, NAB, 70/30 brass and AA2014-T6 following the treatment. This indicates a general homogenisation of metal microstructure and an improvement of resistance to cavitation erosion.

The cumulative effect of all the above-mentioned factors (formation of compressive RS, precipitation strengthening, formation of clusters of Fe impurities and increased homogeneity of metal structure) has led to higher resistance to cavitation erosion for all the treated samples. As a result, while higher levels of erosion can be observed in the samples in the untreated condition, the treated samples exhibited surface characteristics of much lower cavitation erosion damage and surface roughness (refer to Chapter 7 Figure 7.3 – 7.6). As explained above, the driving force for these changes was the need to lower the Gibbs Free energy of the samples which were initially in a stressed/strained state. Lowering Gibbs Free energy can be achieved by reducing the dislocation concentration or by precipitation hardening. In addition, the contribution of the external magnetic field has led to the precipitation of strengthening phases and to the coalescence of iron impurities in the 70/30 brass alloy.

8.3.3 Effect of induced eddy currents cavitation erosion

To determine the influence of induced eddy currents during treatment, numerical modelling was used to understand if the eddy current effect was one of the main driving forces for the improvement in the cavitation erosion behaviour. Numerical modelling has shown that eddy currents were induced at the surface of the samples with current densities ranging from 0.61×10^5 A/m^2 to 4.63×10^6 A/m^2 depending on the material and sample radius as shown in Table 8.6. The electric current itself can be considered as a parameter affecting the mechanical properties, particularly as it causes relaxation and redistribution of RS. During cyclic loading. Tensile RS at the component surface often induces crack initiation and crack propagation,

resulting in critical damage during cyclic loading. This can also be mitigated by reducing tensile RS or by inducing compressive RS on the surface. In addition to fatigue, cyclic loading can alsco occur during sliding contact wear or by cavitation erosion. The cyclic loading contributes to crack propagation in a way similar to that of fatigue. It is well known that residual stress can strongly influence fatigue behaviour. Consequently, it has also been reported that compressive residual stress can influence the sliding contact wear resistance and cavitation erosion behaviour by retarding crack initiation and crack propagation. Understanding the influence of eddy current on residual stress and dislocation behaviour is crucial for understanding if this is the main driving force for the improvement in the mechanical properties.

This influence is based on the electroplastic effect which was observed experimentally for the first time by Troitskii [166] and was later widely investigated in other studies [87, 167-170]. The observed results from the electroplastic effect were attributed to the influence of the electron wind of the current flow which props up dislocations, facilitating their movement and causing a drop in the resistance to deformation. This approach was based on the earlier theoretical work of Kravchenko who concluded that the electron flux creates an accelerating force for dislocations if the electron drift velocity exceeds the dislocation velocity. Later studies [167, 171-173] showed that the "electron wind" approach was not able to explain the observed reduction of the resistance to deformation at the electric current densities used during real experiments. The same conclusion can be derived by applying the "electron wind" approach to the present experimental work. Indeed, considering the basic relationships of the existing electrical conductivity theory , it is possible to determine the current density, i (A/m^2), the electric field intensity, E (V/m), and the electrical resistivity, ρ (Ω·m), from Equation 8.7, 8.8 and 8.9:

$$\frac{dU}{dx} = E = \rho i \qquad \text{Equation 8.7}$$

where

$$i = evn_0 \qquad \text{Equation 8.8}$$

$$\rho = 2m_e/(n_0 e^2 t_0) \qquad \text{Equation 8.9}$$

and e is the electron elementary charge that is equal to 1.602176634 x 10^{-19} Columbs, v is the velocity of electron drift (m/s), n_0 is the number of conduction electrons per volume (m^{-3}), U is the electric potential (V), m_e is the electron rest mass that is equal to 9.10956 x 10^{-31} kg, and t_0 is the mean free time between electron ionic collisions.

Based on Equation 8.7, 8.8 and 8.9, the kinetic energy of the electrons by the action of an electric field under isotropic scattering of electrons can be determined [174] as:

$$K_e = m_e v^2/2 = eE \cdot (vt_0) = \rho i(evn_0)t_0/n_0 = \rho i^2 t_0/n_0 \qquad \text{Equation 8.10}$$

At predetermined experimental conditions (for fixed i and ρ), the interaction between electrons and the crystal lattice for iron (EN8 steel), copper (70/30 brass and NAB) and aluminium (AA2014-T6) can be determined by Equation 8.7 and Equation 8.10. The increase in the kinetic energy of electrons in iron, copper and aluminium within their free path was calculated from Equation 8.10 at the respective maximum current density values that were obtained from the numerical simulation. The results are presented in Table 8.6.

Table 8.6. Current density and calculated Kinetic Energy of electrons by the action of an electric field for EN8 steel, NAB, 70/30 brass and AA2014-T6.

Alloy	EN8 steel	NAB	70/30 Brass	AA2014-T6
Current Density	1.22 x 10^6 A/m^2	0.61 x 10^6 A/m^2	2.92 x 10^6 A/m^2	4.63 x 10^6 A/m^2
Kinetic Energy	$\Delta K_{e(Fe)} \cong$ 1.01 x 10^{-20} eV	$\Delta K_{e(Cu)} \cong$ 2.29 x 10^{-20} eV	$\Delta K_{e(Cu)} \cong$ 5.24 x 10^{-19} eV	$\Delta K_{e(Al)}$ 1.05 x 10^{-19} eV

These values of ΔK_e are negligible in comparison with the change in the kinetic energy, ΔK_T, due to an increase in temperature T, by just 1°C:

$$\Delta K_T \cong kT \cong 8.61 \times 10^{-5} eV \qquad \text{Equation 8.11}$$

Where k, the Boltzmann constant, is $k = 8.617333262145 \times 10^{-5}\ eV \cdot K^{-1}$.

The alloy samples that were used in the present research had been cold-worked during manufacturing and were therefore in a strained condition. By taking a conservative estimate

that the dislocation density, n_d, is about 10^{11}/cm^2, the ratio of the total density of atoms, n, to the density of dislocations, n_d, for each alloy was calculated to be $n/n_{d(Fe)}$ = 1.94 x 10^4, $n/n_{d(Cu)}$ = 1.93 x 10^4 and $n/n_{d(Al)}$ = 2.16 x 10^4. The effective increase in the kinetic energy of atoms in dislocation cores due to electron wind can be estimated by Equation 8.12:

$$\Delta K_{ef} = n/n_d \cdot \Delta K_e \qquad \text{Equation 8.12}$$

In the case of EN8 steel, this value can be calculated as $\Delta K_{ef(Fe)} \cong$ 1.96 x 10^{-16}eV, for 70/30 brass $\Delta K_{ef(Cu)} \cong$ 1.01 x 10^{-14} eV, for NAB $\Delta K_{ef(Cu)} \cong$ 4.42 x 10^{-16}eV and for AA2014-T6 $\Delta K_{ef(Al)} \cong$ 2.26 x 10^{-15}eV. Again, these values are still negligible in terms of thermally induced atomic motion based on Equation 8.11. This means that the strength of the eddy currents is too low to induce atomic motion. From the above calculations, the direct interaction between the electron wind and dislocations is an unlikely cause of dislocation movement; it can therefore be concluded that the induced eddy currents were not the main reason for the observed microstructural changes. This conclusion can also be supported by results of other experimental research where noticeable changes in the microstructure, mechanical properties and RS of metals took place only at electric current density values exceeding 10^8 A/m^2 [157].

8.3.4 Effect of the alternating magnetic field

It must be noted that in this study, the applied treatment was carried out using a relatively "weak" magnetic field in comparison to other research by Golovin [175]. During the present investigation, the magnetic flux density, B , was 0.83T and the energy, U_{mf}, of the magnetic field was estimated using Equation 8.13 [175]:

$$U_{mf} \sim \mu_b B \approx 4.8 \times 10^{-5} eV \qquad \text{Equation 8.13}$$

where $\mu_b \approx$ 5.7883818012 x 10^{-5} eV·T^{-1} and represents the Bohr magneton. At the same time the value of the kinetic energy, ΔK_T, at 20°C (T_R = 293 K) can be estimated to be 2.5 x 10^{-2}eV from Equation 8.11. This means that the energy of the magnetic field, U_{mf}, transferred to the metal samples during the treatment is three orders of magnitude lower than the kinetic energy of motion of the metal atoms at room temperature.

Based on literature data, some authors [137, 139, 140, 175] have concluded that a weak magnetic field would trigger only limited mobility of dislocations, but further dislocation movement during treatment may occur due to the potential energy stored in the metals. Extra precipitation and coalescence of Fe impurities in the treated metals also can be the result of the triggering effect of the magnetic field on diffusional processes. In both cases, the application of the magnetic field is likely to trigger these microstructural changes for the reduction of the Gibbs Free energy. The specific mechanisms of influence of the magnetic field on metals leading to the observed changes at micro- and macro-levels will be discussed next for each metal that was used in the research.

EN8 steel. The changes in the EN8 steel microstructure following treatment can be related to the increased mobility of dislocations and to the release of stored strain energy leading to a reduction in the Gibbs Free energy. This can be see by the TEM micrographs in chapter 7 Figure **7**.**7** According to the simulation results, the steel samples were exposed to the magnetic field of a magnetic flux density of 2.95 T. This value is sufficiently high enough to achieve full magnetic saturation of the steel accompanied by displacement of the magnetic domain walls. This has led to an increase in the size of the magnetic domains oriented parallel to the field by swallowing domains that are oriented opposite to it. The result of this is the creation of a single-domain structure. Alteration of the field during the treatment is accompanied by a decrease of the field down to a zero magnetic flux, thus increasing the number of magnetic domains. Further increase of the magnetic flux density of opposite polarity will again cause the displacement of the magnetic domain walls, finally leading to the creation of a single-domain structure at the point of magnetic saturation. This process is repeated throughout the entire treatment. As soon as this is completed (at zero magnetic flux density), the spontaneous division of the magnetic residual domains will lead to their final structure (see Chapter 7 Figure 7.6a and 7.7b).

The magnetic domain walls are pinned by dislocations which form temporary barriers to their movement. However, when the magnetic flux density becomes high enough to overcome the local energy barrier at the dislocation, an abrupt displacement of the magnetic domain walls occurs and this is recorded in the form of Barkhausen noise [176]. The interaction between magnetic domain walls and dislocations can make it easier for the dislocations to overcome

barriers in the crystal lattice. Depinning of dislocations caused by magnetic domain wall displacement due to domain increase/decrease and rotation and their additional movement driven by the stored energy is commonly suggested as the main mechanism of increased dislocation mobility in the case of magnetic treatment of ferromagnetic metals [11, 82, 105, 177]. The magnetostriction of the metal volume due to the application of the magnetic field is also suggested as an extra factor triggering dislocation depinning [11, 82].

NAB, 70/30 brass and AA2014-T6. In the case of NAB bronze and the AA2014-T6 aluminium alloy, evolution of the microstructure takes place as a result of treatment; this is represented by a more uniform distribution of dislocations and significant levels of precipitation, while in the case of 70/30 brass there is evidence of coalescence of iron impurity dispersions (Chapter 7 Figure 7.8 – 7.11). These changes are accompanied by a reduction of the Gibbs Free energy. As *NAB* has soft magnetic properties, the application of an external magnetic field with a magnetic flux density B = 0.83 T causes magnetization; according to the simulation results, a magnetic flux density of 1.18 T was applied leading to magnetisation. Similar to EN8 steel as discussed above, the alternating value of the magnetic field will cause cyclic gradual magnetic saturation of the metal and build up larger magnetic domains within areas of the alloy with a higher concentration of the Fe_3Al and NiAl phases which are magnetic [178]. Following treatment, a new residual MFM domain pattern appeared (see Chapter 7 Figure 7.6c and 7.7d). Therefore, the same mechanism of dislocation depinning occurred as with EN8 steel involving the movement of magnetic domain walls due to domain increase/decrease and rotation. This action was driven by the stored energy in the as-received deformed NAB.

The model based on magnetic domain wall movement can be used to explain the unpinning of dislocations around the magnetic κ_I, κ_{II} and κ_{III} Fe_3Al and NiAl precipitates in NAB as they are relatively large in size [149]. However, the κ_{IV} precipitates which are also based on Fe_3Al exhibit substantially different behaviour as they have significantly smaller size in comparison to the other κ phases. As shown in Chapter 7 Figure 7.8b, most of them have size have a single-domain state in the absence of magnetisation and remain in this state during application of the magnetic field [151, 152]. In this state, the particles have very high coercivity and consequently during reversing of magnetisation of the κ_{IV} phase, the widest possible hysteresis loop is achieved for a particle of that composition (Fe_3Al). This means that

the external magnetic field does the greatest possible work on the metal and this work is dissipated as heat. This can lead to the unpinning of dislocations from these precipitates and to their additional motion due to the presence of stored energy (long-range stress and strain field). This heating is localized around the κ_{IV} precipitates and can enable diffusion mobility of "free" solute Fe and Al atoms that are present in the α solid solution and the retained β-phase to form more κ_{IV} precipitates.

Another mechanism advancing diffusion mobility of solute Fe, Fe_3Al nuclei and small κ_{IV} precipitates is based on dipolar interaction causing an attraction or repulsion of magnetic dipoles. The energy levels of these interactions can be compared by considering a group of Fe atoms (Fe atom clusters), Fe_3Al nuclei or κ_{IV} precipitates of the same size and magnetic moment, m. When the magnetic field is applied, the magnetic moment of the dipoles (Fe atoms, their clusters, Fe_3Al nuclei and κ_{IV} precipitates) will be aligned with the direction of the field as shown in Figure 8.11a. If the distance between two dipoles is *r*, the energy of the magnetic dipole interaction, E_D, can be expressed in this case as [179]:

$$\boldsymbol{E_D = -\frac{\mu_0 m^2}{4\pi}\frac{3cos^2\theta - 1}{r^3}} \qquad \text{Equation 8.14}$$

where μ_0 is the vacuum magnetic permeability and θ is the angle between the *y*-axis and the radius-vector r. This equation shows that the energy of the magnetic dipole interaction, E_D, depends on the relative position of the interacting dipoles, described by the geometric factor, f, where $f = \frac{3cos^2\theta - 1}{r^3}$. Calculated values of the geometric factor, f, as a function of the relative position of the dipoles are presented in Figure 8.11b.

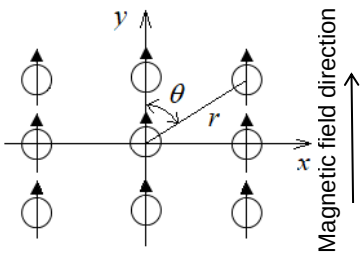

(a)

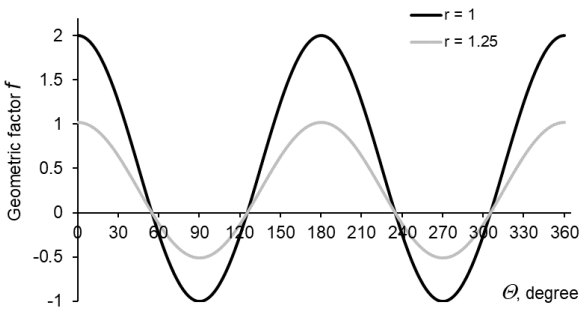

(b)

Figure 8.11. Alignment of the dipoles under a magnetic field (a); variation of the geometrical factor *f* for $0^0 \leq \theta \leq 360^0$ and for *r* = 1 and *r* = 1.25 (b).

Calculation of the geometrical factor, f, shows that the magnetic dipolar interaction energy, E_D, is negative and the dipoles are attracted to each other when two dipoles are on a line that coincides with the direction of the magnetic field. If two dipoles are oriented perpendicular to the field direction, the magnetic dipolar interaction energy, E_D, is positive and the dipoles repulse each other. Overall, the maximum energy of attraction is twice the maximum energy of repulsion. Under this condition, a higher diffusion mobility of Fe atoms, Fe atoms clusters, Fe_3Al nuclei and nuclei of κ_{IV} precipitates can contribute to the formation of a larger amount of κ_{IV} precipitates. Another source of κ_{IV} precipitates is the eutectoid transformation of the β phase to the copper-rich α-phase plus κ eutectoid and further secondary κ precipitation based on Fe_3Al and NiAl.

In the case of 70/30 brass, the migration of dislocations from grain boundaries and the coalescence of Fe impurities were observed as a result of treatment as shown in Chapter 7 Figure 7.9. As with the NAB bronze, the treatment has led to magnetization and has enhanced the presence of the ferromagnetic Fe impurities and has led to the creation of greater Fe clusters which are observed in Chapter 7 Figure 7.9b. Considering that the size of the Fe clusters is quite similar to that for the κ_{IV} precipitates in NAB, it can be suggested that these Fe clusters also have a single-domain state and their re-orientation due to the application of the external magnetic field was accompanied by release of energy. It is obvious that the increased diffusion of Fe atoms together with the re-orientation of the Fe impurity clusters can violate the state of the dislocation pins and cause unpinning of dislocations which then moved under the action of long-range stress and strain field stored in the material (in other words there was release of the stored energy). This movement leads to mutual annihilation of dislocations and to their re-arrangement as shown in Chapter 7 Figure 7.9b. The aluminium 2014-T6 alloy also experienced significant clearance of dislocations from grain boundaries and precipitation of the Θ'' phase due to application of the alternating magnetic field treatment (Chapter 7 Figure 7.10). The aforementioned mechanisms explaining the observed effects of the treatment are not applicable since this alloy has no magnetic phases in its composition. Even if Fe is present as an impurity, it exists mainly in the form of Al_2Fe and Al_3Fe secondary phases which are paramagnetic [180]. It should be noted that Al itself also is paramagnetic.

At the same time the paramagnetism of the main constituent phases can be a key point to understanding the effect of the magnetic field on the AA2014-T6 alloy in the present research. The most adequate model available to explain the observed changes in AA2014-T6 as caused by the magnetic field is presented in the work of Molotov and co-workers [137, 139]. The model assumes that the magnetic field changes the spin multiplicity of radical pairs formed by dangling bonds of dislocation nuclei and paramagnetic obstacles. As a result, the likelihood of depinning increases. According to Molotov and his co-workers , a strong bond between atoms exists only in the ground singlet (*S*) state where the electron spins are antiparallel. In the excited triplet (*T*) state with parallel spins, the coupling is weaker or even absent. In the presence of a magnetic field, the *S*-to-*T* transition becomes possible and, as a result, the number of weaker *T* states in dislocation-obstacle systems (like dislocation-Al_3Fe pins or dislocation-forest dislocations) increases. This, in turn, makes possible the depinning of dislocations and their further annihilation and redistribution associated with their movement due to the release of stored energy (namely due to the long-range stress and strain field originally accumulated within the metal).

As for treatment-induced extra precipitation of the Θ'' phase, it should be mentioned that in the AA2014 aluminium alloy after the T6 temper there is still a high level of solute Cu in the supersaturated solid solution (SSS). As above, it can be suggested that the magnetic field also increases the breakup of weaker *T* states in the Al- “free” solute Cu system increasing the diffusion mobility of Cu atoms which leads to secondary ageing accompanied by additional precipitation of GP-zones and further growth of existing and newly formed GP-zones to the Θ'' phase according to the precipitation sequence:

$$SSS \rightarrow GP\ zones \rightarrow \theta'' \qquad \text{Equation 8.15}$$

It must also be noted that the diffusion distance required to precipitate GP zones and Θ'' is so small that this is possible at room temperature by natural ageing. The application of the external magnetic field was able to supply additional energy to enhance the precipitation process.

The models that were considered in this discussion on the influence of the magnetic field on metals are not complete and exhaustive. It is clear that the influence of the magnetic field is more complex and may involve some other factors and mechanisms and this is the reason why complete understanding of this research topic is still a challenge. At the same time, it can be assumed that the main role of the magnetic field during the treatment is to trigger the transition from a metastable state of metal to a more stable one by a decrease in the Gibbs Free energy. In order to further progress and commercialise this type of treatment, it is vital to develop equilibrium phase diagrams as a function of magnetic flux density. In addition, very little research has been conducted with regard to the kinetics of the treatment. Taking into account the benefits of this treatment, for example, efficiency, simplicity and low energy consumption, it can be concluded that further research is necessary to understand the mechanisms that lead to its effects.

8.3.5 Summary of Cavitation Erosion studies

In Chapter 8, the effect of the alternating magnetic field treatment (AMF) on the cavitation erosion resistance of EN8 steel, NAB, 70/30 brass and 2014-T6 aluminium alloy was discussed through both numerical and experimental analyses. It can be determined that the effect of the treatment has a non-thermal nature and leads to significant improvement of the cavitation erosion resistance of all the investigated metals regardless of their magnetic nature (magnetic, diamagnetic and paramagnetic).

TEM observation found two major groups of microstructural changes in the investigated metals as a result of the treatment: (i) redistribution of dislocations, dispersion of dislocation tangles and pile-ups and reduction of the dislocation density near grain boundaries; and (ii) extra precipitation of secondary phases in NAB (κ_{IV} phase) and AA2014-T6 (theta double prime Θ'') as well as formation of greater iron clusters in 70/30 brass (these are key strengthening phases in these alloys).

Due to the increased mobility of dislocations and additional precipitation and diffusion caused by the AMF treatment, a higher level of residual compressive stresses, increased hardness and

higher homogenisation of the metal structure were achieved resulting in the improvement of the cavitation erosion resistance of all the investigated metals.

9 Conclusion and future work

9.1 Conclusions

A comprehensive investigation has been carried out to investigate the effects of alternating magnetic field treatment on the fatigue, friction and cavitation erosion properties of metallic alloys. This low-cost and low-energy treatment was developed by the author of this thesis at the University of Hertfordshire. The investigation of an alternating magnetic field treatment on the fatigue life of EN8 steel and AA2014-T6 alloy has led to a substantial increase in the fatigue endurance for both alloys. Furthermore, a minor increase in other mechanical properties was achieved. The experimental study on the effects of alternating magnetic field treatment on the friction and wear resistance of EN8 steel, NAB and AA2014-T6 has led to a reduction of the coefficient of friction, wear scar width and specific wear rate for the treated conditions. In addition, micro- and nano-hardness measurements showed an increase after treatment. The loading-unloading results from nanoindentation have shown a small increase in the elastic recovery parameter following treatment for all alloys. This implied that the contact between the pin and the treated sample became less plastic and more elastic leading to lower abrasion wear and to a more stable COF resulting in a lower wear rate. The study on the effect of the alternating magnetic field treatment on the cavitation erosion resistance of EN8 steel, NAB, 70/30 brass and AA2014-T6 have shown improvements following the treatment.

The effect of the treatment in all studies can be attributed to the non-thermal nature of the treatment that leads to significant improvement in the fatigue, wear/friction and erosion resistance of all the investigated metals regardless of their magnetic nature (magnetic, diamagnetic and paramagnetic). Based on the results from each study, the microstructural changes can be broken down into two main groups, : (i) redistribution of dislocations, dispersion of dislocation tangles and pile-ups, reduction of dislocation density near grain boundaries; and, (ii) extra precipitation of secondary phases in NAB (κ_{IV} phase) and AA2014-T6 (Θ'') as well as formation of greater iron clusters in 70/30 brass.

Due to the increased mobility of dislocations which migrate towards the surface as a result of the AMF treatment, a higher level of residual compressive stresses, increased hardness and

higher homogenisation of the metal structure were achieved leading to improvement of the fatigue, friction/wear and cavitation erosion resistance of all the investigated metals. In the case of the NAB and AA2014-T6 alloys, additional precipitation took place to increase hardness and improve resistance against fatigue, friction/wear and cavitation erosion.
The mechanisms of increased mobility and precipitation after magnetic field treatment for the alloys were different:

- the main mechanism for EN8 steel is related to magnetic domain wall movement as well as magnetostriction;
- in the NAB alloy, dislocation mobility and extra precipitation of the κ_{IV} phase can be the result of magnetic domain wall movement, cyclic re-magnetization of κ_{IV} precipitates and their dipolar interaction;
- in 70/30 brass, dislocation mobility and formation of the Fe impurity clusters can be the result of cyclic re-magnetisation of Fe impurities and their dipolar interaction;
- in the AA2014-T6 alloy, dislocation mobility and extra precipitation of the theta double prime Θ'' phase can be due to change of the multiplicity of the radical pairs formed by cores of intersecting dislocations as well as dislocation cores and obstacles. This can also facilitate diffusion mobility of “free” solute Cu atoms from super saturated solution of aluminium matrix.

It is assumed that the main role of the alternating magnetic field during the treatment in the present investigation is to trigger the transition from a metastable state to a more stable (or less metastable) one, accompanied by a decrease in strain energy originally stored in the metals causing increase mobility of dislocations and extra precipitation and diffusivity.

9.2 Future Work

The studies investigated in this PhD revealed some problems that remain to be solved and also it identified new problems:

- In Chapter 5, the investigation of alternating magnetic field treatment on the fatigue resistance has been shown to improve the fatigue life of AA2014-T6 and EN8 Steel. To reinforce this research area, different treatment techniques such as pulsed magnetic field (PMF) treatment and permanent magnetic field treatment can also be investigated. Furthermore, different types of alloys including titanium alloys can be investigated. Lastly, an investigation to examine whether the use of magnetic field treatment in the high-cycle fatigue regime can help promote this area of research.

- Chapter 6 investigated the effects of alternating magnetic field treatment on the friction resistance of EN8 steel, AA2014-T6 and NAB. To strengthen this research different types of treatment techniques and parameters such as pulsed magnetic field (PMF) treatment and permanent magnetic field treatment can also be investigated. Other types of materials such as titanium and bearing steel alloys can also be investigated.

- Chapter 7 investigated the effects of alternating magnetic field treatment on NAB, AA2014, EN8 steel and 70/30 brass alloys. To further enhance this area, different types of treatment techniques and parameters such as pulsed magnetic field (PMF) treatment and static magnetic field treatment can also be investigated. In addition, further investigation to study the effect of this treatment on marine alloys should be investigated. Further investigation of the effect of magnetic field treatment on cavitation erosion-corrosion may generate more knowledge in this research area. Although this research provides important results and insights on why the AMF treatment increases the mobility of dislocations and promote precipitation of phases (and hence improves cavitation erosion resistance), further research is still needed to fully understand the mechanisms of the influence of the magnetic field on structural metals.

- The promotion of magnetic precipitates supports earlier theoretical work that suggests that increasing the magnetic flux density can extend the size of the equilibrium phase field of magnetic phases. In order for this technique to be developed and used commercially, it is necessary for more equilibrium phase diagrams to be developed as a function of magnetic flux density. Until this is done, it will not be possible to drive changes to equilibrium.

References

1. Nussbaumer, A., L. Borges, and L. Davaine, *Fatigue Design of Steel and Composite Structures : Eurocode 3: Design of Steel Structures, Part 1-9 Fatigue; Eurocode 4: Design of Composite Steel and Concrete Structures*. Vol. 1. 2012, Hoboken: Ernst & Sohn.
2. Suryanarayana, C., *Experimental techniques in materials and mechanics*. 2011: Crc Press.
3. Bao-Tong, L., Q. Sheng-Ru, and S. Xiao-Yan, *Exploration on repairing fatigue damage of steel specimens with magnetic treatment.* Scripta Materialia, 1999. **40**(7): p. 767-771.
4. Tang, Y., et al., *Restoration of fatigue damage in stainless steel by high-density electric current.* International Journal of Fatigue, 2013. **56**: p. 69-74.
5. Yan, X., D. Yang, and X. Liu, *Influence of heat treatment on the fatigue life of a laser-welded NiTi alloy wire.* Materials Characterization, 2007. **58**(3): p. 262-266.
6. Conrad, H., et al., *Effect of electric current pulses on fatigue characteristics of polycrystalline copper.* Materials Science and Engineering: A, 1991. **145**(1): p. 1-12.
7. Stepanov, G. and A. Babutskii, *Effect of a high-density current pulse on the fatigue life of a steel specimen with a stress raiser.* Strength of materials, 1995. **27**(5-6): p. 300-303.
8. Bose, M., *Effect of saturated magnetic field on fatigue life of carbon steel.* physica status solidi (a), 1984. **86**(2): p. 649-654.
9. Kuphaldt, T.R., *Lessons In Electric Circuits, Volume I–DC.* Vol. Fifth Edition. Open Book Project, 2006.
10. Babutskyi, A., A. Chrysanthou, and C. Zhao, *Effect of pulsed magnetic field pre-treatment of AISI 52100 steel on the coefficient of sliding friction and wear in pin-on-disk tests.* Friction, 2014. **2**(4): p. 310-316.
11. Tang, G., et al., *Effect of a pulsed magnetic treatment on the dislocation substructure of a commercial high strength steel.* Materials Science and Engineering: A, 2005. **398**(1–2): p. 108-112.
12. Tang, F., et al., *Research on residual stress reduction by a low frequency alternating magnetic field.* Journal of Materials Processing Technology, 1998. **74**(1–3): p. 255-258.

13. Zhao, Y., et al., *Effect of a Current pulse on the thermal fatigue behavior of cast hot work die steel.* ISIJ international, 2005. **45**(3): p. 410-412.
14. Bataineh, O., B. Klamecki, and B.G. Koepke, *Effect of pulsed magnetic treatment on drill wear.* Journal of Materials Processing Technology, 2003. **134**(2): p. 190-196.
15. Hosoi, A., T. Nagahama, and Y. Ju, *Fatigue crack healing by a controlled high density electric current field.* Materials Science and Engineering: A, 2012. **533**: p. 38-42.
16. Fahmy, Y., et al., *Effects of a Pulsed Magnetic Treatment on the Fatigue of Low Carbon Steel.* Scripta Materialia, 1998. **38**(9): p. 1355-1357.
17. Liu, L.H., L.J. Li, and Q.J. Zhai. *Microstructure Evolution and Grain Boundary Characteristics of Oriented Silicon Steel During Primary Recrystallization in a Pulsed Magnetic Field*. in *Advanced Materials Research*. 2013. Trans Tech Publ.
18. Lin, H., et al., *Effects of pulse current stimulation on the thermal fatigue crack propagation behavior of CHWD steel.* Materials Science and Engineering: A, 2008. **478**(1-2): p. 93-100.
19. Karpenko, G., et al. *Influence of an electric current upon the low-cycle fatigue of steel*. in *Sov Phys Dokl*. 1976.
20. Sosnin, O., et al., *Control of austenite steel fatigue strength.* International journal of fatigue, 2005. **27**(10-12): p. 1186-1191.
21. Hosoi, A., et al., *Quantitative evaluation of the displacement distribution and stress intensity factor of fatigue cracks healed by a controlled high-density electric current field.* Fatigue & Fracture of Engineering Materials & Structures, 2014. **37**(9): p. 1025-1033.
22. Levitin, V. and S. Loskutov, *The effect of a current pulse on the fatigue of titanium alloy.* Solid state communications, 2004. **131**(3-4): p. 181-183.
23. Konovalov, S., et al. *Increase in Reliability of Metal Articles with Impulse Current Effect*. in *MATEC Web of Conferences*. 2016. EDP Sciences.
24. Jung, J., et al., *Effect of pulsed electric current on the growth behavior of fatigue crack in Al alloy.* Procedia Structural Integrity, 2016. **2**: p. 2989-2993.
25. Mohin, M., et al., *Effect of Electromagnetic Treatment on Fatigue Resistance of 2011 Aluminum Alloy.* Journal of Multiscale Modelling, 2016. **7**(03): p. 1650004.
26. Garrison Jr, W., *Ultrahigh-strength steels for aerospace applications.* JOM, 1990. **42**(5): p. 20-24.

27. Nichipuruk, A., et al., *The effect of the dislocation structure produced by plastic deformation on the magnetic and magneto-elastic properties of iron and low-carbon steel.* Physics of metals and metallography, 1992. **74**(6): p. 593-597.
28. Klamecki, B.E. *Effects of Pulsed Magnetic Treatment on Mechanical Characteristics of Manufactured Parts*. in *ASME 2006 International Manufacturing Science and Engineering Conference*. 2006. American Society of Mechanical Engineers.
29. Cai, Z., et al., *Magnetostriction varieties and stress relief caused by pulsed magnetic field.* Frontiers of Mechanical Engineering, 2011. **6**(3): p. 354-358.
30. Konovalov, S., et al., *Evolution of dislocation substructures in fatigue loaded and failed stainless steel with the intermediate electropulsing treatment.* Materials Science and Engineering: A, 2010. **527**(12): p. 3040-3043.
31. Yang, C., et al., *Healing of fatigue crack in 1045 steel by using eddy current treatment.* Materials, 2016. **9**(8): p. 641.
32. Bhat, I., M. Muju, and P. Mazumdar, *Possible effects of magnetic fields in fatigue.* International journal of fatigue, 1993. **15**(3): p. 193-197.
33. Hosoi, A., T. Kishi, and Y. Ju. *Healing of fatigue crack treated with surface activated pre-coating method by controlling high density electric current*. in *ICF13*. 2013.
34. Shiozawa, K., et al., *Transition of fatigue failure mode of Ni–Cr–Mo low-alloy steel in very high cycle regime.* International Journal of Fatigue, 2010. **32**(3): p. 541-550.
35. Pook, L.P., *Metal fatigue: what it is, why it matters Solid mechanics and its applications v. 145*. 2007: Springer Verlag.
36. Imam, M.A., R. Srinivasan, and T.S. Srivatsan, *Fatigue of Materials III: Advances and Emergences in Understanding*. Vol. 1. 2014, US: John Wiley & Sons Inc.
37. Newman, J.C., et al., *Fatigue Crack Growth Thresholds, Endurance Limits, and Design*. 2000: ASTM.
38. Callister, W.D. and D.G. Rethwisch, *Materials science and engineering: an introduction*. 2018: Wiley New York.
39. Hertzberg, R.W., *Deformation and fracture mechanics of engineering materials.* 1989.
40. Sosnin, O., et al., *RESTORATION OF STEEL RESOURCE IN TIME OF LOW-CYCLES FATIGUE AFTER TREATING BY CURRENT IMPULES.*
41. Forrest, P.G., *Fatigue of Metals*. 2013, Burlington: Pergamon.

42. Kumar, P. and K. Prashant, *Elements of fracture mechanics*. 2009: Tata McGraw-Hill Education.
43. Wulpi, D., *Understanding How Components Fail, American Society for Metals.* Metals Park, OH, 1985.
44. Hamrock, B.J., S.R. Schmid, and B.O. Jacobson, *Fundamentals of fluid film lubrication*. 2004: CRC press.
45. Khonsari, M.M. and E.R. Booser, *Applied tribology: bearing design and lubrication*. 2017: John Wiley & Sons.
46. Burwell Jr, J.T., *Survey of possible wear mechanisms.* Wear, 1957. **1**(2): p. 119-141.
47. Ludema, K.C. and L. Ajayi, *Friction, wear, lubrication: a textbook in tribology*. 2018: CRC press.
48. Hutchings, I. and P. Shipway, *Tribology: friction and wear of engineering materials*. 2017: Butterworth-Heinemann.
49. Rabinowicz, E., *The least wear.* Wear, 1984. **100**(1-3): p. 533-541.
50. Stachowiak, G. and A.W. Batchelor, *Engineering tribology*. 2013: Butterworth-Heinemann.
51. Bhushan, B., *Introduction to tribology*. 2013: John Wiley & Sons.
52. Sin, H., N. Saka, and N. Suh, *Abrasive wear mechanisms and the grit size effect.* Wear, 1979. **55**(1): p. 163-190.
53. Hokkirigawa, K., K. Kato, and Z. Li, *The effect of hardness on the transition of the abrasive wear mechanism of steels.* Wear, 1988. **123**(2): p. 241-251.
54. Bakshi, S.D., P. Shipway, and H. Bhadeshia, *Three-body abrasive wear of fine pearlite, nanostructured bainite and martensite.* Wear, 2013. **308**(1-2): p. 46-53.
55. John, A., et al., *Stress Analysis of Polyoxymethylene which Leads to Wear in Pin on Disc Configuration using Finite Element Method.* International Journal of Research in Advent Technology, 2014. **2**(4): p. 305-310.
56. Vingsbo, O., *Wear and wear mechanisms.* Wear of Materials, 1979: p. 620-635.
57. Szolwinski, M.P. and T.N. Farris, *Mechanics of fretting fatigue crack formation.* Wear, 1996. **198**(1-2): p. 93-107.
58. Stachowiak, G. and A. Batchelor, *Engineering Tribology, Elsevier*. 2005, Butterworth-Heinemann, Burlington, Mass, USA.

59. Davis, J.R., *Surface engineering for corrosion and wear resistance*. 2001: ASM international.
60. Ghose, J., *Basic ship propulsion*. 2004: Allied publishers.
61. Totten, G.E., et al., *Hydraulic system cavitation: A review.* SAE transactions, 1998: p. 368-380.
62. Brennen, C.E., *Bubble dynamics, damage and noise*. 1994, Chapter.
63. Knapp, R., J. Daily, and F. Hammit, *Cavitation McGraw-Hill.* New York, 1970. **2**.
64. Garcia, R. and F.G. Hammitt, *Cavitation damage and correlations with material and fluid properties.* 1967.
65. He, J.-G. and F. Hammitt, *Comparison of cavitation erosion test results from venturi and vibratory facilities.* Wear, 1982. **76**(3): p. 269-292.
66. Jayaprakash, A., et al., *Scaling study of cavitation pitting from cavitating jets and ultrasonic horns.* Wear, 2012. **296**(1): p. 619-629.
67. Hansson, I. and K. Morch. *Comparison of the initial stage of vibratory and flow cavitation erosion*. in *International Conference on Erosion by Liquid and Solid Impact, 5 th, Cambridge, England*. 1979.
68. Chahine, G.L., J.-P. Franc, and A. Karimi, *Laboratory Testing Methods of Cavitation Erosion*, in *Advanced Experimental and Numerical Techniques for Cavitation Erosion Prediction*, K.-H. Kim, et al., Editors. 2014, Springer Netherlands: Dordrecht. p. 21-35.
69. Yu-Kang, Z. and F. Hammitt, *Cavitation erosion incubation period.* Wear, 1983. **86**(2): p. 299-313.
70. Fitch, E., *Cavitation wear in hydraulic systems.* Practicing Oil Analysis (9/2002, 2002.
71. Billet, M.L. *The specialist committee on cavitation erosion on propellers and appendages on high powered/high speed ships. Final report and recommendations to the 24th ITTC*. in *Proceedings of the 24th international towing tank conference*. 2005.
72. Samson, A., *Technical information: cavitation in control valves.* Samson AG, Frankfurt, Germany, 2003.
73. Çelik, A., et al., *Effect of magnetic treatment on fatigue life of AISI 4140 steel.* Materials & design, 2005. **26**(8): p. 700-704.
74. Tang, Y., et al., *Effect of high-density electric current on the microstructure and fatigue crack initiation of stainless steel.* Materials Transactions, 2013. **54**(11): p. 2085-2092.

75. Sosnin, O., et al., *The structural-phase state changes under the pulse current influence on the fatigue loaded steel.* International Journal of Fatigue, 2005. **27**(10-12): p. 1221-1226.

76. Hosoi, A., T. Kishi, and Y. Ju, *Healing of fatigue crack by high-density electropulsing in austenitic stainless steel treated with the surface-activated pre-coating.* Materials, 2013. **6**(9): p. 4213-4225.

77. Cao, W.d. and H. Conrad, *On the effect of persistent slip band (PSB) parameters on fatigue life.* Fatigue & Fracture of Engineering Materials & Structures, 1992. **15**(6): p. 573-583.

78. H. Conrad, J.W., A. F. Sprecher, Wei-di Cao and X. P. Lu, *Effect of High Density Electric Current Pulses on the Fatigue of Cu.* Materials Science and Engineering A 1991(45): p. 1-12.

79. Xi, X., Y. Xia, and Y. Hu, *The Effects of Magnetic Treatment on the Tribological Behavior of AISI 1045 Steel under Lubricated Conditions.* Tribology Transactions, 2018. **61**(4): p. 671-682.

80. Lu, A.L., et al., *Research on residual-stress reduction by strong pulsed magnetic treatment.* Journal of Materials Processing Technology, 1998. **74**(1–3): p. 259-262.

81. Tang, F., et al., *Effect of magnetic treatment on magnetostrictive behaviour of HT70 steel.* Materials Science and Engineering: A, 1998. **248**(1–2): p. 98-100.

82. Klamecki, B.E., *Residual stress reduction by pulsed magnetic treatment.* Journal of Materials Processing Technology, 2003. **141**(3): p. 385-394.

83. Cai, z. and X. Huang, *Residual stress reduction by combined treatment of pulsed magnetic field and pulsed current.* Materials Science and Engineering: A, 2011. **528**(19–20): p. 6287-6292.

84. Mohin, M.A., et al., *Effect of Electromagnetic Treatment on Fatigue Resistance of 2011 Aluminum Alloy.* Journal of Multiscale Modelling, 2016. **07**(03): p. 1650004.

85. Zhipeng, C., et al., *Plastic deformation caused by pulsed magnetic treatment of mid-carbon steel.* Materials Science and Engineering: A, 2007. **458**(1–2): p. 262-267.

86. Alshits, V., et al., *Magnetoplastic effect: basic properties and physical mechanisms.* Crystallography Reports, 2003. **48**(5): p. 768-795.

87. Conrad, H., *Electroplasticity in metals and ceramics.* Materials Science and Engineering: A, 2000. **287**(2): p. 276-287.

88. Erber, T., et al., *Piezomagnetism and fatigue.* Journal of Physics D: Applied Physics, 1997. **30**(20): p. 2818.

89. Benitez Velez, S., *The effect of residual magnetic field on the fatigue crack propagation of AerMet 100 alloy steel*. 1997, University of Puerto Rico, Mayaguez Campus.

90. Yetim, A., et al., *The effect of magnetic field on the wear properties of a ferromagnetic steel.* Wear, 2013. **301**(1-2): p. 636-640.

91. Babutskyi, A., et al., *Effect of pulsed magnetic treatment on the corrosion of titanium.* Materials Science and Technology, 2017. **33**(12): p. 1461-1472.

92. Zhipeng, C., et al., *Orientation effects in pulsed magnetic field treatment.* Materials Science and Engineering: A, 2005. **398**(1): p. 344-348.

93. *SM1090 Rotating Fatigue Machine User Guide.* TecQuipment Ltd.

94. Astm, G., *99–95a Standard Test Method for Wear Testing with a Pin-on-Disk Apparatus.* ASTM International, 2000.

95. Standard, A., *G32-10, Standard test method for cavitation erosion using vibratory apparatus.* Annual Book of ASTM Standards, 1992. **3**.

96. Cseh, D. and V. Mertinger, *X-Ray Diffraction Measurements of Residual Stress Induced by Surface Compressing Methods*. Vol. 729. 2012. 199-204.

97. Oyen, M.L. and R.F. Cook, *A practical guide for analysis of nanoindentation data.* Journal of the mechanical behavior of biomedical materials, 2009. **2**(4): p. 396-407.

98. Asm.matweb.com, *ASM Material Data Sheet.*

99. Prabhu, T.R., *Effects of ageing time on the mechanical and conductivity properties for various round bar diameters of AA 2219 Al alloy.* Engineering Science and Technology, an International Journal, 2017. **20**(1): p. 133-142.

100. Pakiela, Z., et al. *Mechanical properties and electrical conductivity of Al 6101 and 6201 alloys processed by hydro-extrusion*. in *IOP Conference Series: Materials Science and Engineering*. 2014. IOP Publishing.

101. Salazar-Guapuriche, M.A., et al. *Correlation of strength with hardness and electrical conductivity for aluminium alloy 7010*. in *Materials science forum*. 2006. Trans Tech Publ.

102. Rosen, M., et al., *The aging process in aluminum alloy 2024 studied by means of eddy currents.* Materials Science and Engineering, 1982. **53**(2): p. 191-198.

103. Richardson, I., *Guide to nickel aluminium bronze for engineers*. 2016: Copper Development Association.

104. Akram, S., et al., *Effect of Alternating Magnetic Field on the Fatigue Behaviour of EN8 Steel and 2014-T6 Aluminium Alloy.* Metals, 2019. **9**(9): p. 984.

105. Çelik, A., et al., *Effect of magnetic treatment on fatigue life of AISI 4140 steel.* Materials & Design, 2005. **26**(8): p. 700-704.

106. Zhou, Y., et al., *Crack healing in a steel by using electropulsing technique.* Materials Letters, 2004. **58**(11): p. 1732-1736.

107. Yizhou, Z., et al., *The healing of quenched crack in 1045 steel under electropulsing.* Journal of Materials Research, 2001. **16**(1): p. 17-19.

108. Babutskyi, A., et al., *Effect of electropulsing on the fatigue resistance of aluminium alloy 2014-T6.* Materials Science and Engineering: A, 2020. **772**: p. 138679.

109. Bhat, I.K., M.K. Muju, and P.K. Mazumdar, *Possible effects of magnetic fields in fatigue.* International Journal of Fatigue, 1993. **15**(3): p. 193-197.

110. Nakajima, M., et al., *Effect of solution treatment after nitriding on fatigue properties in type 304 stainless steel.* International Journal of Fatigue, 2014. **68**: p. 103-110.

111. Nie, B., et al., *Very high cycle fatigue behavior of shot-peened 3Cr13 high strength spring steel.* Materials & Design, 2013. **50**: p. 503-508.

112. Liu, Z., et al., *On the fatigue behavior of low-temperature gaseous carburized 316L austenitic stainless steel: Experimental analysis and predictive approach.* Materials Science and Engineering: A, 2020. **793**: p. 139651.

113. Faillace, E. and C. I-Wei, *The effect of a strong magnetic field on age-hardening of iron-chromium alloys.* Journal of Nuclear Materials, 1985. **133-134**: p. 343-346.

114. Song, Y. and L. Hua, *Mechanism of Residual Stress Reduction in Low Alloy Steel by a Low Frequency Alternating Magnetic Treatment.* Journal of Materials Science & Technology, 2012. **28**(9): p. 803-808.

115. Xie, C., et al., *Microstructure and mechanical properties of robot cold metal transfer Al5. 5Zn2. 5Mg2. 2Cu aluminium alloy joints.* Journal of Materials Processing Technology, 2018.

116. Dudrová, E. and M. Kabátová, *Fractography of sintered iron and steels.* Powder Metallurgy Progress, 2008. **8**(2): p. 59-75.

117. Moeser, M., *Fractography with the SEM (failure analysis)*. 2007.

118. Zhou, J., et al., *Tensile Properties and Microstructures of a 2024-T351 Aluminum Alloy Subjected to Cryogenic Treatment.* Metals, 2016. **6**(11): p. 279.

119. Li, G.-R., et al., *Influence of a high pulsed magnetic field on the tensile properties and phase transition of 7055 aluminum alloy.* Materials Research Express, 2016. **3**(10): p. 106507.

120. Zhang, G., et al., *Double-stage hardening behavior and fracture characteristics of a heavily alloyed Al–Si piston alloy during low-cycle fatigue loading.* Materials Science and Engineering: A, 2013. **561**: p. 26-33.

121. Borisova, E.A. and V.V. Zelinskiy, *On the Mechanism of Ferromagnetic Materials Wear Reduction.* Procedia Engineering, 2015. **129**: p. 111-115.

122. Bajwa, R., et al., *Wear and Friction Properties of Electrodeposited Ni-Based Coatings Subject to Nano-enhanced Lubricant and Composite Coating.* Acta Metallurgica Sinica (English Letters), 2016. **29**(10): p. 902-910.

123. Gao, F.M., et al., *In situ observation of the magnetic domain in the process of ferroalloy friction.* Tribology International, 2016. **97**: p. 371-378.

124. Herbert, E.G., *The Hardening of Metals by Rotating Magnetic Fields.* Proceedings of the Royal Society of London. Series A, Containing Papers of a Mathematical and Physical Character, 1931. **130**(814): p. 514-523.

125. Babutskii, A.I., A. Chrysanthou, and J. Ioannou, *Effect of pulsed electric current treatment on corrosion of structural metals.* Strength of Materials, 2009. **41**(4): p. 387-391.

126. Ma, L., et al., *An investigation on the mechanical property changing mechanism of high speed steel by pulsed magnetic treatment.* Materials Science and Engineering: A, 2014. **609**: p. 16-25.

127. Qin, R.S., E.I. Samuel, and A. Bhowmik, *Electropulse-induced cementite nanoparticle formation in deformed pearlitic steels.* Journal of Materials Science, 2011. **46**(9): p. 2838-2842.

128. Levitin, V.V. and S.V. Loskutov, *The effect of a current pulse on the fatigue of titanium alloy.* Solid State Communications, 2004. **131**(3–4): p. 181-183.

129. Shimatani, Y., et al., *The effect of the residual stresses generated by surface finishing methods on the very high cycle fatigue behavior of matrix HSS.* International Journal of Fatigue, 2011. **33**(2): p. 122-131.

130. Magweb, *Free BH Curves - Magweb.* Magweb.

131. Baranov, Y.V., et al., *Physical bases of electric-pulse and electroplastic treatments and new materials.* Chap, 2001. **1**: p. 56-77.

132. Troitskly OA, S.V., Sokolov NV, Ryzhkov VG, Dubov Yu. S.(Moscow), *Some magnetically hard steels are used for magnetic recording of sound and electrical signals (Ref. 1). There is reason to assume that electroplastic drawing would have a beneficial effect on the properties of these steels (Refs. 2-4).* Russian Metallurgy, 1980.

133. Oliferuk, W., S.P. Gadaj, and M.W. Grabski, *Energy storage during the tensile deformation of armco iron and austenitic steel.* Materials science and engineering, 1985. **70**: p. 131-141.

134. Hayashi, S., S. Takahashi, and M. Yamamoto, *Plastic deformation of nickel single crystals in an alternating magnetic field.* Journal of the Physical Society of Japan, 1968. **25**(3): p. 910-910.

135. Hayashi, S., S. Takahashi, and M. Yamamoto, *Magneto-plastic effect in nickel single crystals.* Journal of the Physical Society of Japan, 1971. **30**(2): p. 381-387.

136. Hayashi, S., *Magneto-plastic effect in nickel and nickel-cobalt alloy single crystals.* Journal of the Physical Society of Japan, 1972. **32**(4): p. 949-957.

137. Molotskii, M., *Possible mechanism of the magnetoplastic effect.* Soviet physics. Solid state, 1991. **33**(10): p. 1760-1761.

138. Molotskii, M., *Negative magnetoplastic effect in nonmagnetic crystals.* Physics of the solid state, 1993. **35**: p. 5-7.

139. Molotskii, M. and V. Fleurov, *Spin effects in plasticity.* Physical review letters, 1997. **78**(14): p. 2779.

140. Molotskii, M.I., *Theoretical basis for electro-and magnetoplasticity.* Materials Science and Engineering: A, 2000. **287**(2): p. 248-258.

141. Yan, W., et al., *Effect of surface work hardening on wear behavior of Hadfield steel.* Materials Science and Engineering: A, 2007. **460-461**: p. 542-549.

142. Fridrici, V., S. Fouvry, and P. Kapsa, *Effect of shot peening on the fretting wear of Ti–6Al–4V.* Wear, 2001. **250**(1): p. 642-649.

143. Mitrovic, S., et al., *Friction and wear behavior of shot peened surfaces of 36CrNiMo4 and 36NiCrMo16 alloyed steels under dry and lubricated contact conditions.* Applied Surface Science, 2014. **290**: p. 223-232.

144. Oshida, Y., *Chapter 11 - Surface Modifications*, in *Bioscience and Bioengineering of Titanium Materials*, Y. Oshida, Editor. 2007, Elsevier: Oxford. p. 311-379.

145. Frankel, J., A. Abbate, and W. Scholz, *The effect of residual stresses on hardness measurements.* Experimental Mechanics, 1993. **33**(2): p. 164-168.

146. Jang, J.I., *Estimation of residual stress by instrumented indentation: A review.* J. Ceram. Process. Res, 2009. **10**(391): p. 1996-1944.

147. Stepanov, G.V., et al., *Analysis of pulse current-induced tensile stress relaxation.* Strength of Materials, 2006. **38**(1): p. 84-91.

148. Mitra, R., *Intermetallic Matrix Composites: Properties and Applications*. 2017: Elsevier.

149. Wood, R.J., *Marine wear and tribocorrosion.* Wear, 2017. **376**: p. 893-910.

150. Chesnel, K., *Nanoscale Magnetic Domain Memory*, in *Magnetism and Magnetic Materials*. 2017, IntechOpen.

151. Stoner, E.C. and E. Wohlfarth, *A mechanism of magnetic hysteresis in heterogeneous alloys.* Philosophical Transactions of the Royal Society of London. Series A, Mathematical and Physical Sciences, 1948. **240**(826): p. 599-642.

152. Wohlfarth, E., *Hard magnetic materials.* Advances in physics, 1959. **8**(30): p. 87-224.

153. Cyrot, M., *Magnetisme.* Grenoble: Presses Universitaires de Grenoble, 1999: p. p. 37, 65

154. Lewis, G.N. and M. Randall, *Thermodynamics and the free energy of chemical substances*. 1923: McGraw-Hill.

155. Gao, M.C., et al., *The effects of applied magnetic fields on the α/γ phase boundary in the Fe–Si system.* Journal of Physics D: Applied Physics, 2006. **39**(14): p. 2890-2896.

156. Ravichandran, G., et al. *On the conversion of plastic work into heat during high-strain-rate deformation*. in *AIP conference proceedings*. 2002. American Institute of Physics.

157. Vdovin, E. and A. Kasumov, *Direct observation of electrotransport of dislocations in a metal.* Sov. Phys. Solid State, 1988. **30**(1): p. 180-181.

158. Jang, J.I., *Estimation of residual stress by instrumented indentation: A review.* J. Ceram. Process. Res, 2009. **10**(3): p. 391-400.

159. Tong, Z., et al., *Improvement in cavitation erosion resistance of AA5083 aluminium alloy by laser shock processing.* Surface and Coatings Technology, 2019. **377**: p. 124799.

160. Zhang, L., et al., *Effects of laser shock processing on electrochemical corrosion resistance of ANSI 304 stainless steel weldments after cavitation erosion.* Corrosion science, 2013. **66**: p. 5-13.

161. Tang, C., F. Cheng, and H.C. Man, *Improvement in cavitation erosion resistance of a copper-based propeller alloy by laser surface melting.* Surface and coatings technology, 2004. **182**(2-3): p. 300-307.

162. Tang, C., F. Cheng, and H. Man, *Laser surface alloying of a marine propeller bronze using aluminium powder: Part I: Microstructural analysis and cavitation erosion study.* Surface and Coatings Technology, 2006. **200**(8): p. 2602-2609.

163. Qin, Z., et al., *Microstructure design to improve the corrosion and cavitation corrosion resistance of a nickel-aluminum bronze.* Corrosion Science, 2018. **139**: p. 255-266.

164. Hanke, S., et al., *Cavitation erosion of NiAl-bronze layers generated by friction surfacing.* Wear, 2011. **273**(1): p. 32-37.

165. Song, Q., et al., *Corrosion and cavitation erosion behaviors of friction stir processed Ni-Al bronze: effect of processing parameters and position in the stirred zone.* Corrosion, 2014. **70**(3): p. 261-270.

166. Troitskii, O., *Electromechanical effect in metals.* ZhPmR, 1969. **10**: p. 18.

167. Sprecher, A., S. Mannan, and H. Conrad, *Overview no. 49: On the mechanisms for the electroplastic effect in metals.* Acta Metallurgica, 1986. **34**(7): p. 1145-1162.

168. Okazaki, K., M. Kagawa, and H. Conrad, *A study of the electroplastic effect in metals.* Scripta Metallurgica, 1978. **12**(11): p. 1063-1068.

169. Okazaki, K., M. Kagawa, and H. Conrad, *Additional results on the electroplastic effect in metals.* Scripta Metallurgica, 1979. **13**(4): p. 277-280.

170. Krishnaswamy, H., et al., *Electroplastic behaviour in an aluminium alloy and dislocation density based modelling.* Materials & Design, 2017. **124**: p. 131-142.

171. Conrad, H., A.F. Sprecher, and F. Nabarro, *Dislocations in solids.* Elservier, Amsterdam, 1989: p. 499.

172. Spytsin, V. and O. Troitsky, *Electroplastic Deformation of Metals*. 1985, Nauka, Moscow.

173. Fiks, V., *Interaction of conduction electrons with single dislocations in metals.* Soviet Physics JETP, 1981. **53**: p. 1209.

174. Babutskyi, A., et al., *Effect of pulsed magnetic treatment on the corrosion of titanium.* Materials Science and Technology, 2017: p. 1-12.

175. Golovin, Y.I., *Magnetoplastic effects in solids.* Physics of the solid state, 2004. **46**(5): p. 789-824.

176. *Barkhausen effect.* En.wikipedia.org.

177. Wu, S., et al., *A micro-mechanism model of residual stress reduction by low frequency alternating magnetic field treatment.* Journal of Materials Processing Technology, 2003. **132**(1): p. 198-202.

178. Shull, R.D., H. Okamoto, and P.A. Beck, *Transition from ferromagnetism to mictomagnetism in Fe—Al alloys.* Solid State Communications, 1976. **20**(9): p. 863-868.

179. Zhang, Y., et al., *Grain boundary characteristics and texture formation in a medium carbon steel during its austenitic decomposition in a high magnetic field.* Acta materialia, 2005. **53**(19): p. 5213-5221.

180. Mondolfo, L., *Aluminum Alloys: Structure and Properties, Butterworths, London/Boston*. 1976, Sydney-Wellington-Durban-Toronto.

181. *QuickField support site.* Quickfield.com.

Appendix A

```
/*
 This sketch is used to drive the magnetizing experiment in the material testing lab
*/
//*********************************************************************************
**********************************
const int CurrentPeriod = 5000;   // Change this number for the current time in each
direction in miliseconds
//*********************************************************************************
**********************************
const int RunStopSwitch = 12;      // define the Run/Stop switch
int RunStop = 0;                   // declare the vairable RunStop and set it to "0"
// the setup function runs once when you press reset or power the board
void setup() {
  delay(5000);                   // wait 5 seconds to let the capacitors to charge
  pinMode(LED_BUILTIN, OUTPUT);    // initialize digital pin LED_BUILTIN as an output.
  pinMode(10, OUTPUT);             // define digital pin 10 as output for relay  no 1
  pinMode(11, OUTPUT);             // define digital pin 11 as output for relay  no 2
  pinMode(RunStopSwitch, INPUT);   // define digital pin 12 as input for RunStop switch1
}

// the loop function runs over and over again forever
void loop() {
  RunStop = digitalRead(RunStopSwitch);
                          // get the status of the RunStop switch
  if (RunStop == HIGH){            // test to se if the switch is in Run or Stop position
  digitalWrite(LED_BUILTIN, HIGH);  // turn the LED on (HIGH is the voltage level)
  digitalWrite(10, HIGH);          // switch on relay no. 1
  delay(10);                     // wait 10ms
  digitalWrite(11, LOW);           // switch on relay no. 2
  delay(CurrentPeriod);                  // wait for 30 seconds
  digitalWrite(LED_BUILTIN, LOW);   // turn the LED off by making the voltage LOW
```

```
digitalWrite(10, LOW);          // switch off relay no. 1
delay(10);                  // wait 10 ms
digitalWrite(11, HIGH);         // switch off relay no. 2
delay(CurrentPeriod);               // wait for 30 seconds
}
else {
 digitalWrite(10, LOW);         // turn relay no 1 off
 digitalWrite(11, LOW);         // turn relay no 2 off
}
}
```

Appendix B

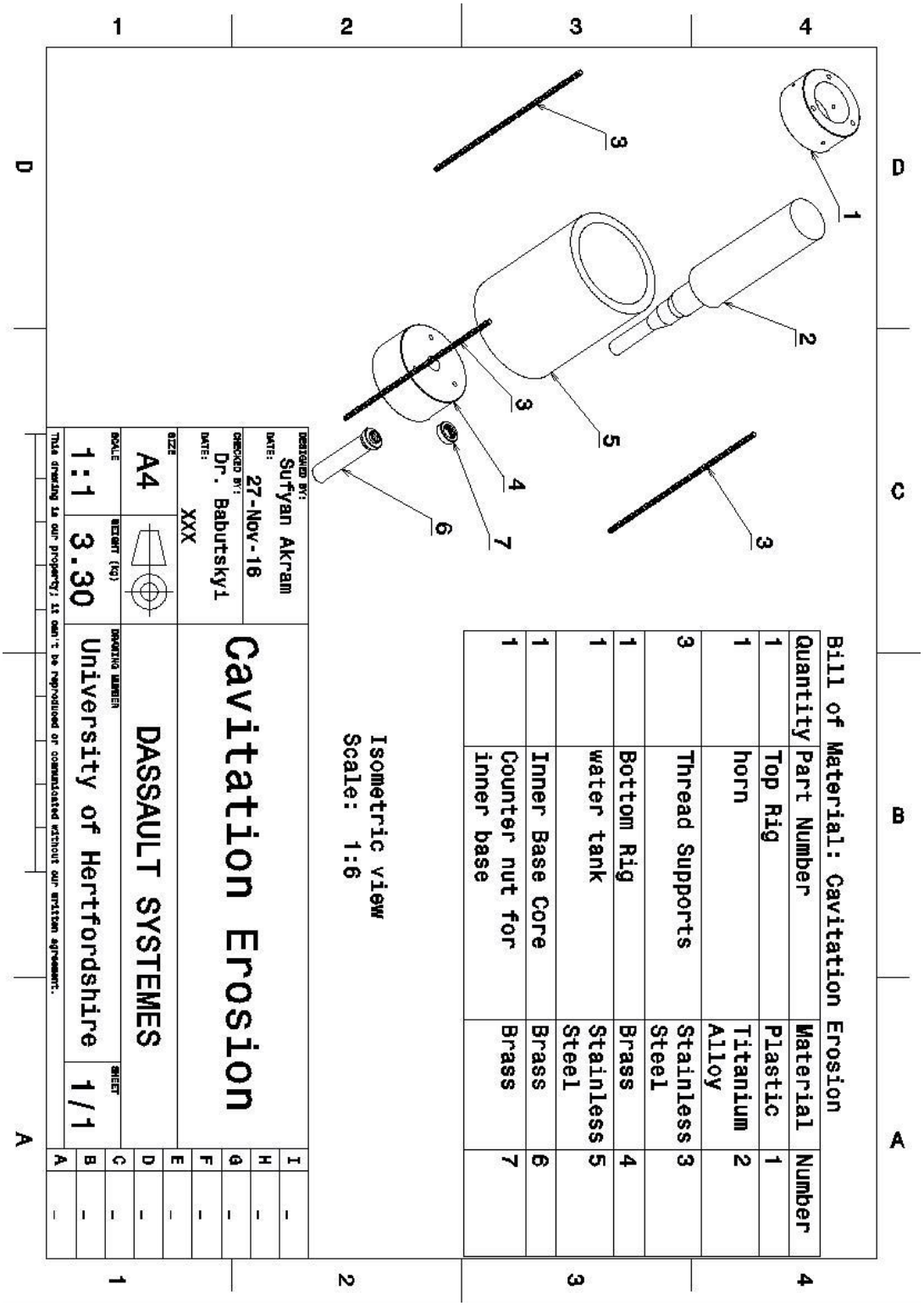
Bill of Material: Cavitation Erosion
Number | Material | Quantity | Part Number
1 | Plastic | 1 | Top Rig
2 | Titanium Alloy | 1 | horn
3 | Stainless Steel | 3 | Thread Supports
4 | Brass | 1 | Bottom Rig
5 | Stainless Steel | 1 | water tank
6 | Brass | 1 | Inner Base Core
7 | Brass | 1 | Counter nut for inner base
Isometric view
Scale: 1:6
Cavitation Erosion
DASSAULT SYSTEMES
University of Hertfordshire
Surfyan Akram
27-Nov-16
Dr. Babutsky1
XXX
A4
1:1
3.30
1/1
This drawing is our property; it can't be reproduced or communicated without our written agreement.

Appendix C

Finite Element Analysis modeling of Alternating Magnetic Field Treatment

Finite Element Analysis Modelling with QuickField 6.4 Pro

QuickField 6.4 pro (Tera Analysis, Svendborg, Denmark) is a finite element analysis (FEA) software used to model enviroments for electromagnetic, thermal and stress analysis. In this research FEA modelling was conducted to determine the eddy current and magnetic field distrbution at the sample during treatment. FEA modelling was conducted for treatments for each type of study (fatigue, friction and cavitation erosion). The FEA model was created as a transient magnetics problem which can simulate transient or steady state AC analysis for designing a variety of DC or AC devices such as electric motors, transformers, etc. Generally, the quantities of interest in transient magnetics analysis are time functions of magnetic flux density, field intensity, external, induced and total current densities, force, torque, inductance and flux linkage. The transient magnetic field simulation can be coupled with other types of solution such as temperature. The solution was conducted for 2-D formulation of a transient magnetic field problem.

The transient magnetic analysis is the generalized form of computation electric and magnetic field. It is derived by either direct or time-varying currents (alternating, impulse, etc.), permanent magnets or external magnetic fields, in linear or nonlinear (ferromagnetic) media. Furthermore, it takes into account eddy current (skin) effect in conductors of electric current [181].

To increase the accuracy of the FEA model, a ¼ geometrical model was used to increase the number of elements and nodes that the solver used. Figure 0.1 shows the ¼ geometrical model of treatment arrangement used during numerical modelling, while physical properties of the samples and model components are presented in Table 0.1. Depending on the type of study, a different spacer and sample geometry were used.

Table 0.1. Physical properties of materials used during modelling [130].

Property	Core (steel)	Spacer (steel)	Winding wire (copper)	EN8 Steel* sample	AA2014-T6* sample	NAB** sample	70/30 Brass* sample	Surrounding air
Conductivity, MS/m	10	10	56	10	23	2.3	13.8	0
Relative permeability	B-H curve*	B-H curve*	1	B-H curve*	1	1.5	1	1
The magnetic flux density vs magnetic field strength (B-H) curve for steel was taken from [130] and [103]**								

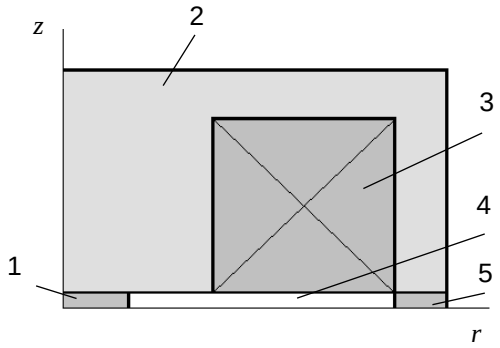

Figure 0.1. Schematic view of ¼ model used during modelling: 1 – disc sample, 2 – magnetizer core; 3 – winding (consists of 70 turns), 4 – air, 5 – spacer.

Full current time variation *I(t)*, passing through every single turn of magnetizer winding can be presented by the equation:

$$I(t) = I_0\, sign(sin(2\pi \times \frac{t}{T})), \qquad \text{Equation 0.1}$$

where T = 10 s is a period of time that the field acts in both directions during magnetization (Figure 3.6). The value of I_0 was determined based on the best fitting of the calculated and registered profiles of the magnetic field for the magnetizer without a sample; the values obtained were 0.54 T for the fatigue sample set up, 0.75 T for the cavitation erosion sample set up and 1.25 T for the set up for pin-on-disc samples (Figure 3.6). An example of the set-up for the FEA model for AA2014-T6 is shown in Figure 0.2. In this example a 10 mm diameter 5 mm thick sample was treated using the alternating magnetic field treatment. The highest magnetic flux density for this treatment was 0.75 T. Each copper winding was assigned a

theoretical equation for the alternating magnetic field. The equation that was assigned to each copper stand is presented below:

$$29.5 \times sign(sin(360 \times \frac{t}{10})), \qquad \text{Equation 0.2}$$

An axisymmetric model was used for the FEA. The finite element analysis mode was solved for up to 15s with a step size of 0.0025s. A mesh size of 2.5 mm was used at the points of each copper winding. A smaller mesh size of 0.5 mm was used for the sample. The smaller mesh was divided into smaller sub-layers for greater accuracy. Mesh convergence was obtained at 2188 nodes of mesh.

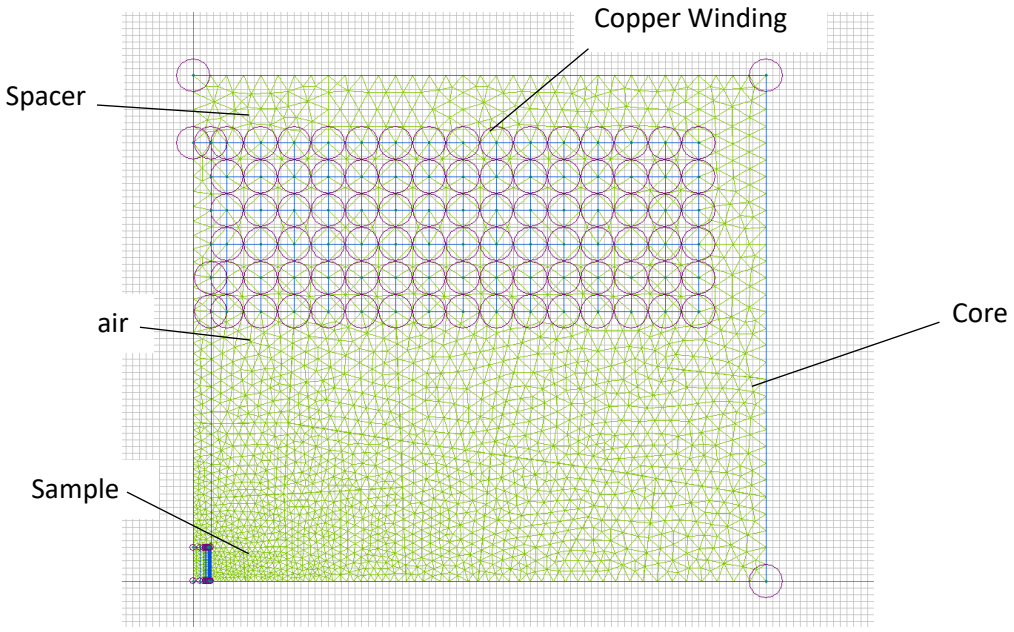

Figure 0.2. Quickfield simulation of ¼ model used during modelling: 1 – disc sample, 2 – magnetizer core; 3 – winding (consists of 70 turns), 4 – air, 5 – spacer.

Results

The results for the numerical modelling with the AA2014-T6 samples located at the centre of the core is shown in Figure 0.3 to Figure 0.6. According to the results of the numerical modelling, the AA2014-T6 sample was exposed to a magnetic flux density of about 0.82 T (shown in Figure 0.4) due to having a relative permeability of 1. During alternating of the

polarity of the magnetic field for AA2014-T6, the total step-change of the magnetic flux density is 1.64 T.

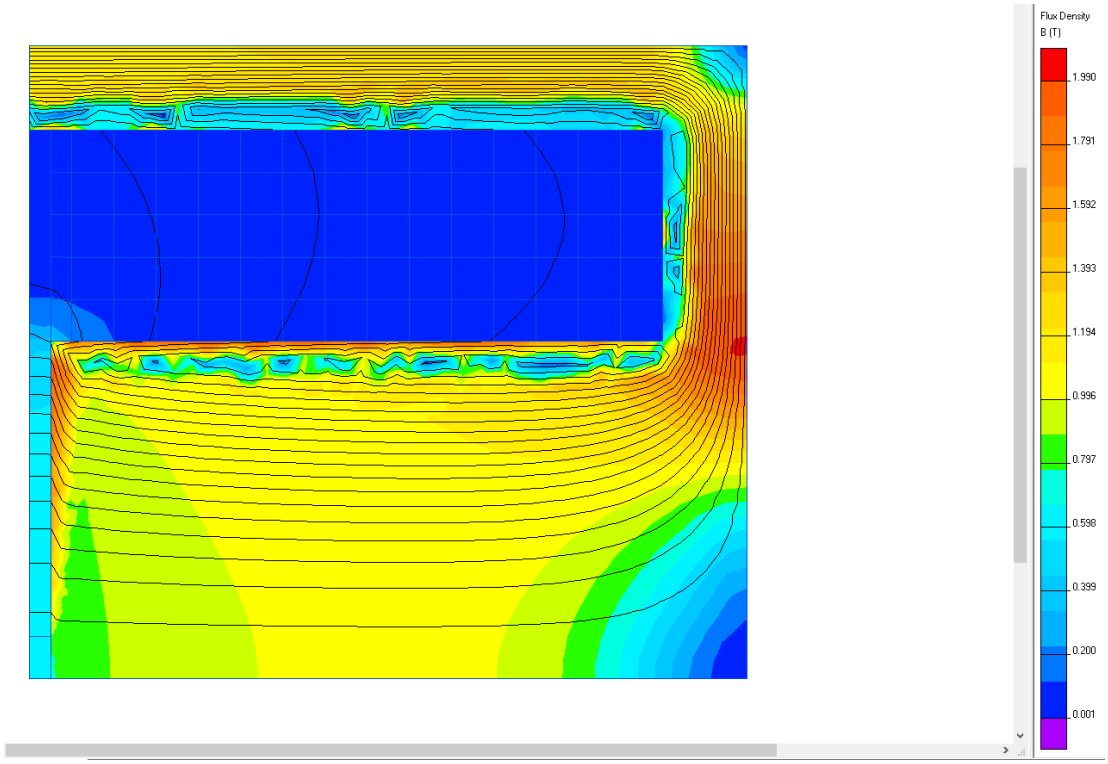

Figure 0.3. Example of transient simulation results of the magnetic flux density of AA2014-T6 at 5 sec.

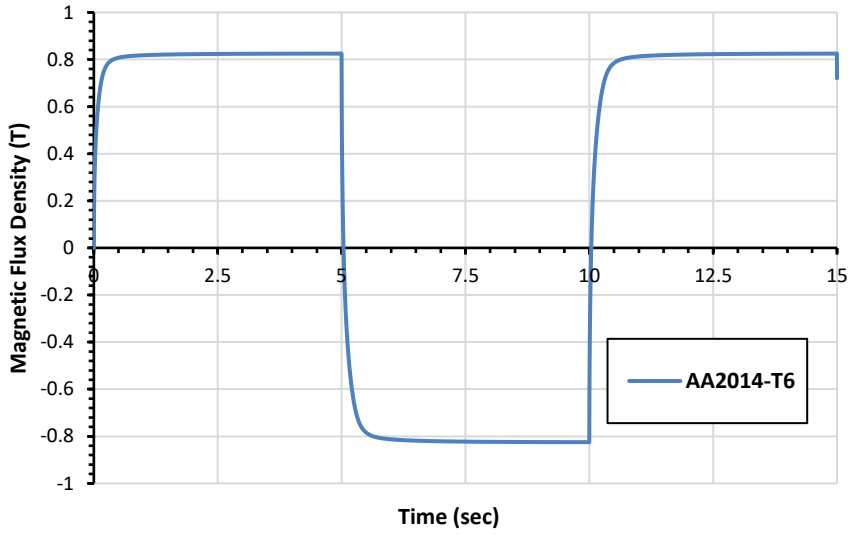

Figure 0.4. Magnetic Flux Density versus time for the AA2014-T6 sample.

During the alternating magnetic field treatment, the magnetic field varies every 5 s and as a result of this step-change of the field, eddy currents are induced in the samples. An example of the eddy current distribution as obtained by FEA modeling is presented in Figure 0.5. A peak eddy current is observed in the sample when the polarity alternates as shown in Figure 0.6a. Figure 0.6b presents the induced eddy currents along the outer radius of the AA2014-T6 sample. The maximum current density of 4.63×10^{6} A/m^{2} of the eddy currents was achieved at the edge of the cylindrical surface of the samples.

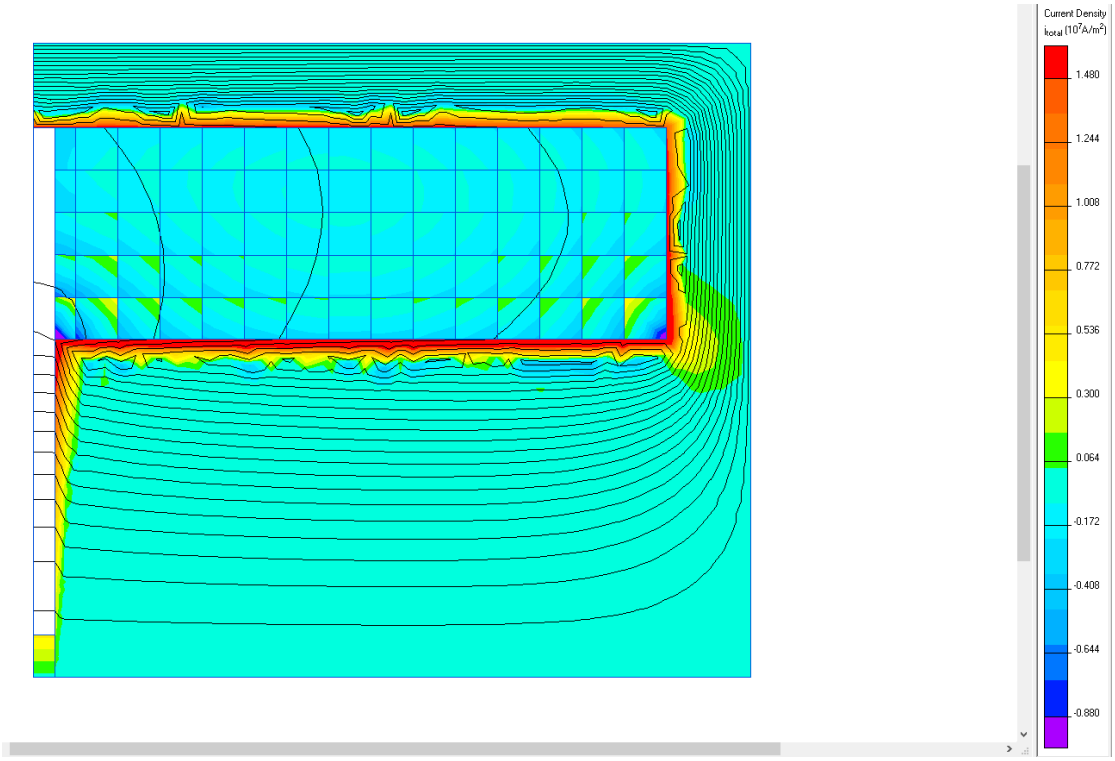

Figure 0.5. Example of transient simulation results of the current density distrbution during AMF treatment of AA2014-T6.

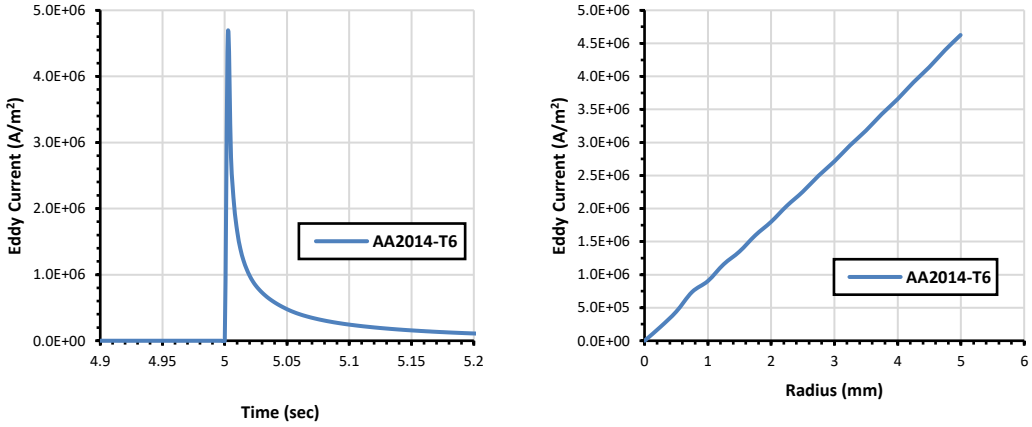

(a) (b)

Figure 0.6. Eddy current versus time (a) and eddy current verses radius (b) of AA2014-T6 sample.